Towards a Rubidium Quantum Gas Microscope

TOWARDS A RUBIDIUM QUANTUM GAS MICROSCOPE

MASTER THESIS

Submitted by:

JACOB F. FRICKE
Bachelor of science ETH in physics

January 2023

Supervised by:

PROF. WOLFGANG KETTERLE
PROF. TILMAN ESSLINGER
DR. JULIUS DE HOND

ABSTRACT

Correlations between the constituents of quantum many-body systems can produce highly entangled states showing e.g., superfluidity and magnetic ordering. Only a few detection schemes, like in situ single-site observation, allow direct measurement of those correlations between cold atoms in optical lattices. The quantum gas microscope presented here, with a numerical aperture of ~ 0.8, will collect atomic fluorescence and reconstruct the atoms position with high fidelity. The existing machine underwent a significant upgrade to achieve this, featuring a new octagonal chamber with a reentrant viewport housing the objective. Further changes include extending experimental control and implementing a lateral steering mechanism of the transport optical dipole trap. These adaptations will provide a powerful tool for future research in quantum many-body physics, approaching the goal of observing XY-ferromagnetic ordering in spin Hamiltonians.

ACKNOWLEDGEMENTS

A big thank you to Wolfgang, who made this time at MIT possible in the first place and served as a wonderful mentor and teacher. I was always impressed by his trust and confidence in our work and bringing me to MIT without prior experience in the field of cold atoms. I am also grateful for my advisor Tilman, who was willing to supervise this whole endeavor from a distance patiently and even crossed the Atlantic for a chat over a cup of tea.

The memorable time at MIT would not have been so fantastic without the people I've met and the friends I've made. I feel especially grateful for my lab mates Jinggang, Enid, and Julius, who "adopted" me to BEC4-family. They showed me around the lab and taught me much about cold atoms in frequent discussions. All the people from the CUA make this place special for studying AMO.

I enjoyed winding magnetic coils like we would go fishing, praying for the water jet to work, swearing at the lab's temperature control, locking lasers, making pickles glow, detecting high-energy particles, playing volleyball in the park, making candles late at night, going frisbee golfing, de-icing the freezer, collecting bananas from the banana room, stacking kittens and solving murder mysteries, watching birds hatch and making sure they survive,

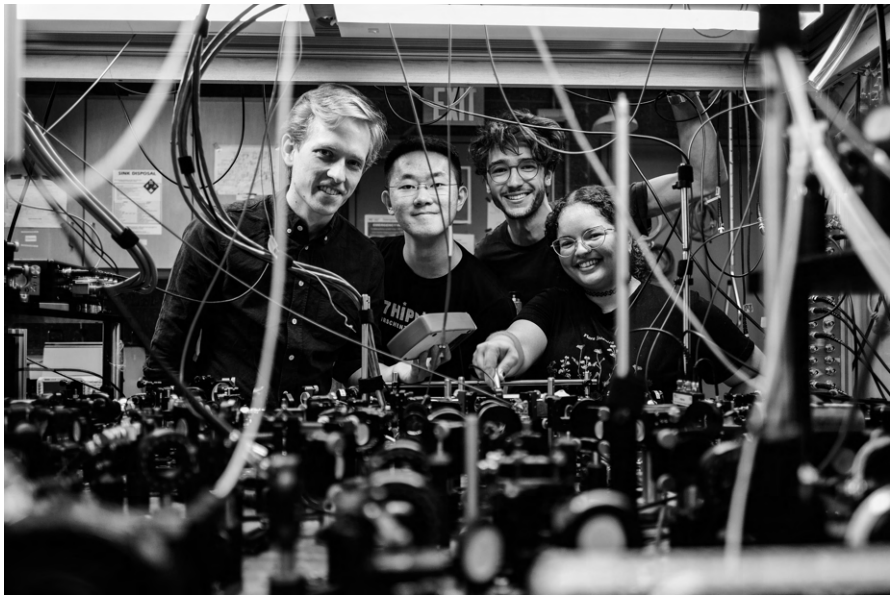

Figure 1: BEC4 team in summer 2022. Left to right: Dr. Julius de Hond, Jinggang Xiang, Jacob Fricke, Enid Cruz-Colón

plumbing and brazing pipes, assembling vacuum, picking up lead beads, learning electronics from Hanzhen, laughing about Cicero quotes, playing geo-guesser, scavenging tools from the hallway, having Wolfgang's BBQ, going snack hunting with Michael, building telescopes, sailing with Felix until our hands were numb, cross country skiing up the steepest hills, lab-cart racing in the basement, teaching how to flunky-ball, having Kaiserschmarrn competition with Botond[1], bouldering early in the morning with Eunice, having overtime coffee breaks with Mathew and Simone, grilling burgers with Jared, singing to the tunes of Martin and Markus ...

Of course, I could always count on my partner, roommates, and family to have an open ear in moments of frustration and to ensure I had enough breaks by exploring nature in Maine, beaches in Florida, and museums in NYC. The long bike trips to the beach and discussions on cell counting and eye-distortions over a good bowl of ramen or some veggie burgers will be missed.

1 Felix and I won.

CONTENTS

1

INTRODUCTION

Atomic physics is what atomic physicists do.

— Wolfgang Ketterle

ATOMIC, MOLECULAR, AND OPTICAL PHYSICS (AMO) has seen a revolution from detecting and understanding quantum properties of atomic systems toward manipulating and precisely controlling those quantities using light and other means. One discipline in the vast field of AMO physics is the study of ultracold neutral atoms. In contrast to ions, which possess strong and long-range Coulomb interactions due to the extra charge, neutral atoms are well isolated due to their weak coupling with the environment [1][1]. With the discovery of Bose-Einstein condensates (BEC) in 1995 by Eric Cornell, Carl Weimann [4], and Wolfgang Ketterle [5], a new era of atomic physics was launched. The study of degenerate atomic gases quickly became a field on its own, utilizing the unprecedented control over position and coherence properties similar to the laser [6].

Soon also, degenerate fermi-gases became possible [7], enabling the analysis of fermionic quantum statistics in various systems [8]. These advances in cooling and trapping techniques enabled the implementation of toy models for quantum simulation of many-body phenomenon [9–11], quantum computing [12–14], and quantum information processing [15, 16] in general.

Since many of those techniques for trapping and cooling are widely applicable to several atomic species, selecting a suitable atom is essential. The availability of affordable lasers and scattering properties influences many decisions according to atomic species. For example, alkali atoms like Rubidium (Rb), Sodium (Na), and Lithium (Li) inhibit a rather hydrogen-like level structure. The Hydrogen character makes manipulating those Alkali species more manageable. Alkali-Earth atoms like Strontium (Sr) have an additional electron to play with, giving rise to more complex level structures with clock-transitions [17]. In recent years, the progress on magnetically dipolar atoms such as Dysprosium (Dy) and Erbium (Er) also took off [18]. These

1 This is not an inconvenient property of ions in general. For example, the strong coupling of ions to external electric fields makes it easy to generate strong trapping potentials in which the ions can remain for days or months, and measurements can be performed [2, 3].

lanthanides with spin-orbit coupling in the ground state have a "zoo" of optical transitions with line widths ranging from MHz to a few kHz. These additional "knobs to turn" can be used to engineer interactions and maybe implement new Hamiltonians in quantum simulators. Other groups are progressing toward controlling molecules [19] that possess complex states with additional vibrational and rotational manifolds. On the other side, these different molecular degrees of freedom enable physicists to use strong electric dipolar interactions between the molecules [20].

Following this work, many groups worldwide have pursued the goal of using these cold atomic systems as "Lego blocks," and generated insights into the world of natural solids by mimicking the properties of solids with cold atoms in optical lattices [9, 21, 22]. This experimental platform is a form of analog quantum computing or quantum simulation. In a nutshell, optical lattices are periodic potentials formed by the interference of light, in which the atoms are attracted to either the minima or maxima of the light intensity [23]. The atoms in the optical lattice mimic the behavior of electrons in a solid. The benefit of using neutral atoms in optical lattices to approach this task is the scale. Atoms in genuine solid crystals are only Angstroms away, whereas atoms in optical lattices have a separation on the order of optical wavelengths, i.e., several hundred nanometers. The beauty of the optical lattice is also in its flexibility in creating somewhat arbitrary potential geometries by changing the color, angle, or intensity of the lasers being used.

A certain state is prepared as a starting point if the chosen atoms or molecules are loaded into the optical lattice. Often that state is low in entropy and prepared from loading a BEC into a lattice. After the time evolution, according to some engineered Hamiltonian of the many-body wavefunction, one would like to measure the observables of the system. A measurement constraint is set by the condition of the delicate atoms being isolated in an ultra-high vacuum (UHV), often limiting the optical access. One can use time-of-flight (TOF) techniques to let the cloud expand and measure the local density profile by absorption imaging. Expanding the clouds can reduce the imaging system's required resolution drastically. TOF maps the atoms' instantaneous momentum distribution in the lattice onto a real space image. The conversion from bulk atom-number counting to microscopic observables can become cumbersome for some applications. On the other side, super-resolution imaging doesn't require the expansion of the cloud. It uses dark states to obtain a mapping of the atomic wave function with the sublattice spacing resolution. Still, it does not generate a single site resolution or addressing of the lattice [24, 25].

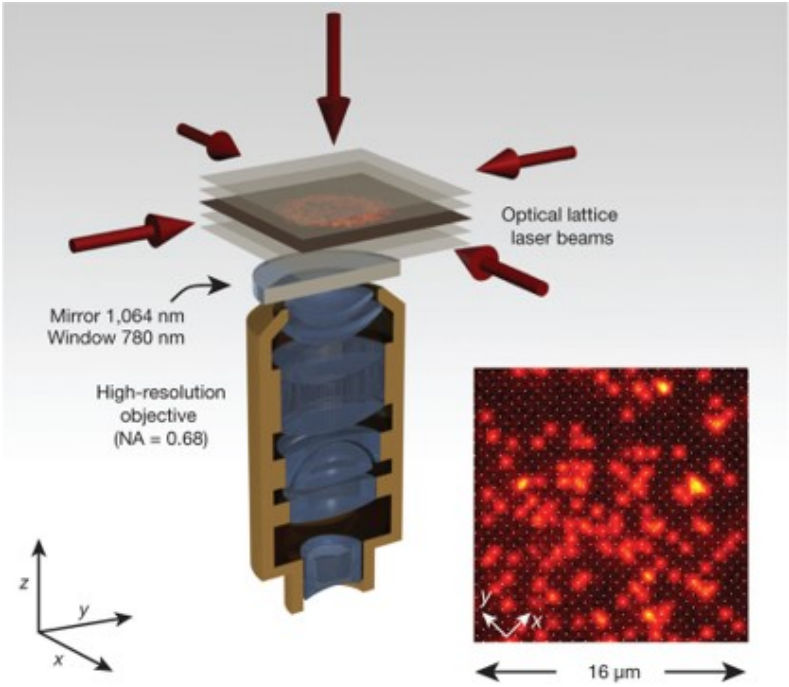

Figure 2: Schematic for single site resolved microscopy of Rubidium atoms in an optical lattice formed by retro reflecting 1064nm laser beams. The insert shows the detected fluorescence, together with the reconstructed lattice. The image is adapted from reference [26].

An elegant way to take in situ images of the position of the atoms in the lattice is a quantum gas microscope (QGM). As mentioned earlier, the atoms are separated on the order of an optical wavelength ($\sim \lambda/2$). Using a high numerical aperture (NA) objective, one can collect atomic fluorescence over a large enough solid angle and reconstruct the atom's position by measuring the local point spread functions. This scheme is only possible if the NA and fluorescence wavelength λ_f are chosen to enable a maximal resolution $r \approx \lambda_f/2NA$ [27] comparable to the separation of the atoms. Every piece of optics in the imaging path must be chosen carefully to guarantee aberration-free imaging. Especially vacuum viewports can become a critical element.

There are two main configurations for imaging. Either the objective is placed outside the vacuum [28], or there are in-vacuum optics [29]. If the objective is positioned outside the UHV chamber, the highly divergent light will pass through the UHV viewports. The image won't be diffraction limited when the viewports are not flat due to mechanical stress or fabrication imperfections. Also, optics outside vacuum chambers for single-site resolution are often bulkier because collecting the minimal solid angle of the fluorescent light farther away from the source requires a larger area of glass.

On the other hand, it can be pretty convenient to have easy access to the objective outside UHV for refocusing, positioning, or maintenance.

The first QGM was demonstrated by the group of Markus Greiner in 2009 [30]. Since then, a few more groups, such as students of Immanuel Bloch [26], Peter Schauss [31], Wasem Bakr [32], Martin Zwierlein [33], and more, have implemented objectives in their experiments with single-site resolving power. An additional benefit introduced by the QGMs is an ability to project almost arbitrary potentials onto the system through the objective using spatial light modulators (SLM) or similar techniques [34], which can be on the lengthscales of the lattice. From the direct observation of Mott insulator states [26] to spin-resolved imaging [35], the QGM has proven to be a mighty tool for quantum many-body physics[2].

THE MOTIVATION FOR THE RUBIDIUM LAB (BEC4) at MIT to have a QGM was to observe the long-range correlation of a 1D - ordered XY-ferromagnetic state. This XY-ferromagnetic state has zero net magnetization, but large quantum fluctuations [36]. This physics goal to investigate quantum magnetism was pursued by previous generations of Ph.D. students. However, it was not yet entirely successful despite gaining insights into the preparation of the states and its limitations.

In a Bose-Hubbard regime, the system's behavior is determined by the interactions between bosons, which obey Bose-Einstein statistics. In a two-component system, there are two types of bosons, which in our case, are different spin states of Rubidium. In particular, we prepare a mixture of two hyperfine states, A and B, of Rubidium ($A = |F = 1, m_F = -1\rangle$, $B = |F = 1, m_F = 1\rangle$). The Hamiltonian includes terms representing the interactions between A and B and terms describing the individual bosons' kinetic energy. Due to contact interaction away from Feshbach resonances, we have $U_{AA}, U_{BB}, U_{AB} > 0$. This two-component system can be mapped in second-order perturbation theory onto a bosonic spin one system [36–39]. This mapping is depicted schematically in Figure 3 a). The kinetic energy and interaction energy parameters can be controlled using a spin-dependent lattice. This particular lattice can continuously change the separation and overlap between the Wannier wave functions of constituents A and B, thereby changing the inter-species interaction U_{AB}. Ultimately the choice of lattice parameters will change the ground state of the spin system [38].

As shown in Figure 3, in the limit of maximal separation between the components A and B, the system is in the spin-Mott state [40]. Since A and B wave functions are maximally separated, there is minimal penalty U_{AB},

2 Owning a great tool does not guarantee to produce great physics.

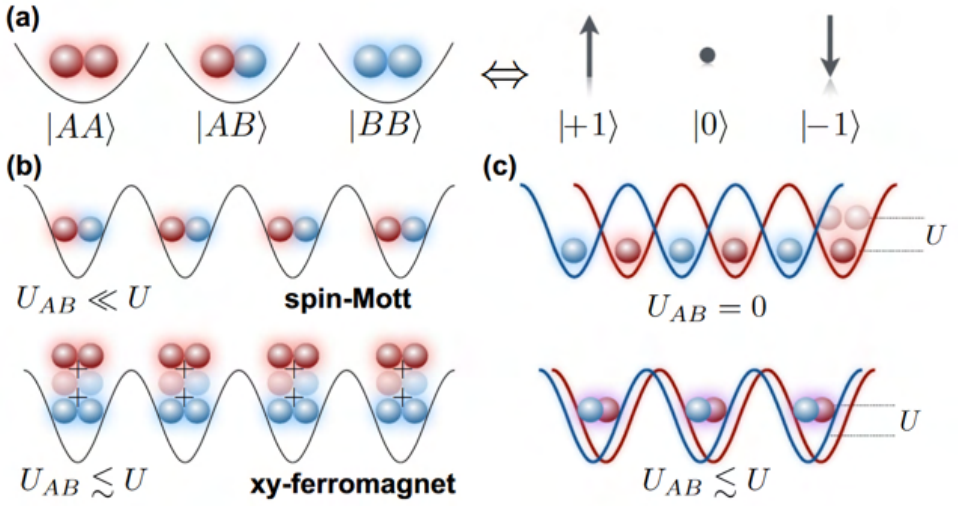

Figure 3: a) In the limit of second-order perturbation theory, one can map a two-component Bose-Hubbard system onto a spin one configuration. Two equal species per unit cell AA or BB can be considered spin +1 or -1, and two different species per unit cell AB is spin 0. b) The spin-Mott state - a product state - is the system's ground state in the limit of small inter-species interactions. Suppose the interaction U_{AB} is adiabatically increased. In that case, the system tries to stay in the ground state, and the quantum fluctuations explore the correlated spin-aligned state resulting in XY-ferromagnetism. c) The spin-dependent lattice can be used to tune the interactions of the two species in their unit cell. By separating the wavefunctions of the two atoms A and B, U_{AB} can be minimized, generating a spin-Mott state. When the overlap is larger, U_{AB} can be comparable to U. [36]

and the system prefers to fill the unit cell with components A and B equally. At the same time, the system is protected by the intra-species interaction U_{AA} or U_{BB} and forms a gapped state with zero net magnetization, the spin-Mott.

In the XY-ferromagnet, the system is in a state where the bosons have zero net magnetization but tend to align their spin fluctuations in the same direction, forming a ferromagnetic state. This state can be characterized by the presence of long-range order, where the spins of the bosons are correlated over long distances. In addition, the system may exhibit other characteristic features of ferromagnetism, such as spontaneous magnetization.

The behavior can be explained using the concept of a quantum phase transition [41]. At zero temperatures, the system can undergo a phase transition as a parameter in the Hamiltonian is changed without needing thermal fluctuations. The different ground states of the many-body system compete as the parameter U_{AB} is tuned, leading to the transition.

BUILDING AN APPARATUS capable of producing single-site resolved fluorescence imaging is a big challenge. As is typical for AMO experiments, "building and running an apparatus is a bit like hunting. Everyone has their role, must contribute, and work as a team" - Dave Prichard. The Rubidium experiment in Wolfgang's group has planned the upgrade of the science chamber for a long time. Previous generations of graduate students part-time organized this endeavor while the experiment was still operating, slowing down the process. However, the breakdown of the primary cooling laser in 2021 has forced the team to focus more on the upgrade and push the new project for a quantum gas microscope. I joined the lab consisting of two Ph.D. students and a Postdoc to learn about the Rubidium experiment and support their efforts.

The thesis is structured into three main parts.

PART I focuses on introducing the techniques used to cool and trap Rubidium in the machine behind the doors of BEC4. This will feature beam slowing, magneto-optical trapping, and magnetic trapping. Furthermore, the formalism for trapping atoms using the light shift based potential is presented.

PART II of the thesis describes the installation and ground loop isolation of new analog and digital control channels. In particular, how those ground loops cause problems in the experiment and how the new system can prevent them.

PART III concentrates on the upgrades to the machine. It begins by giving an overview of the new vacuum system's components and the assembly and bakeout of the latter. It highlights a coating failure during the bakeout and the subsequent design change. In addition, a mechanism to move the lateral transport optical dipole trap is discussed. The part ends by explaining the progress of cooling Rubidium to BEC and an outlook for the future.

Part I

A HITCHHIKER'S GUIDE TO COOLING AND TRAPPING OF RUBIDIUM

The level structure of Rubidium is briefly reviewed, together with methods to cool and control its motion with lasers and evaporation schemes to reach degenerate atomic quantum gases. (The reader already familiar with the topic is welcome to get a coffee and enjoy a recap or skip.)

1.1 HYPERFINE STRUCTURE OF ^{87}RB

Rubidium (Rb) is an alkali atom, and in the central field approximation, it can be seen as a single electron orbiting a screened hydrogen-like charge density [1]. The typical level structure (not to scale) is depicted in Figure 4. The spectroscopic features in the schematic are divided into three columns from left to right: fine-structure doublet, hyperfine manifolds, and magnetic sub-levels of the latter. The exquisite control of transitions between these levels and a thorough understanding of these is necessary for cooling and trapping techniques in cold atom experiments.

Coupling of the orbital angular momentum **L** with the electron spin **S** contributes to the non-degenerate fine-structure of Rubidium with total angular momentum $\mathbf{J} = \mathbf{L} + \mathbf{S}$.

In spectroscopic notation, a state manifold is then characterized by term symbols like $|n^{2S+1}L_J\rangle$, where n is the principle quantum number. The optical transitions between the ground state manifold $|5^2S_{1/2}\rangle$ to $|5^2P_{1/2}\rangle$ (~ 794 nm) and $|5^2S_{1/2}\rangle$ to $|5^2P_{3/2}\rangle$ (~ 780 nm) are called D_1- and D_2-line respectively. Especially the D_2 line is important for the laser cooling cycle of Rubidium since it includes a cycling transition and gives Rubidium a quasi-two-level structure.

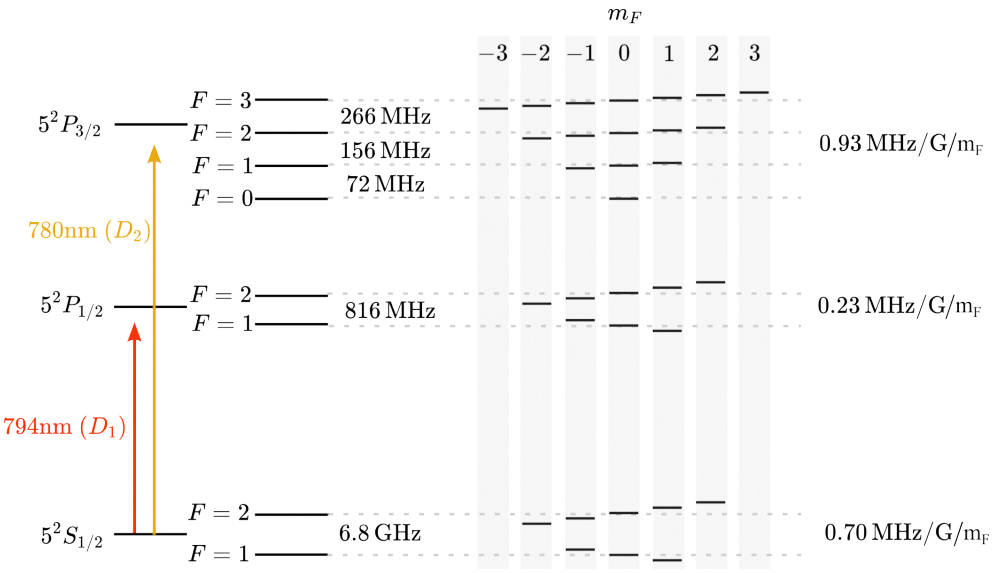

Figure 4: Hyperfine Level structure of Rubidium 87 (not to scale). The schematic shows the D_2 ($5^2S_{1/2} \rightarrow 5^2P_{3/2}$) and D_1 ($5^2S_{1/2} \rightarrow 5^2P_{1/2}$) line transition in the first column. The middle column shows the hyperfine splitting from J-I coupling and the approximate level splitting between adjacent hyperfine states. The third column represents magnetic sub-levels and their anomalous Zeeman splitting in the small B-field regime. [42]

Rubidium's nuclear spin $\mathbf{I}$ is non-zero with $I = 3/2$ for ^{87}Rb and $I = 5/2$ for the more abundant isotope ^{85}Rb. The interaction between the nuclear magnetic moment and the electron creates a correction of the eigenstate energies of the fine structure. Since for Rubidium, the hyperfine splitting is small compared to the energy splitting of the LS-coupling, the hyperfine Hamiltonian can be written to first order as [1]

$$H_{hf} = A_{hf}\,\mathbf{J}\cdot\mathbf{I}. \tag{1}$$

With A_{hf} being the hyperfine constant [42]. The interaction couples the nuclear spin $\mathbf{I}$ to the angular momentum $\mathbf{J}$ and gives rise to the conserved total atomic angular momentum

$$\mathbf{F} = \mathbf{J} + \mathbf{I} \quad \text{with} \quad |J - I| < F < J + I. \tag{2}$$

Each hyperfine manifold with quantum number F consists of $2F + 1$ magnetic sub-levels that are degenerate at zero external magnetic fields. The Hyperfine states are labeled as $|n^{2S+1}L_J, F, m_F\rangle$ or simply $|F, m_F\rangle$, with m_F being the magnetic quantum number, i.e. the eigenvalue of the operator $F_z/\hbar$.

The splitting between the individual hyperfine levels in Figure 4, $\omega_{\Delta F}$ is $\sim 1\,x\,2\pi$ GHz. Hence the splitting originating from the JI-coupling is four orders of magnitudes smaller than the energy gap between the fine-structure splitting ($\sim$ 15 nm), which justifies our previous assumption.

So far, only the basic properties and notation of the hyperfine structure of rubidium originating from intrinsic magnetic dipole interaction have been given. When introducing a static external magnetic field $\mathbf{B}$, the individual magnetic sub-levels $|F, m_F\rangle$ lose their degeneracy. In the limit where the interaction energy is small compared to the hyperfine splitting, F remains a "good" quantum number. The Hamiltonian producing the anomalous Zeeman effect can then be written as

$$H_{B_{ext}} = \frac{\mu_B}{\hbar}(g_S\mathbf{S} + g_L\mathbf{L} + g_I\mathbf{I})\cdot\mathbf{B} \approx \frac{\mu_B}{\hbar}g_F\mathbf{F}\cdot\mathbf{B}, \tag{3}$$

with

$$g_F \approx g_J\frac{F(F+1) - I(I+1) + J(J+1)}{F(F+1)}, \tag{4}$$

and g_J being J dependent [42]. Depicted in the rightmost column of Figure 4 are the individual magnetic sub-levels. Also labeled is the approximated frequency shift per applied magnetic field strength in Gauss (1 G $= 10^{-4}$ T). As an example, when applying a magnetic field of 200 G in the $\hat{z}$-direction, the $|5^2S_{1/2}, F = 1, m_F = -1\rangle$ state would be detuned by +140 MHz from $|5^2S_{1/2}, F = 1, m_F = 0\rangle$. Hence by "winding coils" around the apparatus,

we can vastly tune the transitions of Rubidium, and gain more control over the atom, which is important for Zeeman slowing, magneto-optical trapping, magnetic trapping, and RF-induced evaporation.

With the basic atomic structure of Rubidium introduced, a short overview of a few experimental techniques for cooling and trapping Rb is given in the following chapters. The order will represent the timeline in the BEC4 Rb experiment.

1.2 RADIATION PRESSURE SLOWING

To reach the Bose-Einstein condensate (BEC) state, the phase space density must be increased by cooling the gas and dissipating entropy. Laser cooling and evaporation cooling are the two main procedures by which this is achieved.

The atoms are ejected from an oven that creates vapor pressure of Rubidium and ejects the atoms with a mean velocity of ~300 m/s into the slower. If hot and fast atoms move in the laboratory frame toward a resonant laser field, they can scatter photons with momentum $\hbar\mathbf{k}$ from the field to a random direction at a scattering rate R_{sc}. On average, the atoms feel a slowing force from the laser due to the momentum kick of the photon [43]

$$\mathbf{F}_{rad} = \hbar\mathbf{k}R_{sc} = \frac{\hbar\mathbf{k}(\Gamma/2)^3}{\Delta^2 + (\Gamma/2)^2}\frac{I}{I_{sat}}. \tag{5}$$

With Γ being the natural line width of the D_2 transition, Δ the detuning from resonance and $I_{sat} = \hbar\omega_0\Gamma/2\sigma_0 \approx 3.6\ \mathrm{mW/cm^2}$ [42]. As the atoms slow down, the doppler shift brings them out of resonance with the slowing light.

In the Zeeman slower used in BEC4, the atom's cycling transition is kept in resonance with the light by shifting the energy splitting with an increasing magnetic field [44], compensating for the doppler shift.

Most of the cooling of atomic gases is done in traps. After an atomic beam is slowed down using the radiation pressure in a Zeeman slower, it is loaded into a magneto-optical trap (MOT). Here the MOT catches ~ 10^8 atoms from the slower beam and then transitions into optical molasses while the atoms are transferred into a magnetic trap for evaporative cooling. The next sections will give some highlights of these mechanisms.

1.3 DOPPLER COOLING IN OPTICAL MOLASSES

We can further cool down the atoms once they are slowed down from the oven to only several meters per second. In the case of 1D optical molasses, the atoms sit in the center of two counter-propagating light fields. The light is red-detuned several MHz below the resonance of the cycling transition. When the atom is moving toward one of the beams, the frequency of the counter-propagating light appears more blue-detuned and hence closer to resonance, leading to an absorption event that transfers a recoil. The resulting dissipative force in the limit of small initial velocities is [43]

$$\mathbf{F}_{\text{rad}} = -\alpha\mathbf{v} = \frac{\hbar k^2 \Gamma^3}{2} \frac{\Delta}{[\Delta^2 + (\Gamma/2)^2]^2} \frac{I}{I_{\text{sat}}}\mathbf{v}. \tag{6}$$

The temperature limit achievable is the Doppler limit $T_D = \hbar\Gamma/2k_B$, which for Rubidium is $T_D \approx 146$ μK [42]. The optimal damping α, occurrs when the detuning is $\Delta = \Gamma/2\sqrt{3}$ [43].

1.3.1 *Magneto-Optical Trap*

The magneto-optical trap (MOT) is created when the molasses scheme[3] is placed into an inhomogeneous anti-Helmholtz field [45]. Next to cooling, it is also used to accumulate the atoms from the Zeeman slower.

Six independent, pairwise $\sigma^+ - \sigma^-$ polarized beams are detuned by ~ -18 MHz from the $F = 2 \rightarrow F' = 3$ transition [44]. When the atoms move away from the magnetic field minimum, the Zeeman shift brings the respective hyperfine level in resonance with the counter-propagating circular polarized light while detuning the co-propagating polarization. This traps the atom to the center of the magnetic field minimum.

Figure 5 shows an image of the fluorescing MOT in the main chamber. The six individual beams must all overlap at the magnetic field minimum, and their intensity must be carefully balanced.

1.3.2 *Sub-Doppler Cooling*

The σ^+-σ^- optical molasses can produce sub-Doppler cooling when no magnetic field is present in the slow velocities limit[4] due to a polarization gradient [46]. The mechanism is used in BEC4 after the MOT loading phase by

3 Here it refers to the geometry of six counter-propagating beams overlapping in one point.
4 Slow compared to the optical pumping rate. [46]

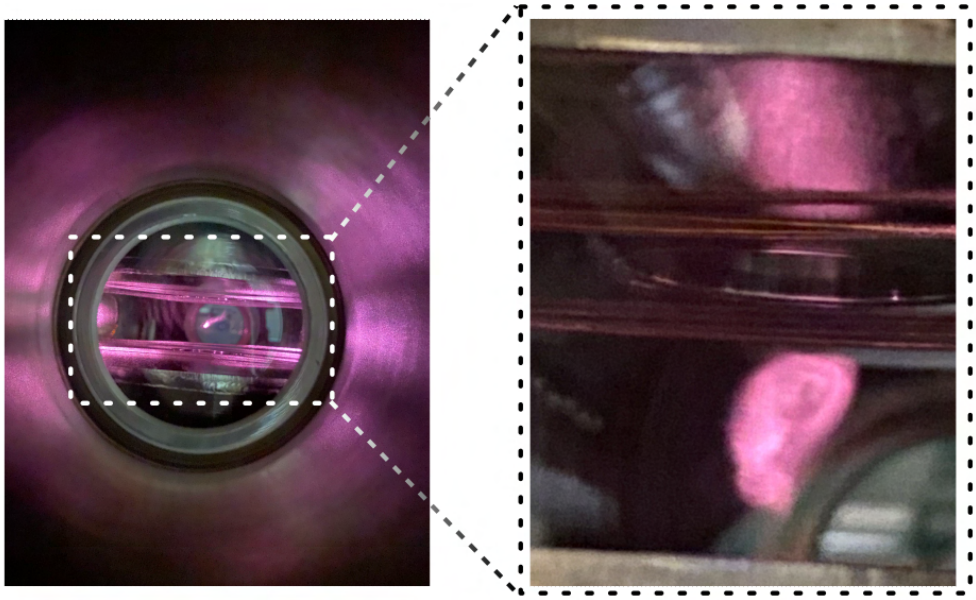

Figure 5: Image of a healthy MOT of Rubidium atoms in the main chamber of BEC4. The cloud is easily visible.

ramping down the MOT coils. In contrast to Sisyphus cooling, the ellipticity of the local light field remains constant, and there is no change in vector light shift along the propagation axis. As the atom moves slowly through the polarization gradient, a population imbalance in the ground state builds up. This population imbalance increases the scattering of photons from the counter-propagating field, leading to a velocity-selective dampening force [46].

The achievable temperature limit of the $\sigma^+ - \sigma^-$ polarization gradient cooling mechanism approaches the recoil temperature $T_r = (\hbar k)^2/k_B m_{Rb}$ [1, 46]. This theoretical limit for Rubidium would be $T_r \approx 362$ nK [42]. This is usually not achieved in the lab, but the mechanism contributes to the cooling, creating temperatures of ~ 10 μK for Rubidium [47].

1.4 MAGNETIC TRAP

The magnetic trap is a part of many cold atom experiments and contributed to achieving BEC in the first experiments [6]. In BEC4, the magnetic trap design is an Ioffe-Pritchard trap with cloverleaf coils [44] as displayed in Figure 6. The energy of an atom due to its interaction with a magnetic moment μ_F in a magnetic field B is

$$H = g_F m_F \mu_B B. \tag{7}$$

For $g_F m_F > 0$, the atom is attracted to a local minimum of the magnetic field B. These states are called low-field seeking states and are the only ones that can be trapped since there can't be a local maximum in the magnitude of the free magnetic field [1, 48]. A low field seeking state in Rubidium is $|F = 1, m_F = -1\rangle$ ($g_F = -1/2$) or $|F = 2, m_F = 2\rangle$ ($g_F = 1/2$). If the atom is in a state where $g_F m_F < 0$, it is rejected from the trap, like the state $|F = 1, m_F = 1\rangle$.

The transition from trapped to untrapped can occur by applying an RF signal tuned to the right frequency or when the atom moves too fast through an inhomogeneous field. The second case can be suppressed as long as the spins of the atoms are adiabatically following the magnetic field. This requires the curvature of the field to be small and the field bias to be large. Suppose the atoms would cross a region of the low field. In that case, the adiabaticity condition is easily broken, and the Majorana flop into an untrapped state is possible [6]. The cloverleaf style trap provides a large bias, at the minimum, to prevent these spin flips [44]. Another way to prevent the spin flips is to use a time-averaged orbiting-potential trap (TOP) [49].

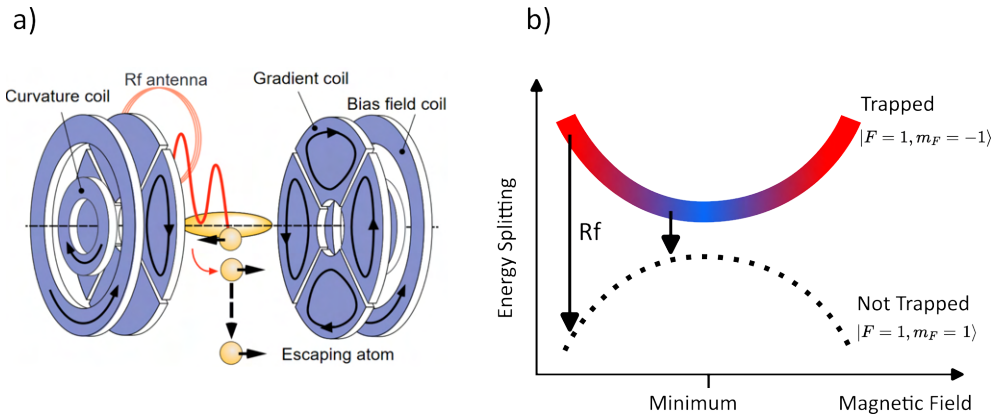

Figure 6: Magnetic trapping and evaporative cooling. Figure a) shows the schematic design of the cloverleaf Ioffe-Pritchard magnetic trap. The atoms are confined to a minimum magnetic field with a non-zero bias. Figure b) shows how the trapped and untrapped state changes their detuning with a magnetic field away from the minimum. The antenna provides the field for the RF transition between the two spin states. The frequency is ramped from large detuning toward small detuning, gradually releasing the hot atoms from the cloud. Figure a) is adapted from Reference [6].

1.4.1 *RF Induced Evaporation*

The high-energy atoms should be released to evaporate in the magnetic trap while the remaining atoms rethermalize through elastic collisions. The larger the kinetic energy of the atoms, the higher they climb up the potential, and the larger the magnetic field B they experience. As shown in Figure 6 b), this leads to a position-dependant detuning between the trapped and un-trapped states.

To release the high-energy atoms from the trap, the RF frequency is tuned to the splitting between the trapped and untrapped hyperfine state of Rubidium caused by the magnetic field at the edge of the trap. When these atoms transition at the equipotential surface of the magnetic trap, they are in resonance with the RF field.

After thermalization, the frequency of the RF field is lowered to evaporate the next portion of atoms. This process is done continuously, ramping from $\sim$ 60 MHz to $\sim$ 0.5 MHz [44]. This can increase the phase-space density of the cloud by six orders of magnitude [6].

1.5 OPTICAL DIPOLE TRAP FOR ALKALI ATOMS

The far-off-resonant optical dipole trap (ODT) is an essential technique for trapping atoms. Unlike magneto-optical traps, which operate with magnetic field gradients and light close to the D_2 line, an ODT uses the light shift to generate a potential almost independent of the internal state of the atoms. This yields the advantage of controlling the external degrees of freedom while the internal states can be used to "do physics." The following summary follows the references [50], and [23] for the light shift.

The general principle of the light shift results from the second-order time-independent perturbation theory of non-degenerate states. In a multi-level atom - like 87Rubidium - the energy shift of state $|i\rangle$ due to the presence of the field $\mathbf{E}(\mathbf{r},t) = \mathbf{e}E(\mathbf{r})e^{-i\omega_L t} + c.c.$ is given by

$$\Delta E_i = \frac{I(\mathbf{r})}{2\epsilon_0 c\hbar} \sum_j \mathcal{R}e \left\{ \frac{|\mu_{ij}|^2}{\omega_{ij} + \omega_L + i\Gamma_{ij}/2} + \frac{|\mu_{ij}|^2}{\omega_{ij} - \omega_L - i\Gamma_{ij}/2} \right\}. \tag{8}$$

With $\mu_{ij} = \langle e_i|\,\mu\,|g_j\rangle = c_{ij}||\mu||$ the dipole matrix element, and $\omega_{ij} = \omega_i - \omega_j$ being the transition frequency. When using light with a detuning larger than the fine structure splitting $\omega_{ij} - \omega_L = \Delta_{ij} = \Delta \gg \Delta_{Fs} \gg \Delta_{Hfs}$ but close enough to neglect the fast rotating term, the light shift potential is equal to the result of the two-level atom picture in zeroth order

$$U_{dip}(\mathbf{r}) = \frac{3\pi c^2 \Gamma}{2\omega_0^3 \Delta} \left(1 + \frac{1}{3} \mathcal{P} g_F m_F \frac{\Delta_{Fs}}{\Delta} \right) I(\mathbf{r}) + \mathcal{O}\left(\frac{\Delta_{Fs}^2}{\Delta^2} \right). \tag{9}$$

Here $\mathcal{P} = 0, -1, +1$ is for π-, σ^-- and σ^+-light. Also, g_F and m_F are the Landé factor and the magnetic quantum number. That means in the simplest picture, the potential is proportional to the light intensity, and the "efficiency" is given by the frequency-dependent polarizability of the atom $\alpha(\omega_L)$ [42]:

$$U_{dip}(\mathbf{r}) \approx -\frac{\alpha(\omega_L)}{2} I(\mathbf{r}). \tag{10}$$

Figure 7 shows a single red detuned beam trapping atoms. The atoms are confined to the beam's intensity profile as described by the above equation, showing an elongated shape.

The general perturbation theory is overkill to get the big picture of how an ODT works. Still, the internal degrees of freedom become relevant for smaller detunings, causing vector- and tensor-light shifts [50].

Finally, a 1D lattice can be created by retroreflecting the light from a mirror and fixing the boundary condition. The self-interference gives a factor of two in the electric field and hence a four-fold gain in intensity and trap depth.

Assuming that the spatial mode of the retro reflectance is mode matched, one can approximate the gaussian potential for small energies as:

$$U(r,z) = -4U_{dip}(\mathbf{r}=\mathbf{0})\cos(kz)^2\left(1-2\frac{r^2}{\omega_0^2}-\frac{z^2}{z_R^2}\right). \tag{11}$$

The lattice depth is often stated in units of recoil $E_r = (\hbar k)^2/2m_{Rb}$.

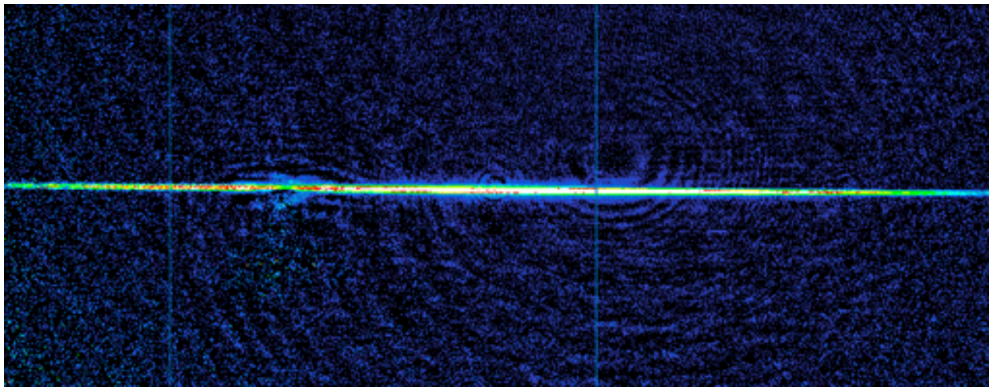

Figure 7: Absorbion image of Rubidium atoms in an elongated optical dipole trap, formed by a single red detuned beam in the science chamber of BEC4.

Part II

THE GROUND LOOP BREAKER SYSTEM

This part will feature the design and testing of a ground loop breaking system for digital and along signals, used in a cold atom lab. Disclaimer: I am not an electrical engineer, nor have I years of experience developing electronics. I am a physicist trying to understand and use the resources he has to control the things he tries to understand. If in doubt, contact your nearest professional or refer to *The Art of Electronics*, by Paul Horowitz and Winfield Hill.

2

THE HUMMING SPEAKER

"A cable is a source of potential trouble connecting two other sources of potential trouble." — Unknown [51]

When entering a laboratory for experiments with cold atoms, like BEC_4, the first thing that stands out is the abundance of cables running throughout the space. It becomes clear that electronics play a vital role in these experiments, alongside optics and lasers.

I began working in BEC_4 with only a basic understanding of analog circuitry from my undergraduate studies and had to quickly educate myself on electronics. I learned that controlling atoms in the lab is similar to conducting an orchestra, where all instruments must function properly to achieve the desired outcome. AMO physics is an interdisciplinary field. I did not initially realize the importance of understanding the devices controlling the lasers, polarizers, high currents, and more for the smooth operation of a cold atoms lab.

In experiments with cold atoms, such as creating a Bose-Einstein condensate (BEC), a precise and synchronized sequence of steps is essential for success. Electronics play a crucial role in this synchronization process.

Firstly, electronic devices such as timing and signal generators control the sequence of steps in the experiment. These timing signals trigger the various laser pulses, power supplies, microwave sources, translation stages, and more to cool and manipulate the atoms.

Secondly, electronic devices such as data acquisition (DAQ) cards and field-programmable gate arrays (FPGAs) are used to send, collect and process data to and from the experiment. This data is used to monitor the experiment's progress and adjust the timing and intensity of the optical and laser pulses as needed. However, many of the analog feedbacks from the experiment are just sent to oscilloscopes for surveillance.

Lastly, using a ground loop breaker, which will be discussed in detail in the following sections, is crucial to avoid interference and noise in the signal. This device isolates the different electrical circuits in the lab, ensuring that the important signals used to control and measure the experiment are not affected by outside interference. It is a vital component that does not require much attention as long as it functions properly.

Overall, electronics play a vital role in synchronizing and controlling the steps in an experimental sequence with cold atoms. Without precise timing and control of the electronic devices, the experiment would not be able to achieve the desired outcome.

2.1 THE PROBLEM

A centralized server system controls every device through various communication protocols. It is the Physicist-Atom interface; in the case of BEC4, it is called Cicero [52]. Many devices are required, and all must be timed accordingly for an experimental sequence to function. Those devices can be categorized depending on the signal they receive as analog and digital[1]. Digital meaning Transistor-Transistor Logic (TTL) signals with 0 V meaning "off" and 5 V meaning "on", and analog voltage outputs being capable of sweeping between ± 10 V with a 12-bit [53] or 16-bit [54] depth. The digital and analog signals are generated on specialized National Instruments (NI) cards housed on PCI slots on motherboards. The Physicist tells Cicero to generate an experimental sequence, and Cicero then coordinates the NI cards. A "breakout" board redirects the signals to different devices. And meters of BNC cable finally carry the information to their destination. Analog signals, for example, determine set points for the PID controller, coordinate current sweeps for magnetic field coils, determine the RF power in AOMs, or set the angle for polarizing waveplates. Digital signals are used to trigger devices and turn on different apparatuses. For example, they switch an RF source on and off for a Rabi flop.

Usually, all these signal-receiving devices, under the control of the signal-emitting NI cards, are connected to a power outlet. The terminals of the outlet are Live, Neutral, and Ground. The first two provide the power for the devices, whereas the last one – Ground – is a safety requirement for users and a voltage reference for devices. This non-ideal ground wire provides an electrical connection between the emitter and the receiver through the wall, almost invisibly. In the case of BEC4, the signal emitter is the motherboard on the computer with the NI cards, and the receiver is any other device connected to these cards. This is not too bad at first.[2] No, the complication in the lab arises when we want to send a signal from the NI cards to the device, for example, that regulates an AOM. By making another connection

1 Of course, there are also communication channels like USB, RS232, and GPIB, but those (TTL and analog) are the more important ones that need and can be timed to the microsecond

2 Imagine how absurd it would be if it were a problem when we would plug in the toaster and the water cattle at the same time in the morning.

and transferring a voltage signal concerning the ground, we connected the "Grounds" of two devices now in two different ways, once through the signal carrying BNC cable and once through the power sockets in the wall. Since the BNC cable uses this ground component for signal transfer, it creates a topological loop, a Ground-loop[3].

Similar to how it arises in the lab, a ground loop in audio systems is created when there are multiple paths for the electrical current to flow. This can be caused by multiple devices connected to the same electrical circuit or different devices connected to different circuits that are not properly isolated. The result is that a slight voltage difference between the grounds of the different devices can cause a current to flow through the low-impedance path, creating unwanted electrical noise and a humming speaker [51].

Figure 8 shows a schematic arrangement of such a system. These peripheral devices are connected to a power outlet; hence, both devices' grounds are connected through the wall. A ground loop is formed if the output on the emitting and/or receiving end is not floating concerning that outlet ground. This loop of non-ideal[4] wire has the effective functionality of an antenna. This leads to a strong AC effect. Hence, it can pick up inductive electromagnetic noise from devices in or outside the lab and add a noisy background to the ground. This can be an issue since some labs in the CUA also report seeing the influence of the elevators nearby[5]. Since the ground also acts as a reference for the emitter, this noise will be on the transmitted signal.

The wallplug ground connections' limited resistance is another less important consequence. This prevents the outlets from having two precise voltage references by causing a slight DC voltage drop across their grounds. The solution to the problem is to devise a way to "break" the second ground connection of the signal path. Since two types of signals are transmitted, two solutions will be presented - one ground loop breaker (GLB) device for the digital NI cards and one GLB for the analog NI cards.

3 Some music enthusiasts may be familiar with this issue. Ground loops can create a humming sound coming from the speaker.

4 Meaning the wires have resistance, creating a voltage drop if a current is driven through them

5 "Not unnaturally, many elevators imbued with intelligence and precognition became frustrated with the mindless business of going up and down, up and down, experimented briefly with the notion of going sideways, as a sort of existential protest, demanded participation in the decision-making process and finally took to squatting in basements sulking." - Douglas Adams

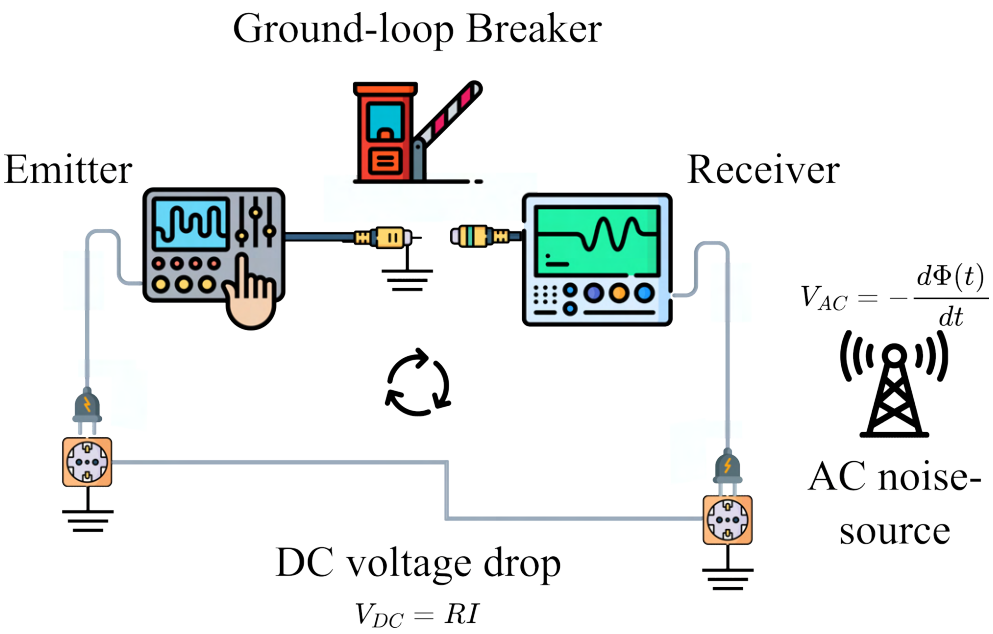

Figure 8: Schematic of a simple ground loop between two devices. Both devices are connected to the wall plug, and the outlets are assumed to be connected inside the wall. The signal-emitting device sends a voltage referenced to the ground to the receiving device. The receiver measures the incoming voltage relative to its ground and executes a step in the experiment. The composite system forms a ground loop if the signal ground is not floating.

2.2 THE IDEA TO SOLVE THE PROBLEM

One way to prevent such a ground loop is to add a "middleman" - depicted by a red toll station in Figure 8 - between the signal source and the receiver by completely breaking the wire connection between the sender and receiver. In one way or the other, one needs to introduce two independent grounds on each end. In the case of a digital signal, the heart of the ground loop breaker is formed by an optocoupler. These optocouplers turn a voltage signal into a stream of photons, and a photodiode then turns those photons back into a voltage signal, thereby breaking any wire connection. For analog channels, the signal is buffered by an instrumentation amplifier (INA) powered by an external floating power supply and then forwarded to the receiver. The INA only detects the voltage difference between the two input pins, rejecting DC common mode. This unreferenced signal requires an individual power supply per output channel. Both techniques introduce two different ground references on either side of the GLB.

Although this system already exists in the BEC_4 lab, the number of available channels is limited, and the capacity is exhausted. In addition, the system in place has also proven inaccessible for maintenance or debugging.

Therefore, the new system should be modular, easy to use, and extend. The 19-inch Rack Mount Euro-Card system provides a good platform for such a project. The idea is to have a backplane printed circuit board (PCB) directly distributing signals between cards. These cards then either provide input to the network or output. Each output card is a PCB containing all the necessary components to buffer the signal and break the ground loop.

The design requirements can be summarized as follows:

- **Modular and easy to access**. Both the digital and analog isolation solutions should be euro-card-system compatible.
- **Low noise.** The analog signal directly controls experimental parameters and should have minimal distortion.
- **Low latency.** since all signals pass through a GLB, the delay should be minimal.
- **Manual override toggle for TTL channel.** It has been proven convenient to have a manual interface for digital channels.

3

DIGITAL GROUND LOOP BREAKER

As mentioned in the introduction, the heart of the digital ground loop breaker is a high-performance optocoupler [55]. Its basic operating principle is depicted in Figure 9. The two main components in the IC are the LED and the photodiode. An individual source with a separate ground pin GND_i powers each. When the voltage V_I is high, the LED will light up, and the photodiode will receive it, causing the output voltage V_O to rise with a maximal propagation delay of 22 ns [55]. This two-step process cuts the physical connection between the grounds GND1 and GND2.

Functional Diagram

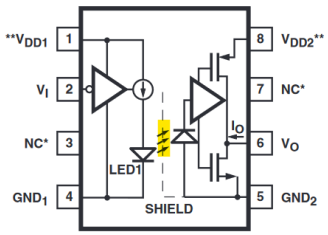

Truth Table

V_I Input	LED1	V_O Output
H	OFF	H
L	ON	L

Figure 9: Functional diagram and truth table of the optocoupler HCPL-0723. Pin 1,4 and 8,5 power the emitting LED and the receiving photodiode, respectively. The TTL signal arrives at pin 2 as voltage V_I (referenced to GND_1). The internal LED1 is lit when the voltage threshold of ~2 V (High) is reached. The output voltage V_O (referenced to GND_2) on pin 6 will also be high as the photodiode receives a photon flux. The simple logic is also shown in the truth table on the right. The Figure is adapted from reference [55]

Now it seems like all the problems of ground loops are removed, but one still must avoid connecting the two grounds with the same power source. This means we need two floating power supplies for each optocoupler. In principle, all the grounds on the emitter side of the optocoupler can share a ground and be powered by a single supply. Introducing an SMD DC-to-DC converter on the board is a rather noisy but cheap solution. At the cost of creating a lot of switching noise on the power line, it breaks the wire connection. It's a DC-(AC-AC)-DC like a transformer, where the -AC-AC- part breaks the physical connection by using an inductive transmission. Although the inner working principles of DC-to-DC converters can vary widely, the basic result is isolation between the two ground potentials from the input and output

of the device. This solution is fine for the digital TTL channel since noise doesn't affect the system much. On the other side, the rise time and timing are more important.

3.1 PCB DESIGN

The design for the digital GLB card is based on a 5 V input power supply. To properly isolate the signal, a DC-to-DC converter [56] is used to convert the input to 12 V, which is down-regulated to a clean 5 V by a voltage regulator (L7805). Three DC-to-DC converters are used for one card with two optocoupler channels. One is used to power the infrared emitting LEDs of the optocoupler, while the other two are used to isolate the circuitry for each output channel from each other.

As shown in the design schematic 10, the power distribution and channel selection on the left side of the board take up more than half the space. The small optocoupler ICs are positioned on the left boundary of the Channel1/2 section. The outputs of the optocouplers are then directly forwarded to the respective BNC outputs. This allows for a compact and efficient design while ensuring proper isolation and signal transmission.

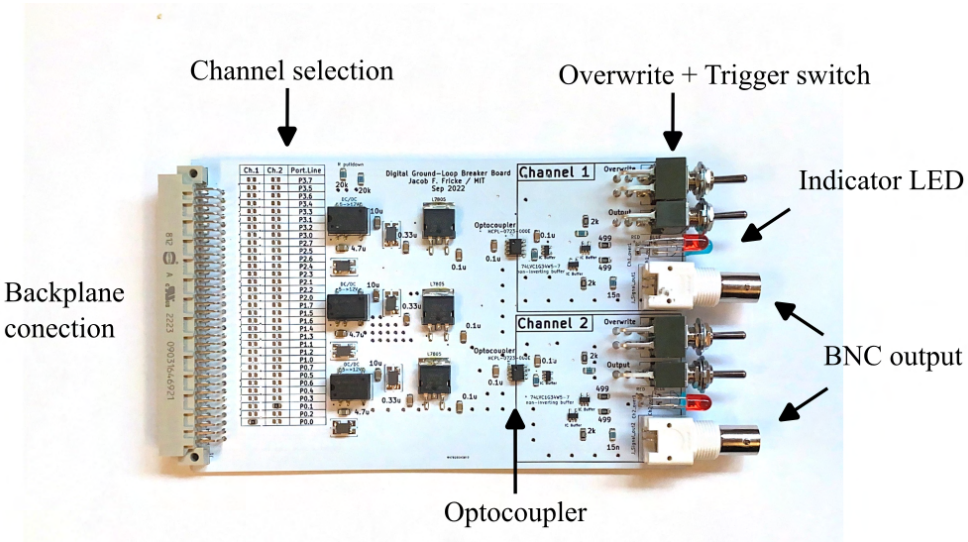

Figure 10: Design drawing of the digital GLB PCB. The card can forward two TTL channels from the NI cards to the BNC connector. The channels can be selected by soldering jumpers to the desired port line surface mount.

The digital isolation board is designed to feed-forward isolated TTL signals, which are used as triggers or "on" switches. Two indicator LEDs at the user interface indicate the output status, making the board more user-friendly. A blue LED lights up when there is a 5 V (logical 1) output po-

tential on the channel and remains off when there is not (logical 0). Additionally, two mechanical toggle switches per output channel control the Cicero-independent output state.

The first way to control the output of the TTL is via software on the Cicero platform. However, a physicist can also generate the TTL signal by flipping a toggle switch and entering the manual override mode. Now the red LED will light up, and the BNC output is completely software independent and can be controlled by the second switch. When executed, the blue LED and the 5 V output can be turned on manually. This produces a different result: when the manual toggle is flicked, the output is not a single rising flank but a repeating step-like oscillation until the signal remains high. This is due to the mechanical effect of "switch-bounces," as the toggle is spring-loaded and jumps up and down on the contact until it remains in contact. Existing solutions, such as a double NAND gate [57], could be implemented in future versions to avoid this. Still, since we can also override the TTL in software, it was considered over-engineering. It's good to keep that phenomenon in mind if a device misbehaves because it appears to receive multiple triggers[1].

1 The camera trigger is known to cause unexpected behavior when used in manual mode, probably due to switch bounces.

4

ANALOG GROUND LOOP BREAKER

Analog signals are used to control continuous variables in the experiment. The signals from the NI cards are bipolar, meaning they can cover the range from negative -10 V to positive +10 V relative to the ground. For TTL signals, noise does not play such an important role. In most applications, the devices communicating via TTL are only interested in the value above a threshold or signal's rising/falling flank. This changes for the analog system and can be illustrated by a simple example.

Many PID boxes take an external reference to regulate. The other input comes from an in-loop measurement. The difference between these two voltages - the error signal - is minimized by the PID by sending feedback to the system. If a Laser has intensity noise, an active feedback system using an AOM can chop away power on demand, stabilizing the intensity. The PID box then tries to minimize the difference between the NI card voltage reference signal and the photodiode measurement voltage. Since the PID box can't differentiate between the noise from the Laser and the noise from the reference voltage after taking the difference, the PID box will add it to the error signal. The external noise is then falsy added onto the Laser by the PID's feedback since the resulting Laser intensity minimizes the PID's internal error. Hence bringing external noise onto the PID loop will add it directly onto the thing we try to stabilize.

Of course, if the output of a device is directly proportional to the analog voltage from the NI card, then every noise from the NI control will reappear in the experiment. A good example are the high current power supplies. If the power supplies are operated in voltage control, the 60 Hz noise on the control will propagate to the current output. These currents drive coils and generate magnetic fields, now with a 60 Hz noise contribution.

As discussed in the introduction, the noise in signal transmission is easily increased if a ground loop is formed. 60 Hz line noise and its harmonics are often easily picked up by the loop in the lab. Hence in order not to generate a bottleneck in the experiment, the analog GLB should be below the noise level of the NI card output itself, thereby setting the biggest design constraint.

In the previous section, I introduced the idea of "breaking" the ground loop by using an optocoupler and isolating the DC-to-DC converter. The following section will use a different approach: impedance control by an

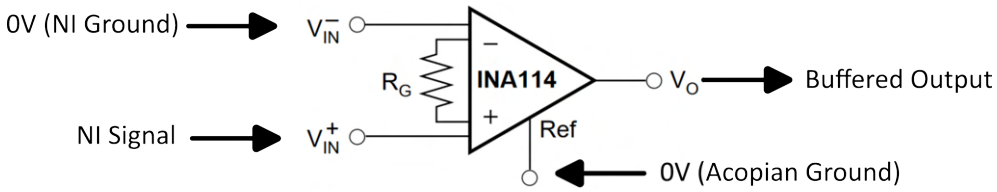

Figure 11: Simplified schematic of the working principle of the instrumentation amplifier INA114. The resistor R_G determines the device's gain and is set to unity. The ground and signal pins of the NI card are connected to the negative and positive poles of the INA, respectively. The output voltage Vo is then referenced to the floating ground of the linear Acopian [58] power supply. The Figure is partially adapted from reference [59]

instrumentation amplifier. The approach is similar to before. Get a device with a floating/isolated ground and add the unreferenced signal on top of that. In this case, the optocoupler is replaced by an instrumentation amplifier, and a quiet bipolar linear power supply replaces the DC-to-DC converter with a floating ground. The analog GLB design utilizes the INA114 [59] instrumentation amplifier, and its operation principle is depicted in Figure 11.

The INA114 has two input pins and a gain control set by an external resistor. The resistance R_G is chosen such that the device is operating in unity gain, thereby forwarding the voltage difference between the input without multiplicative factor. The common mode voltage between the two input pins is rejected by ~96dB [59]. The difference signal is then added onto the reference from the floating ground power supply and sent to the receiving device in the lab.

The power supply of the INA114 determines the operating range. If the device is powered with ± 5 V, but the input voltage is 10 V above the reference, the output will rail at 5 V, the momentary operating limit. To prevent the output from "railing", the INA114 is supplied with ~ ± 12 V giving a few volts of headroom for the ± 10 V range coming from the NI cards[1].

Since the noise performance of the analog GLB is important for the operation of some devices in the lab, I will discuss the implementation of the active filter after the INA's output and how the noise on the output changes when the floating ground source is altered.

1 If the output signal can't follow the Cicero command input up to a certain value, then this might be a good start for troubleshooting. Usually, the output is railing for a certain polarity, and the power delivery to the INA114 is malfunctioning.

4.1 ACTIVE FILTER

A filter's purpose is to suppress the signal's spectral components causing disturbances in the experiment while trying to keep the relevant frequencies unchanged, determining the stopband and passband, respectively. Our experiment uses analog signals to mainly adiabatically ramp signals between constant plateaus. The timescale at which those ramps can be performed is related to the bandwidth available. The frequency of the 3 dB point is inversely proportional to the rise time. To ramp a signal within 1 ms, the 3 dB point should be at least 400 Hz. This sets the right corner of the passband.

The disturbances that can be caused for the atoms in the optical lattice are band excitations, which are approximately the splittings of the first two harmonic oscillator levels. For 87Rb in a 1064 nm lattice with 30 E_r lattice depth, this gap is around ~ 22 kHz [23]. Those frequencies should already be within the suppressed stopband of the filter.

The filter, displayed in Figure 12 is chosen to have a -60 dB suppression at 10 kHz and a passband with a -3 dB point at 1 kHz. The filter design is chosen to be an active 4th-order Bessel filter to achieve this fast suppression. Active filters have the advantage that they are not a load to the signal input and can therefore be stacked more easily. Furthermore, they can control their output impedance somewhat [60]. The downside is often the higher costs and complexity compared to passive systems.

In previous experiments, the fasted wanted modulation of the lattice was around 1 kHz, which was on the order of the on-site interaction energy U [40]. This frequency is close to the 3 dB point, where getting a homogeneous amplitude response is difficult. Therefore, there should be a convenient way to bypass the filter by easily changing the 3 dB frequency.

Analog Devices' Filter Wizard [61] selected the optimal parts for the desired response. The components can be changed if the system requires another use since the topology of the PCB is universal for all 4th-order filters. The simulated step response of the filter is below a millisecond and hence fast enough for most applications.

The core of the active filter is the operational amplifier ADA4075-2 [62] from Analog Devices. The same linear floating power supply powers it as the INA114. It is a surface mount component with ultra-low noise performance, ideal for filter applications. Its low impedance output also helps buffer the GLB card's output signal. If bypassed, the output is only provided by the INA114 directly, which has a relatively high output impedance and can't provide currents beyond 5 mA [59]. This can lead to a limited output voltage range. A pre-amplifier with unity gain and bandwidth beyond 10 kHz

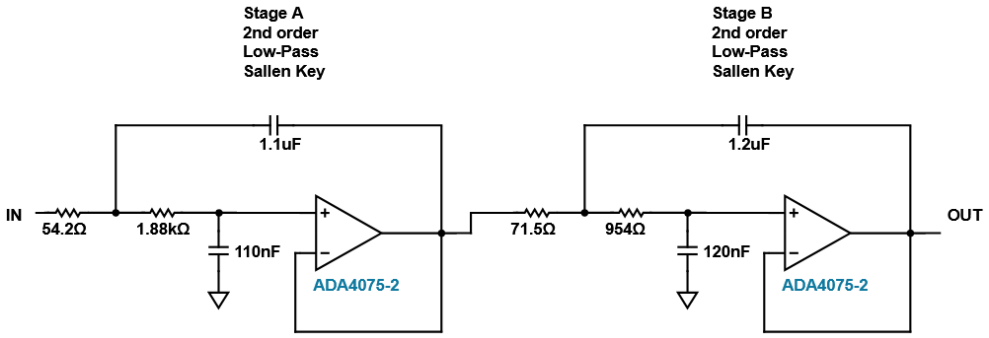

Figure 12: The 4th order Bessel filter [60] using the ultra-low noise operational amplifier ADA4075-2 [62]. The parts are selected by The Filter Wizard from Analog Devices. The -3 dB point, determining the passband, is chosen at 1 kHz. The -60 dB point is chosen to be at 10 kHz. The parts are chosen to be capacitance heavy to reduce Johnson noise. The Figure was created using the Filter Wizard from Analog Devices.

following the output of the GLB is recommended to prevent the higher voltage outputs from being limited.

4.2 NOISE PERFORMANCE

The Analog GLB device is built around a precision instrumentation amplifier, the INA114 from Texas Instruments [59]. The instrumentation amplifier operates in unity gain, and a fourth-order active filter processes its output. The instrumentation amplifier has a large common mode rejection and is thus only sensitive to the differential input of the signal. Since the input lost its absolute reference, the INA114 needs another source to act as a voltage reference. The common ground of the floating power brick plays this role. It provides the INA114 (and the filter OPAMP) with ± 15 V and defines the new ground.

That means the stability and noise of the output signal are primarily set by the accuracy of the floating ground potential provided by the power supply. Therefore, different types of power supplies were compared to evaluate their performance. The types of power supplies that were compared were: linear power supplies, switching power supplies, and battery-powered power supplies. Each power supply had pros and cons, but the most suitable one for the application was chosen based on its noise characteristics, stability, and overall performance.

- **Recom** switching AC-DC converter, 10 W ± 15 V [63].
- **Acopian** linear AC-DC converter, 5 W ± 15 V[58].

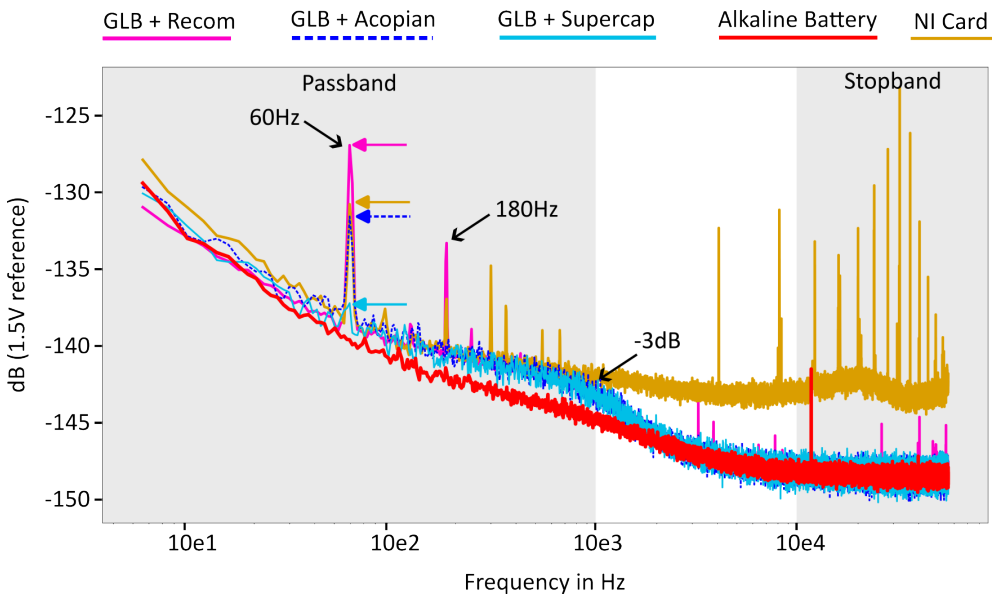

Figure 13: AC RMS noise measurement of the analog GLB and comparison to references. The red curve is the measured noise spectrum of a 1.5 V alkaline battery. It represents the noise floor of the measurement device. The yellow curve is a 1.5 V signal measured directly from the output of the NI card. The remaining three curves - GLB+Recom, GLB+Acopian, and GLB+Supercap - show the GLB card's output noise when the 1.5 V input comes from a NI card, but the voltage reference source for the instrumentation amplifier is changed. Furthermore, the background color indicates the Passband and the Stopband starting at ~10 kHz of the active filter on the GLB card. Also, the 60 Hz noise peak and its third harmonic at 180 Hz are indicated for each measurement.

- **Supercapacitor** powered supply.

The Acopian is a linear power supply and uses a transformer to step down the voltage from the input power source to the desired output voltage. A rectifier follows the transformer to convert the AC voltage to DC voltage, and a filter circuit to smooth out any remaining AC ripple [60]. Linear power supplies are known for their ability to produce a very stable and clean output voltage. Still, they are generally less efficient than switching power supplies and tend to be larger, heavier, and more expensive.

On the other hand, the Recom is a switching power supply that uses a switching device, such as a transistor, to rapidly switch the input voltage on and off, thereby creating a "chopped" version of the input voltage. This chopped voltage is then passed through a transformer and rectifier to create a DC voltage [60]. The input voltage switching also produces a significant amount of high-frequency noise, which can be filtered out with a specialized

output filter circuit. Switching power supplies are generally more efficient than linear ones and can be designed to be smaller, lighter, and cheap [60].

Thirdly since both linear and switching AC-DC converters are expected to show noise on their DC output, an array of capacitors is used as the ultimate reference DC power supply. We used many supercapacitors in series to get enough capacitance and a voltage range of ± 15 V around the common ground.[2]

To determine the noise performance of the board, a 1.5 V alkaline battery was used as a precise input reference. The noise spectrum of the battery was measured with the Picoscope [64] and is shown as a solid red line in Figure 13. This measurement says not so much about the noise of the battery but the limitations of the noise floor of the Picoscope. The actual noise floor of the battery signal should be beyond the measurement capabilities of the Picoscope.

The second reference measurement is the undisturbed output of a 1.5 V DC signal from the NI card shown in yellow in Figure 13. The yellow spectrum shows a much higher noise floor at high and low-frequency values than the red battery spectrum. In addition, there are prominent spectral peaks at 60Hz and its harmonics and above ten kilohertz. The GLB card ideally should not add but only subtract noise to that NI spectrum.

The noise spectra of the GLB+Recom (Pink), GLB+Acopian (Blue dashed), and GLB+Supercap (Turquoise) show a significant reduction of power beyond the filter cutoff at 1 kHz. The value quickly reaches the noise floor of the Picoscope and coincides with the red battery reference. In the high-frequency section, their performances seem to be similar, judging by the measurement result.

At the low-frequency end, their performance differs more drastically. Looking at the 60Hz peak in Figure 13, one can see that the pink, blue and turquoise peaks are all of different heights. Furthermore, the pink Recom switching AC-DC converter-based spectrum is the only one showing significant peaks of 60Hz harmonics.

The best performance measure by the amount of AC RMS noise, as may be expected, is achieved by using the supercapacitors as a power source. No significant 60 Hz peak is visible. The Recom switching converter delivers the worst performance. The spectrum displays many peaks in the passband of the active filter. This means much of the 60 Hz line noise is leaking into the system. The Acopian linear converter is performing better than the Recom. The difference between the Recom and the Acopian is not only the increased

2 WARNING! It can be hazardous to work with these capacitors if not handled with care since they can release several amps of current at 30 V when accidentally shorted, which can hurt.

price tag but also the fact that it is a linear power supply with a lower 60 Hz noise peak.

The downside of the capacitor approach is the bulkiness and the overhead it produces during operation. Whenever the sequence is running, the capacitors discharge and supply the GLB. Then there would be the need to implement a timeslot in the sequence where the devices would be charged again. Since this can take several seconds, it could be done during MOT loading since that is not very sensitive or at the end of the sequence. In any case, it creates more overhead. The other downside is the required voltage, which creates bulkiness. To reach a voltage of 30 V between the two poles, one needs 18 supercapacitors connected in series, each the size of a glue stick.

The Acopian linear converter was selected for the final design after this analysis. The performance of the Acopian AC-DC converter was further improved with the new ultra-low noise, high performance, linear voltage regulators LT3045 [65], and LT3094 [66]. They regulate the provided 15 V down to a convenient 12 V, which is still enough for the INA114 not to rail. External precision resistors determine the output voltage value. The external set capacitors can influence the $1/f$ noise behavior of the device and are adapted according to the datasheet.

4.3 PCB DESIGN

The PCB of the analog GLB card can be segmented into two regions. The signal is processed by the top region containing the channel selection, the INA114, and the active filter. The bottom area on the card is reserved for the Acopian AC-DC converter and the voltage regulators. The left end of the card is equipped with the standard DIN connector. The right side has a single BNC output and two SubMiniature version A (SMA) solder pads to connect an external battery for ultra-low noise and ultra-paranoid operation.

As depicted in Figure 15, the final version contains an additional feature, a pin header interface. This enables the jumping of the output filter and the use of an arbitrary external power supply. These two features allow for the modulation of analog signals beyond the optical lattice's excitation energy and possibly lower noise performance below the filter cutoff.

The surface mount pads around the operational amplifier are chosen to be universal, such that it is easy to change the values of the filter but keep the topology of the board for future applications.

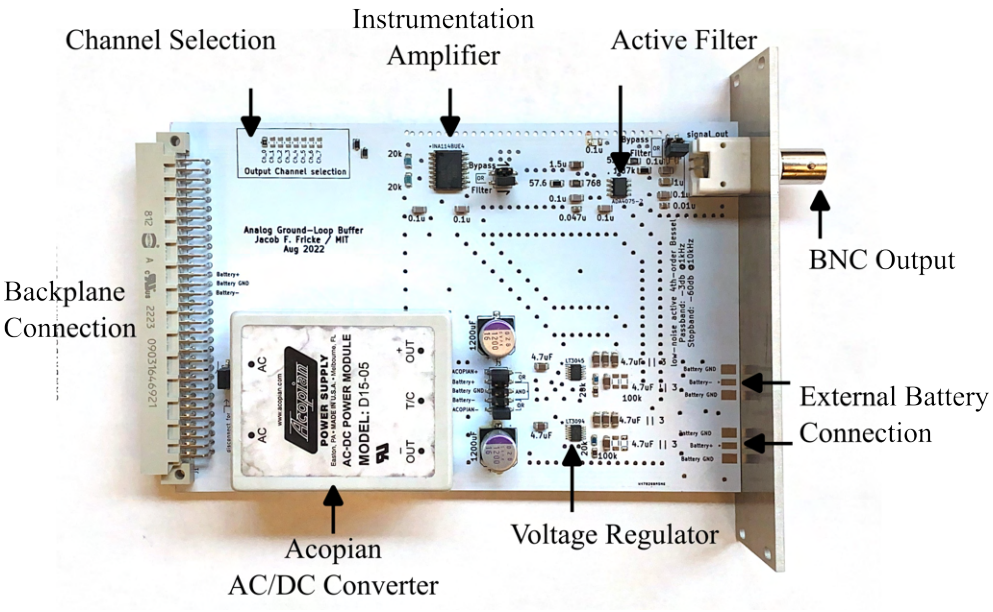

Figure 14: PCB design for the analog GLB card. The card can be divided into two main parts, the upper half, relevant for signal processing, and the lower half, in charge of power preparation and distribution.

A small but important part is the pulldown resistor at the input of the instrumentation amplifier. It provides a pathway for a small current to flow to the ground of the Acopian. If the input line from the NI card were solely connected to the INA, then charges would build up on its input, and the voltage would exceed the common mode rejection abilities. So instead, the voltage is kept in a reasonable operation range by introducing a high resistor of 20 kΩ as described in the datasheet [59]. It is like preventing a balloon from flying away by holding it with a little string.

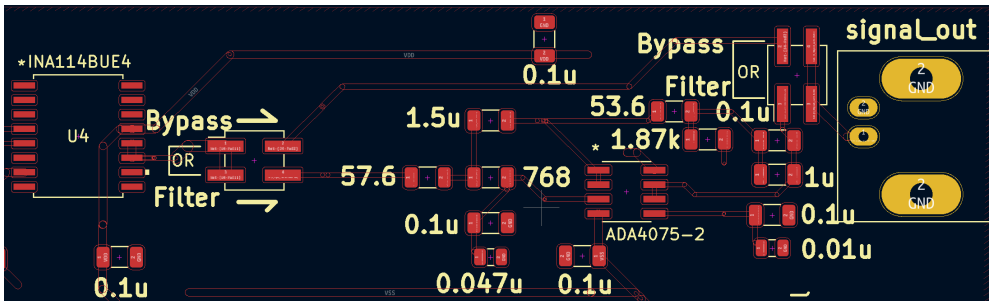

Figure 15: PCB design for the active filter stage. The signal from the INA114 (left) can either be directed directly to the BNC output (right) or passed through a filter (middle). All the footprints around the OPAMP ADA4075 are 1206_3216Metric, except for some additional small capacitor pads of size 0805_2012Metric.

5

THE INTERFACE

One design improvement over the previous generation is how the signal from the NI cards is distributed to the GLB cards and, from there on, to the devices in the lab. The previous method was to have an external breakout box, which would reroute the signal from the specialized NI cable to an array of BNC plugs. Then each device had an input and an output BNC connection. Each GLB device was a loose PCB lying in a larger metal box.

The situation for the previous generation digital GLB system was also very unflexible and challenging to service. The channels were all connected to a big PCB, which was difficult to remove from the housing. In addition, when

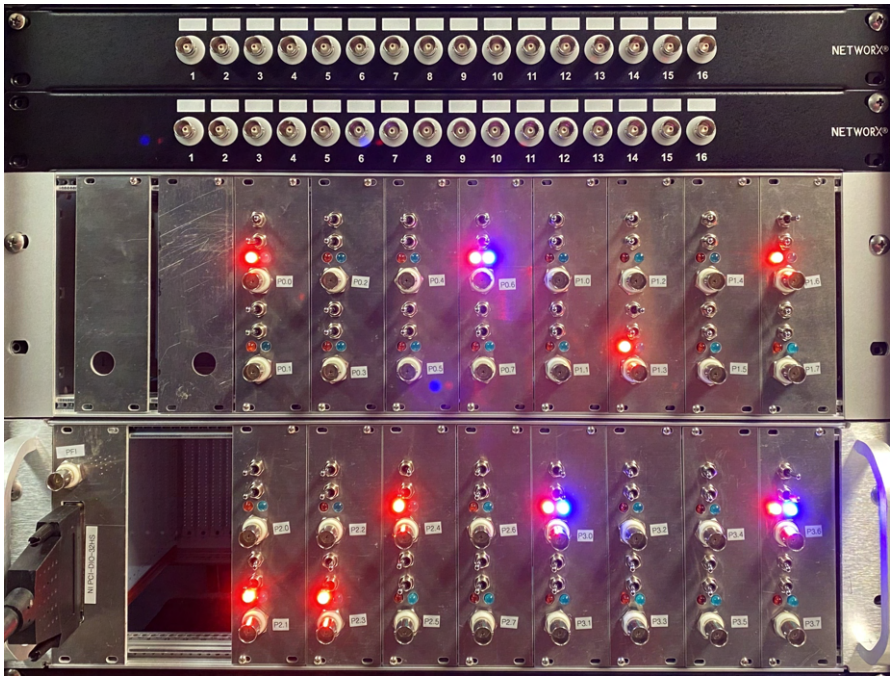

Figure 16: Photograph of the front end of the digital GLB system. Two stacks of 8 GLB cards in the rack are mounted to their backplane. Each card houses two output channels. The bottom leftmost card is a signal breakout for the NI cable to the backplane. The LEDs indicate the status of each BNC output. All the cards can be individually shuffled around in the rack without changing their functionality. The top two black rows of BNC connectors can distribute the signals from the rack to different locations in the lab.

one channel was malfunctioning, all the channels needed to be removed, interrupting the operation of the experiment.

The euro-card rack system shown in Figure 16 and Figure 17 can now distribute signals and power through a backplane PCB, onto which all the GLB cards can be plugged. A breakout card is also plugged into the backplane, building the connection between the NI cable and the backplane. This results in a very flexible way of how the GLB system operates.

The PC is also housed in the same rack, containing the NI cards on the motherboard's PCI slots. Since we already had remaining legacy NI cards with PCI connectors, we set up a legacy motherboard[1] compatible with at least three PCI slots. The PC's name is Zurich, and it provides two analog cards with eight channels each and one digital card with 32 channels.

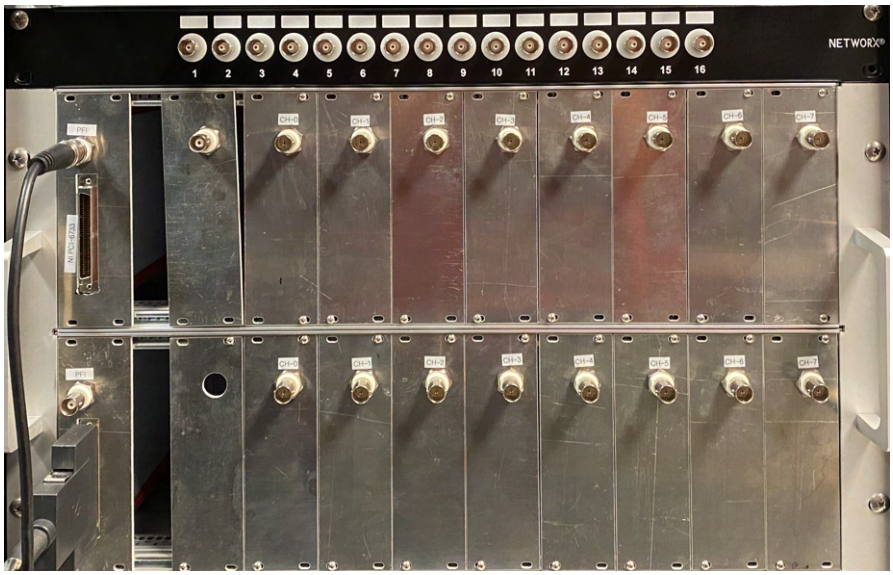

Figure 17: Photograph of the analog GLB front end. Each of the rows houses eight cards, with each one having an output port. The leftmost card slot provides the analog signal input for each row. The BNC cable visible in the breakout slot is the external clock signal. All the cards can be shuffled around in the rack without changing their output channel.

A Cicero-controlled FPGA device provides a variable timebase as an external clock signal [52]. A BNC interface on the breakout cards connects the clock signal to the PFI0 pins after the pin header connector selects the desired channel. From there, the clock signal is routed to a single NI card on the motherboard of the Zurich server. The NI cards are connected to the motherboard through their rtsi ports via a ribbon cable[2].

1 Motherboard model: ASUS Prime H310-Plus LGA1151 (300 Series) DDR4 HDMI VGA ATX Motherboard

2 See Cicero user manual for internal hardware connections.

Another feature is that because of the backplane, all the signals from the NI card arrive on each GLB card. Only now is the channel selected. This means once a channel is set on the physical GLB card, it doesn't matter where it is arranged on the rack. Similarly, for the signal distribution adapter housing the NI cable. It only matters that the card is plugged into the correct row, not the column, since each backplane routes the signal only on its level.

Part III

THE NEW SCIENCE CHAMBER

"It is a mistake to think you can solve any major problems just with potatoes." - Douglas Adams. But the following Part will present the features of the new scientific apparatus designed to enable single-site resolution microscopy of Rubidium. It will show the constituents of the vacuum chamber and discuss a coating failure, which occurred during the bakeout. The implementation of a lateral ODT steering mechanism is presented. Finally, it is shown how this ODT steering is used to align the atoms to a cross ODT in the science chamber and create BEC by forced evaporation.

6

THE NEW VACUUM SYSTEM

Most cold atom experiments use similar structures. Light is prepared at a separate laser table and sent using fibers to the main experiment table. The main component of the experiment table is a vacuum chamber, which is often covered and hidden by optics and cables. The ultra-high vacuum (UHV) conditions inside protect the atoms from colliding with the background gas. Without it, the cooling of the atoms to degeneracy would be impossible.

The vacuum system is divided into several compartments, each serving a different purpose, often including a science chamber and a main chamber for optical access, as shown in Figure 18. The main cooling process for achieving quantum degeneracy takes up a lot of space and limits optical access for introducing lasers for science. As a result, the main and science chambers are often used for different stages in the experimental sequence.

6.1 DESIGN OVERVIEW

The main chamber shown in Figure 18 hosts the fields and light responsible for cooling and preparing the Rubidium atoms, bringing the gas close to degeneracy. It starts with an oven section where the "hot" Rubidium vapor is released into the angled Zeeman slower. The reason for the angled slower is the improved horizontal optical access it creates. The atoms are then caught by the MOT and transferred into a cloverleaf-style Ioffe-Pritchard magnetic trap after a short round of molasses cooling. Here the cloud is further cooled by forced RF evaporation close to the transition temperature of BEC [44]. The cloud is then loaded in an optical dipole trap, using red detuned 1064nm light, and transported into the science chamber. All details of the main cooling chamber can be read in the thesis and paper of Erik Streed [44].

The main chamber and its optics were almost entirely untouched throughout the upgrade. The MOT optics were, unfortunately, partially connected to breadboards that needed to be removed, and hence the MOT boards were mounted on a different anchor. But after realignment, the MOT could quickly be restored. Also, the vacuum in the main chamber was never broken due to the gate valve between the main chamber and the science chamber, which was closed before the upgrade. Although imperfect, it could keep a

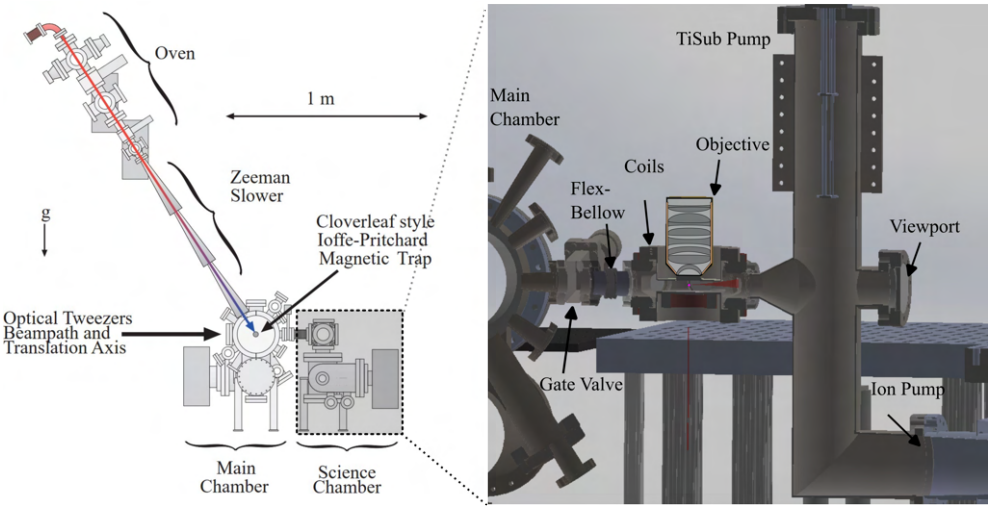

Figure 18: The Figure shows the old vacuum chamber design in BEC_4 on the left. It is divided into four main parts. The oven, the Zeeman slower, the main chamber, and the science chamber. The Zeeman slower is angled such that the horizontal axis is free for transporting the atoms from one chamber to the other with an optical tweezer. The Figure on the left is adapted from the thesis of Erik Streed [44]. Depicted on the right is the new science chamber vacuum complex cross-section. The left side indicates the connection to the main chamber via a gate valve and a flexible bellow. The octagonal science chamber is connected to titanium sublimation and an ion pumps, a residual gas analyzer, and an ion gauge (the last two are not visible in the Figure). The high NA objective (to scale) is placed without a positioning stage directly on the reentrant top viewport. A water-cooled copper coil surrounds the top and bottom reentrant viewports.

pressure around 10^{-10} Torr. All of this ensured a quick recovery to operation when the building phase had ended.

The new science chamber complex, shown in Figure 18, is segmented into a pump system, a CNC-machined octagonal stainless steel chamber with new reentrant viewports, a high NA objective, new magnetic coils, and a unibody breadboard around it.

The new system is connected to the main chamber tract with a flexible and fully contractable bellow connected to a gate valve, as shown in Figure 19. The bellow prevents a rigid connection between the two chambers and makes positioning the new science chamber relative to the main chamber more delicate.

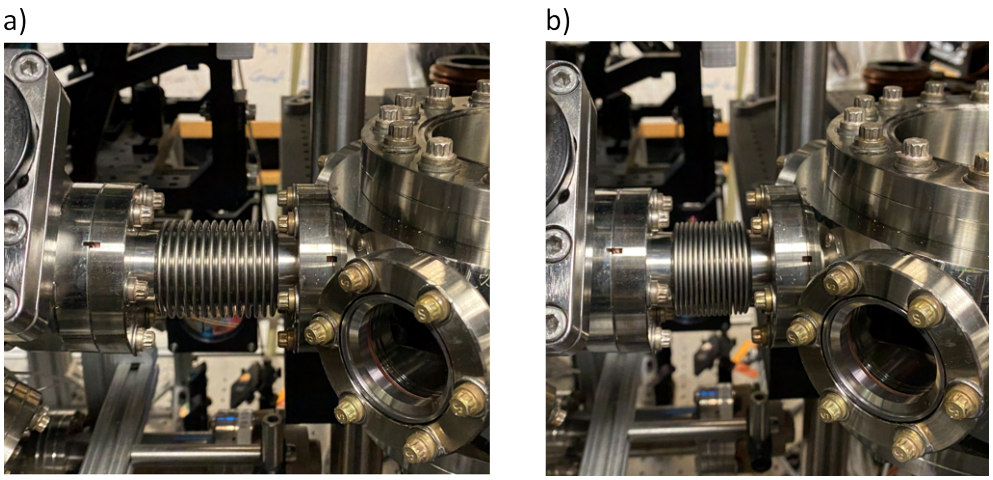

Figure 19: The Photographs a) and b) show the bellow connection between the main chamber (left) and the science chamber (right) in the uncontracted and fully contracted state, respectively. To the left side of the bellow is the gate valve, separating the main chamber from the science chamber.

6.1.1 *The Pump*

The pump section consists of a titanium sublimation pump and an ion pump, which has a turbo pump connection on it[1]. A residual gas analyzer (RGA) and an ion gauge are also on the same connection.

The titanium sublimation (TiSub) pump consists of an elongated filament inside the TiSub tower's vertical cylinder. When activated, the filaments emit titanium onto the chamber wall and act as a getter pump for non-noble gases [67]. The critical step is that it must be ensured to keep the titanium filaments away from the line of sight of the viewports. If not, a layer of titanium will be deposited on them.

An ion pump is required to achieve UHV and pump noble gases such as Helium and Argon. A strong electric field releases free electrons from the anode, which orbit in a cyclotron motion due to a strong magnetic field. Those electrons ionize the atoms and adsorb them onto a titanium surface cathode [67]. As the gas ions collide with the cathode wall, they will also sputter titanium inside the pump. The pump in the new system has a pumping speed of ~ 75 L/s.

The chamber body has six side viewports and two reentrant viewports at the top and bottom. Two additional ways of optical access are along the transport direction from the main chamber to the viewport on the TiSub tower.

1 We did not use the NEG pumps like many other new experiments.

The vacuum structure is mechanically supported by a set of height-adjustable posts on the TiSub tower and a height-adjustable platform below the heavy ion pump. Using those adjustable feet, the orientation of the chamber could be precisely adjusted before mating it with the bellow on the main chamber.

6.1.2 *Unibody Breadboard*

The previous generation of the experiment had several unconnected breadboards around the chamber with optics on them. The independent motion of those breadboards relative to each other caused instabilities in the optical path lengths. This would lead to phase or amplitude noise in the lattice and disturb the experiment.

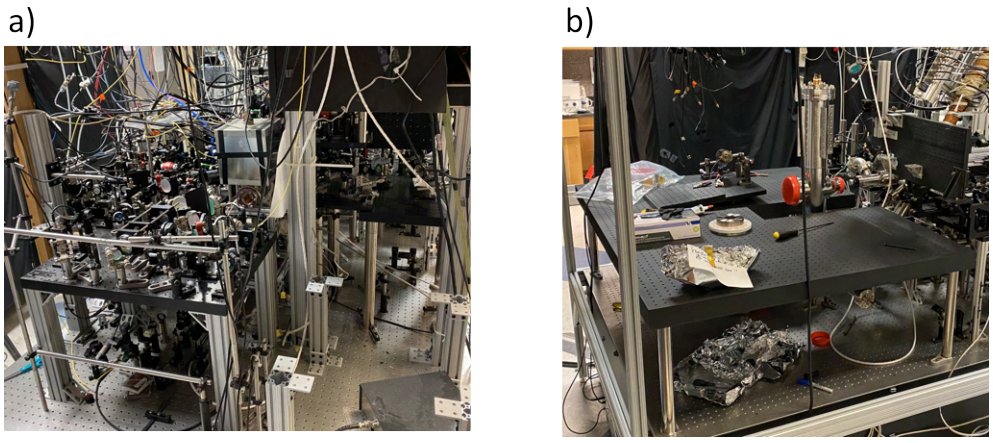

Figure 20: a) Old experimental setup, with multiple rectangular breadboards surrounding the science chamber. b) New U-shaped breadboard design surrounding the new vacuum parts.

There have been attempts to dampen the breadboards by using specialized mounts to improve stability, but that was unsuccessful. In the new upgrade, a big unibody breadboard is introduced. It wraps itself around the new vacuum system like a "U", giving ideal optical access and hopefully better stability.

The individual free-standing breadboards also bring a degree of modularity to the setup. This made the disassembly of the experiments straightforward[2] since the breadboards around the chamber could be removed with the optics sill mounted. This modular design will also be adapted to the new machine by mounting multiple units to the big unibody breadboard.

2 Never have lead beads in a hollow post, supporting a breadboard, without the proper plugs installed at the bottom.

6.1.3 *The Reentrant Viewport*

The viewport at the top of the octagon chamber is crucial in the setup. It is the bridge between the atoms in a vacuum and the optics collecting their fluorescence outside it. The atoms are transported along almost a direct line from the main chamber to the science chamber. Since it is simpler to bring the objective to the atoms than the atoms to the objective, the top viewport is lowered into the chamber such that the objective is positioned at a working distance of ~1 cm (5 mm fused-silica, 6.5 mm vacuum) from the rough center of the chamber.

6.1.4 *RF Antenna*

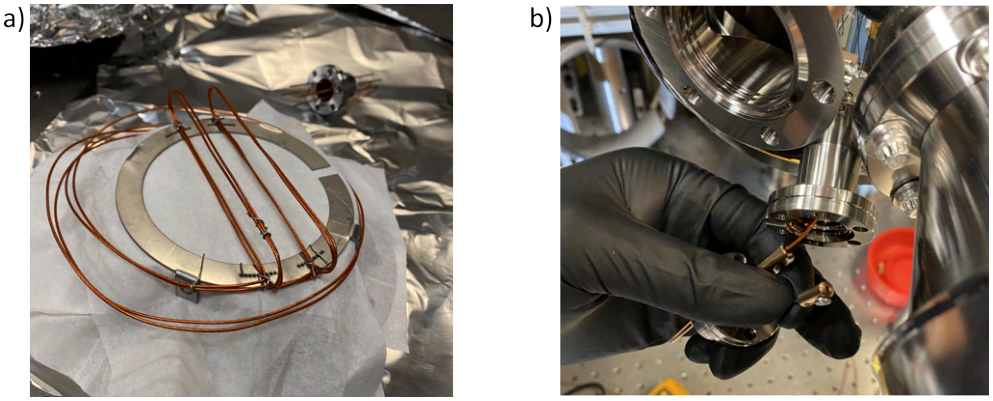

Figure 21: a) Square RF antenna in Helmholz configuration, mounted on sheet metal clamp. b) Feedthrough connection between the leads of the antenna and the outside of the chamber.

An in-vacuum antenna was planned to increase the Rabi frequency for RF transitions in the hyperfine states of Rubidium. A square RF antenna depicted in Picture 21 a) made from Kapton insulated wire is mounted on a stainless steel clamping ring. The antenna is mounted to the clamp by using a vacuum-compatible twisted wire. The clamp is placed onto the bottom viewport inside the octagon chamber. The leads of the RF antenna wire are connected to the outside of the vacuum system by a special feedthrough piece shown in Figure 21 b). The wire is partially stripped from the Kapton and connected to the copper leads of the feedthrough by a hollow cylinder with screw clamps.

Since the risk of creating a shorted connection with the chamber is high, we benchmarked the RF power arriving outside the chamber when the an-

tenna is driven with a specific power at a determined frequency. If a short occurs, the response of the antenna will decrease or vanish.

6.1.5 *Magnetic Field Coils*

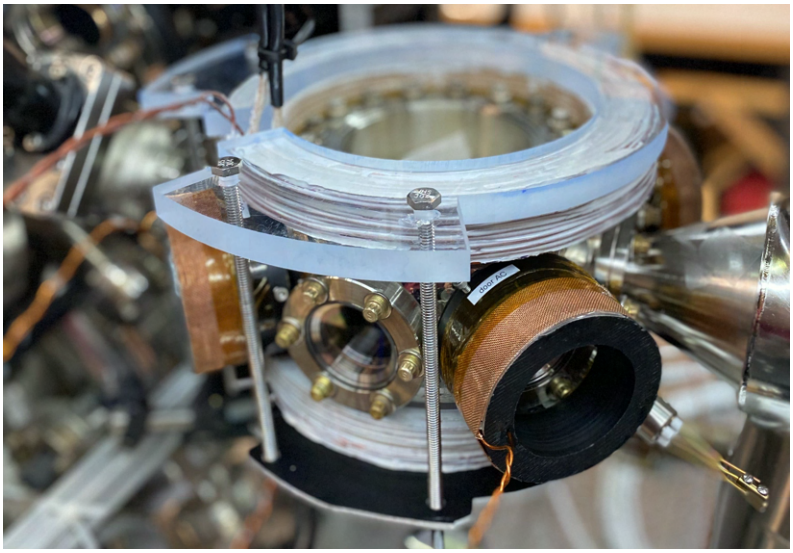

Figure 22: Science chamber with magnetic field coils attached. The coils on the side viewports are housed in a black plastic mold and are not water-cooled. The gradient coils are placed on the flange and clamped together by brass rods mounted to acrylic and aluminum plates on the top and bottom of the coils, respectively. To the lower right end of the octagon, one can also see the copper leads for the RF antenna.

The new science chamber, as shown in Figure 22, is equipped with three kinds of magnetic field coils. Two primary gradient coils at the chamber's top and bottom, four biasing coils on the side viewports, and two additional biasing coils in the vertical direction. The water-cooled gradient coils can produce a gradient of ~50 G/cm @ 100 A, and the side coils ~0.8 G/A.

The gradient coils will be used to select a single layer in the field of view of the objective. By detuning the resonance of certain RF transitions in Rubidium between neighboring layers, one can drive only a specific layer into a state that is insensitive to a resonant blowout pulse [26].

The bias coils can compensate for stray fields and adjust for imperfections in the gradient coils. They provide the bias along the lattice direction and can change the atoms' response in the spin-dependent lattice, where science happens in BEC4 [38, 40].

6.2 DOUBLE BAKEOUT

After the chamber was assembled, the vacuum was regained over several days by a pump down and baking procedure. Different pumps in the system can function at different pressure ranges to create a continuous operation. In addition, a bakeout is required to eliminate the water film and any residual crap in the chamber [67].

a) b)

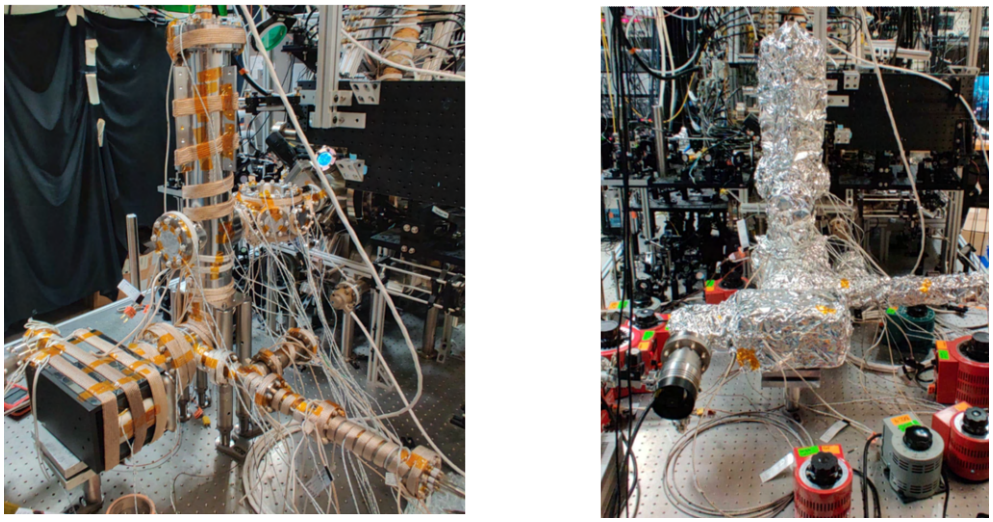

Figure 23: a) The Picture shows how the vacuum chamber is wrapped in heating tape for baking. Thermocouples are attached for temperature control and monitoring. The bottom right part of the chamber shows the RGA and ion gauge attached to the bottom of the TiSub tower. Photograph b) shows how the whole chamber unit is covered and wrapped in aluminum foil. In addition, some of the used Variacs used to heat the tape are visible.

The pump-down starts by connecting a dry-scroll roughing pump to the system until its operation limit is reached. Then the turbomolecular (turbo) pump, connected to the ion pump through an angle valve, is started. The angle valve is closed later to disconnect the system's turbo and roughing pumps. This is necessary since neither the roughing nor the turbo pump can maintain a large enough pressure differential for the ion- and titanium sublimation pump to operate effectively.

While the turbo pump runs, the chamber is heated with variac-powered heating tape. The individual tapes are wrapped around different system parts to create controlled heating. Not all components should be heated to the same maximal temperature. The imaging viewports should be heated not higher than 160°C. Some parts of the ion pump should also be handled

carefully since the ferrite magnets could demagnetize at high temperatures. Otherwise, it is desired to increase the temperature as high as feasible. As plotted in Figure 24 a), individual thermocouple readers around the chamber monitored the temperature during the procedure to ensure proper heating. In particular, the displayed data originates from the thermocouple reader on the side of the top imaging viewport, which sits between the atoms and the high NA objective. Throughout the ten days of bakeout, the temperature of the imaging viewport remained below 160°C.

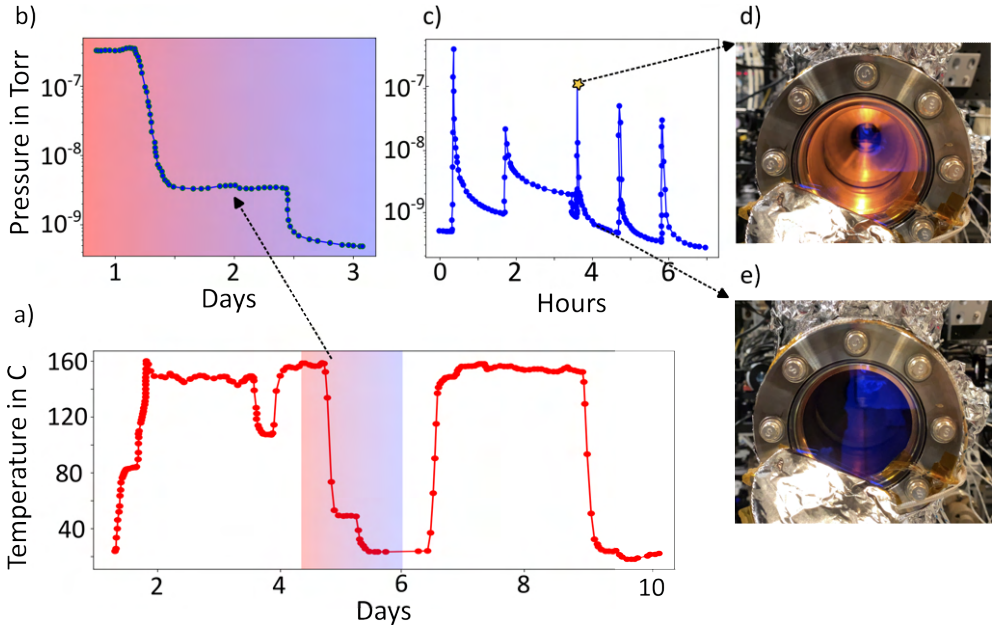

Figure 24: a) The Plot displays the temperature monitored close to the reentrant imaging viewport over several days. The temperature was varied between room temperature and ~160°C. b) The Plot displays the pressure change measured by the ion gauge as the temperature is lowered for the first time. c) The pressure was measured at low temperatures in the chamber while the titanium sublimation pump was fired repeatedly for several hours. Photographs d) and e) display the glowing light from the hot titanium filaments, which are visible when the pressure is at a peak. The pressure settles to a plateau when the filaments cool down again and stop glowing.

When the pressure reached the lower 10^{-7} Torr[3] region, we decided to cool down the system to degas and fire the filaments of the ion gauge, residual gas analyzer (RGA), and titanium sublimation pump. The cooldown was needed since the RGA head could not be operated at bakeout temperature. Also, we hoped that the time we baked was enough and we could proceed.

3 1 Torr ≈ 1.33 mBar or 1 mBar ≈ 0.75 Torr

Later we saw that the achieved pressure wasn't low enough, and we heated it again for a couple of days.

Figure 24 b) is a beautiful example that the pressure in the chamber sinks more than one order of magnitude during cool down. The second kink in the pressure occurred when the angle valve to the turbo pump was closed. After a first cool down to room temperature, we could observe the pressure to be higher than expected and ramped the temperature up for a second time.

The filaments of the titanium sublimation pump should be fired when the chamber walls are cold. That increases the sticking coefficient and supports the deposition. The filaments are fired by driving high currents through them and making them glow due to the heat produced by their resistance [67]. For each operation, the filament was supplied with 48 A for about one minute. The glow can be observed through the viewports, shown in Figure 24 d) and e). When the filaments are fired, the chamber locally heats up, causing crap surrounding the TiSub to evaporate, which is detected by the ion gauge, causing the pressure reading to increase as shown in Figure 24 c). After the reading reaches its pressure peak, the filaments are turned off, and the titanium on the wall acts like a getter pump, bringing the pressure to a lower plateau value than before. This step is repeated until the final pressure of $\sim 10^{-11}$ Torr is reached.

It is crucial to prevent a meltdown of the titanium heating filaments during operation. To get a sense of lifetime, we logged the resistance, current, and voltage drop across the filaments for each operation.

The vacuum chamber was covered in fiberglass and aluminum foil for isolation during the baking and pump-down procedure. When the chamber was uncovered, a broken coating of the top imaging viewport was noticed. The moment is captured in Figure 25 a). The coating was a high-reflective (HR) coating for 1064 nm and an anti-reflective (AR) coating for wide angles at 780 nm. We tested the coating briefly and decided that we could not use it for future experiments, and we had to discard the viewport.

The alternative plan B was replacing the top viewport with the bottom and making our spare viewport flange the new bottom viewport. None, except the original top viewport, were coated for HR at 1064 nm, which is required to construct a vertical lattice. Also, the thickness and flatness of the replacement top viewport are sub-optimal. The original optics design compensated for 5 mm thick fused silica in the diverging beam path of the fluorescence. The new window is only 4 mm thick, which would create aberrations without compensating for thickness. Furthermore, the replacement viewport is not as flat as the original one from plan A, creating more astigmatic aberra-

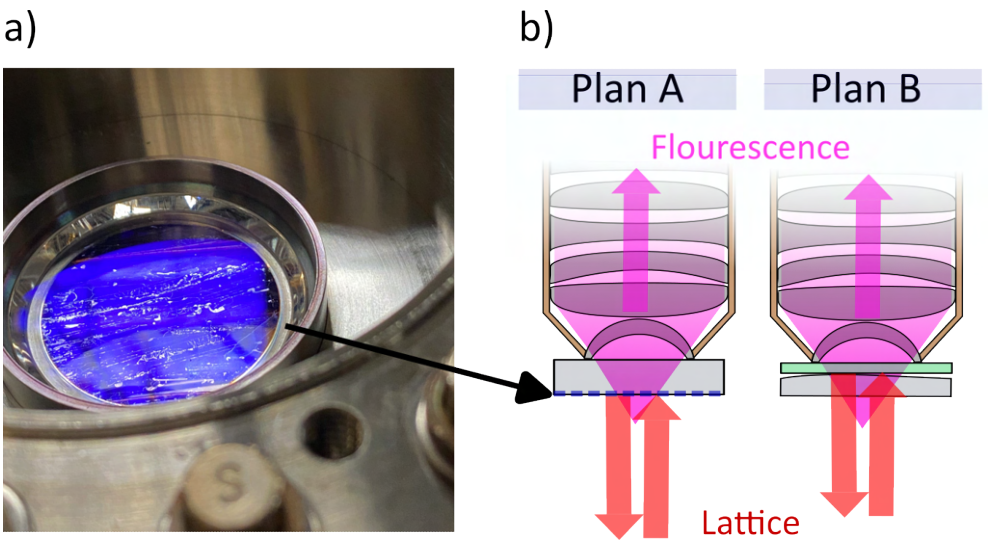

Figure 25: a) Photograph of the top imaging viewport after the baking procedure. The in-vacuum coating (1064 nm HR, 780 nm AR) failed and cracked into small elongated chips. b) The flat top viewport (5 mm thick) with the complicated coating from plan A was destroyed and replaced with a thinner and not-so-flat viewport without HR coating on the vacuum side. The wavefront aberration of the viewport from plan A was ~ 2λ. The lack of fused silica in plan B was compensated with a flat 1 mm HR-coated fused silica window. The wavefront aberration of the new 4 mm viewport from plan B is ~ 5λ.

tions in the imaging system. Those can be compensated by carefully adjusting the eyepiece.

Figure 25 b) schematically summarizes the differences between plan A and plan B. To compensate for the lack of silica and the missing HR coating, we introduce a flat and coated 1mm window between the vacuum viewport and the objective. In hindsight, this 1 mm correcting plate can also bring flexibility into the system since it enables the easy change of coating for the lattice beams.

Currently, it is still unknown what exactly caused the coating of the viewport to fail. The coating was done by Blue Ridge Optics. The vendor also did the coating for the objective. One hypothesis for the failure is that a large temperature gradient during baking causes stress in the viewport. Since the HR coatings comprise multiple stacked layers, the induced stress could lead to a crazing [68]. Another factor might also have been that the coating was never designed to be bakable or used in a UHV environment due to miscommunication between the vendors.

A similar problem was reported in the group of Waseem Bakr [69] (Page 16). Their original design also had an in-vacuum HR coating, which failed

after baking and pumping down. The HR coating failure forced them to proceed with an accordion lattice design. They also tried to reduce the stress on the HR coating of the reentrant viewport by not sonicating it in solvents. We did sonicate the HR viewport, and both our and their coating failed after baking and pumping down!

Eventually, we had to break the vacuum again, unmount the bottom and the top bucket, and swap and replace them. During the process, a continuous flow of Argon in the chamber was provided to avoid too much exposure to the atmosphere. Afterward, the chamber was wrapped the same night again, and a second baking and pumping process was started to restore the low pressure.

Currently, the chamber operates at a pressure of $\sim 2 \cdot 10^{-11}$ Torr.

7

THE HIGH NA OBJECTIVE

Imaging is a crucial tool in cold atom experiments, as it allows us to observe and analyze the behavior of ultracold atoms directly. Several imaging techniques are commonly used, including absorption, fluorescence, and phase contrast imaging. Absorption imaging involves illuminating the atomic cloud with near-resonant light and then measuring the amount of light absorbed by the atoms, which can be used to determine the density distribution and, indirectly, the temperature of the atomic cloud [6]. Fluorescence imaging involves exciting the atoms with a laser and then measuring the light emitted, which can be used to determine the position and distribution of the atoms [30]. These imaging techniques are essential for characterizing and understanding the properties of ultracold atoms and have supported many important discoveries in the field of cold atom physics, such as the proof of reaching BEC by observing atomic interference fringes [5, 70, 71].

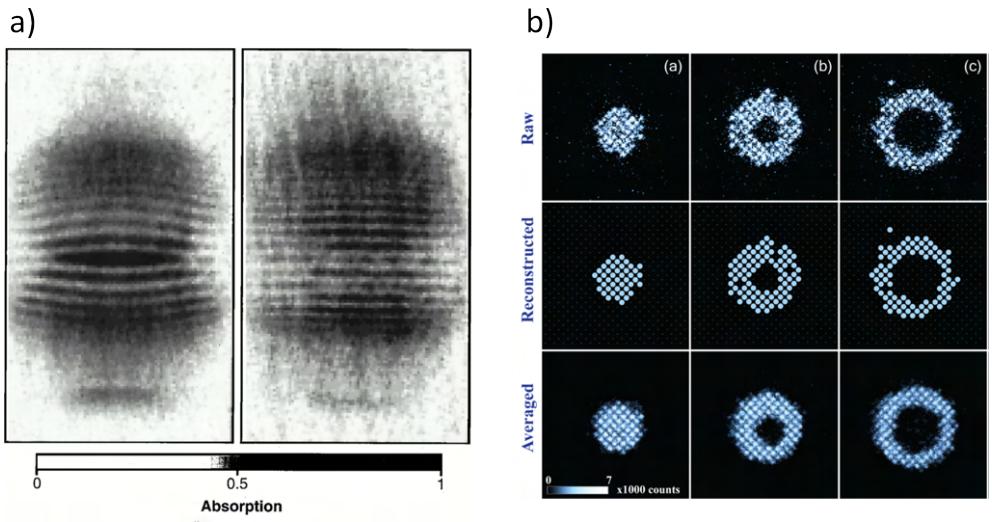

Figure 26: Figure a) shows the absorption image of two interfering sodium BECs. The fringes demonstrate the coherence properties of the BEC state. Figure b) shows the fluorescence of a Mott insulator state of bosonic Ytterbium in a 544 nm period lattice. The first row displays the raw data, the second row the reconstruction of the PSF, and the last row displays the average of multiple shots. Figure a) is adapted from reference [70]. Figure b) is adapted from reference [28].

In the case of fluorescence imaging, the system's resolution is ultimately determined by the detected wavelength λ, and the solid angle from which light can be collected, the numerical aperture (NA) of the objective [72]. Since the emitter of fluorescence, the Rubidium atoms, are point-like particles, the image through the finite aperture will show an Airy disk-like intensity pattern, also known as point spread function (PSF) [73]. The imaging system is considered diffraction-limited when it can reach the Rayleigh-limited resolution [27, 72]:

$$r = \frac{1.22\ \lambda}{2\ NA}. \tag{12}$$

This limit describes the distance at which two light-emitting point-like particles separated by r can still be distinguished from one another. In other words, the smaller the wavelength and the higher the NA, the higher the resolution that can be achieved. At this limit, the radial intensity distribution of the first PSF aligns its first intensity minima with the PSF of the second source separated by r [27]. In practice, the resolution of an optical microscope is usually limited by the diffraction of light through the low NA rather than by the imperfections in the optics.

For Rubidium, the fluorescence wavelength is 780 nm at the D2 line. When atoms are in the 1064nm lattice, their separation is $\lambda/2$, hence half a micron. Therefore, the required NA of the imaging system to distinguish two neighboring Rubidium atoms in the lattice would be $1.22 \cdot 780$ nm / 1064 nm $\approx$ 0.89. However, it is possible to distinguish the two atoms with a lower resolution since we have prior knowledge of the system, such as the lattice geometry. Still, one has to detect much more photons. Other elements with cycling transitions that have shorter wavelengths, like Dysprosium [18] and Erbium [29], can give an advantage in allowing a lower NA.

Since the required NA of the imaging system for in situ lattice imaging scales inversely with the lattice spacing, one can also imagine changing the scaling before collecting the fluorescence. This can be done by implementing an accordion lattice [74–76]. The period in the lattice scales with the half angle θ between the beams as $\lambda/(2\sin(\theta))$. The lattice spacing is changed by changing the angle between the interfering laser beams. If the angle is shallow, then a large spacing is created. When the beams are exactly counterpropagating, the angle is maximal, and the spacing is $\lambda/2$, where lambda is the lattice laser wavelength.

Another strategy can be to use the spontaneous transfer into a dark state. If atoms on a checkerboard grid are spaced closer to the Rayleigh limit, resolving the individual sources is difficult since their PSF overlap. When the atoms are randomly transferred into a semi-long-lived state during illumina-

tion, their PSF does not interrupt their neighboring atoms. This technique requires taking several images and then stitching them together in post-processing [77].

This upgrade in BEC4 aims to implement a high NA objective, enabling single-site resolution of atoms in optical lattices by collecting their fluorescence directly. The NA of the new objective is designed to be around ~ 0.8. Although the objective was tested and characterized by measuring the Strehl ratio of a SNOM fiber tip, the final resolution and performance of the imaging system are yet to be determined in the experiment. The objective will be placed outside the vacuum system with a working distance of ~ 6.5 mm in the vacuum and sit directly on the viewport.

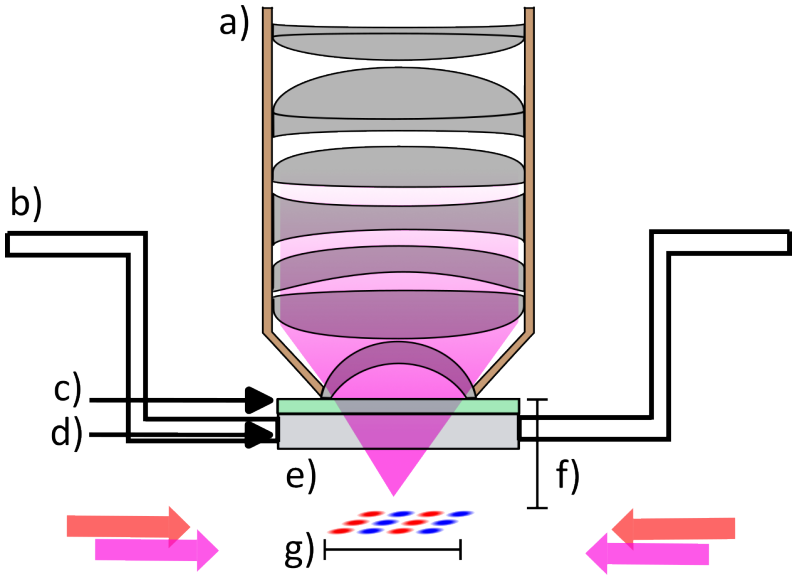

Figure 27: Schematic of the high NA objective setup. a) High NA (0.83) objective manufactured by Special Optics. b) Reentrant viewport for bringing the optics closer to the center of the octagon chamber, where the atoms are delivered. c) 1mm flat fused-silica window with a high reflective coating for 1064 nm and anti-reflective coating for large angles at 780 nm. This 1mm plate is not bonded to the vacuum viewport. d) 4mm thick fused-silica window bonded to the reentrant flange. It is coated with an anti-reflective coating for 780 nm on the vacuum side. e) Fluorescent light cone emitted from the atoms in the lattice as collected by the high NA of the objective. f) The working distance of the objective is 6.5 mm in vacuum. The performance of the objective is designed to have 5mm of fused silica followed by another 6.5mm of vacuum between the objective and the atoms. g) The atoms are arranged on a grid by lattice beams and illuminated to fluoresce. The imaging system's field of view (FOV) is estimated to be 50 by 50 microns with a depth of focus of ~1 μm.

The fact that the highly divergent light cone from the atoms must pass through the vacuum viewport sets stringent requirements on the flatness of the glass interface [38]. To maintain diffraction-limited performance, the wavefront aberrations must be minimized. Since the thickness of the glass is constant, the curved glass would leave collimated light unaffected. While ordering a flat piece of glass is easy, vacuum components are prone to curvature imperfections due to metal-to-glass bonding, which can stress the glass. There have been some efforts in BEC4 to bond a flat piece of glass to the vacuum-compatible housing by gluing it with a special epoxy. Still, the resulting bond always struggled to maintain the vacuum inside the test chamber.

Another design alternative [29] is to have the imaging lens in a vacuum to reduce the demands on viewports. This introduces other technical difficulties, such as mounting the optics in a vacuum and ensuring that everything is UHV compatible. It also reduces access to the objective.

Hence the previous generation of Ph.D. students decided to plan an outside vacuum objective as depicted in Figure 27. The objective is placed inside a reentrant viewport, directly standing on a 1 mm correction plate with no tip-tilt stage mounted to it. This design is simply relying on passive stability due to friction.

The in-vacuum working distance of 6.5 mm brings a lot of flexibility and accessibility to address the atoms with light. But this also requires some engineering in positioning the atoms to the proper distance from the objective. The depth of focus of only a micron gives no room for errors in position. The vertical confinement is provided by the vertical lattice, which is retroreflected from the 1 mm correction plate, resulting in several possible layers to load the atoms into. One big challenge is to robustly select the layer in the focal plane of the objective.

To summarize, the objective demands for the flat viewport and good optical access require the upgrade of the science chamber in BEC4. Some of the occurring astigmatic aberrations from the viewport can be compensated by tilting the eyepiece carefully. Also, the shallow depth of focus of the objective requires precise and flexible positioning of the atoms relative to the chamber, leading to the upgrade of the transport optical dipole trap.

8

LATERAL STEERING OF THE TRANSPORT OPTICAL DIPOLE TRAP

The two-chamber design brings the advantage of generating more optical access when needed. The challenge with this layout choice is bringing the atoms from one chamber to another. Longitudinal transport of cold atom clouds from one vacuum chamber to another has been demonstrated in various ways. The main idea is to trap the atoms in a potential minimum, which is then displaced. This potential can be of magnetic or optical nature.

Optical dipole traps can be focused at multiple locations by changing the arrangement of optics outside the chamber in various ways. The use of focus-tunable lenses, for example, enables the transport of atoms in ODTs without moving parts [78]. Another way is to use a one-to-one telescope that images a focus inside the chamber. By changing the distance of the focus on the object plane, the image will also be displaced without changing the trapping parameters [79]. Magnetic traps have also been successfully implemented for transport [80]. These magnetic traps can also move the atoms around corners in the vacuum system.

Our system uses a mechanical translation stage to move a lens and shift the focus of the ODT as described in [81]. The atoms, which sit in the focus of the ODT, are then transported as the lens changes position.

Most optical transport mechanisms can move the atoms along a one-dimensional line, which can be a bottleneck for some experiments. The following chapter will detail a lateral steering mechanism for the transport optical dipole trap in BEC4. The system is meant to be minimally invasive and will provide an additional lateral range of motion of 4mm of the ODT focus while maintaining μm precision.

8.1 THE PROBLEM WITH A GRAVITATIONAL SAG IN THE MAGNETIC TRAP

To transport the atoms from one vacuum chamber to the other, we load the atoms into an ODT and move the focusing lens with a translation stage. The focus of the ODT, and hence the atoms, can only be moved in one dimension: the direction of the translation stage.

The trajectory is fixed when one fixes the ODT's focus position at one point in space. Now let us assume one wants to drop off the atoms at a specific place in the vacuum chamber B, but the point where one wants to pick them up in chamber A is not on the trajectory.

This constraint was set in the previous arrangement, as the transport ODT drop-off was aligned to the lattices in the science chamber. It was impossible to control the beam in both places with static optics alone. It would have been complicated to readjust the drop-off position due to the lattice alignment.

Additionally, with the microscope upgrade in mind, we wish to position the atoms at their destination independent of their pick-up position. The microscope will determine the drop-off position by its working distance, the field of view, and the depth of field.

Previously, when the optical dipole trap (ODT) was loaded from the magnetic cloverleaf trap in the main chamber for transport, the gradient fields were decreased to let the trap expand. This is shown in Figure 28. Due to gravity and the large mass of Rubidium, the cloud will start to sag down [44]. The expanding magnetic trap makes loading into the ODT more likely

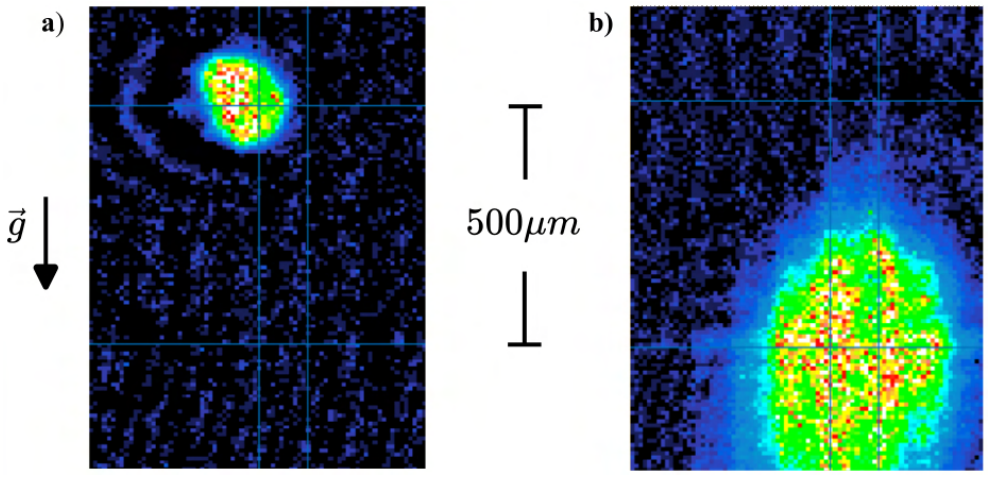

Figure 28: Absorption image from the side of the magnetic trap in the main chamber. a) Magnetic trap loaded from a compressed MOT. b) Magnetic trap and ODT after the gradient field was relaxed. The trap is expanding due to the reduced confinement and sagging due to gravity.

due to a larger overlap of the two. This alignment advantage at the pick-up position comes at the cost of a long loading time of ~6 seconds due to the decreased trap frequency in the magnetic trap. Two lateral degrees of freedom are needed to load and unload the atoms more flexibly. By implementing a lateral control of the ODT, one could keep the magnetic trap compressed and steer the tweezer to the atoms instead of letting the atoms rain onto the tweezer.

A simple method to implement this movement is replacing a fixed mirror mount with a motorized one. Then during the sequence, the mirror's alignment could dynamically steer the ODT's focus. However, the ODT alignment is very sensitive and needs to be placed precisely. Hence, replacing existing mirrors with motorized ones would mean a signal loss. To circumvent this, we wanted to implement a "quick fix" by inserting a fused silica window on a motorized gimbal mount. This step does not require the removal of optical elements from the existing beam path and can be removed if wanted. One only wants to add optics, but not remove or replace them, potentially saving time.

8.2 OPTICAL SETUP

The design idea is to insert a fused silica window at or around a conjugate plane of the ODT focus as depicted in Figure 29. One can introduce a translated focus point at the image plane by tilting a thick and flat AR-coated window at the object plane. The displaced focus of the conjugate plane is then collimated and focused down inside the chamber by a 2 inch, 500 mm focal length lens mounted on a translation stage.

The tilted window must be introduced at the conjugate plane of the ODT and not when the beam is collimated. by placing the window in the collimated path, only the trap angle would change rather than the position. This is because the light would still be collimated after the window; hence, the lens would still focus the collimated light at the focal point. But the beam would hit the last lens not in the center, creating an uneven NA of the beam, which results in a tilted trap.

Jongchul Mun described the z translation mechanism in BEC4 well in his thesis [82]. The stage model is Aerotech ABL2075, with a precision of up to 0.1 µm and a typical travel of 360 mm.

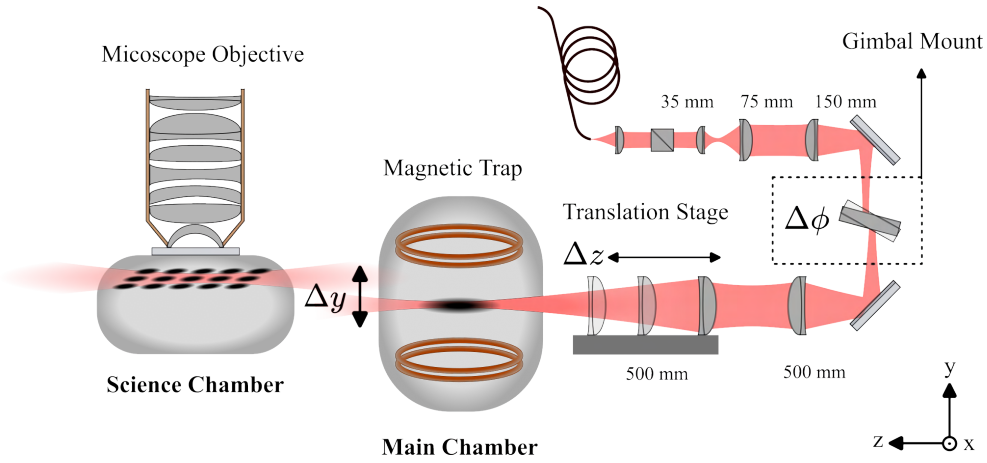

Figure 29: Schematic of the ODT transverse beam displacer working principle. After the light emerges from the fiber tip, it passes through two telescopes to expand the beam. The beam is then focused in the main chamber to load the Rubidium atoms from the magnetic trap. A final focusing lens is mounted on a translation stage and can transport the cloud along the z direction from the main chamber to the science chamber. A fused silica window is placed near one of the ODT's conjugate planes. It is mounted in a gimbal with two independent axes of rotation. The rotating window leads to a translation of the focus and a movement of the atoms in the x and y directions.

Since the lens must remain outside the chamber and can only come as close as touching the viewport, the focal length sets the largest distance that can be covered. The value of f=500 mm was close to the limit since making that number larger creates an even looser trapping frequency in the transport direction. Transport with such a long focal length can be challenging and can lead to losses since the atoms are mostly confined radially (orthogonal to the direction of transport) and the least axially (along the direction of transport).

Another parameter that influences the efficiency of transport is the three-body loss in the trap. It was observed in the past that transporting a degenerate cloud in the ODT leads to a low atom number efficiency. The transport efficiency was increased by stopping the forced RF evaporation in the main chamber's magnetic trap and transporting the cloud close to the transition temperature of BEC. That is the reason why in BEC4, a thermal cloud is transported from the main to the science chamber.

To get two degrees of freedom, i.e., translation in x and y, one can mount two fused silica windows on independently motorized rotators, controlling orthogonal axes. The solution for saving space in the setup is to implement a gimbal mount to steer a single window. The gimbal is depicted in Figure 32.

The gimbal mount's precision then determines the system's precision and stability. Another concern is not only the precision of absolute positions of the ODT but, as already mentioned, how we can minimize atom loss during transport. Jerk[1] induces density waves in a medium by inhomogeneous acceleration. These can lead to three-body collisions, and atom loss during transport [81]. The Z translation stage is already programmed to perform a zero jerk motion. That means that the rate of change in acceleration is close to zero. Although we can't eliminate the jerk, we can minimize it!

1 The derivative of acceleration.

8.3 GEOMETRIC OPTICS PICTURE

To get an estimate for the ODT displacement, one can use geometric optics approximations and Snell's law, as indicated in Figure 30, to find the displacement Δy of a ray with incident angle $\Delta\phi$:

$$\Delta y(\Delta\phi) = d\sin(\Delta\phi)\left(1 - \frac{\cos(\Delta\phi)}{\sqrt{n_{win}^2 - n_{air}^2\sin^2(\Delta\phi)}}\right). \tag{13}$$

Here d is the thickness of the window, and n_{win} is its index of refraction. From the drawing in Figure 30, the focus is also displaced in the direction of propagation of the beam by Δz. Since this shift depends on the angle of divergence α, it leads to small comatic aberrations, which can be neglected in our case due to the small diverging angles of the beam. The z displacement of a focused beam with divergence α, at symmetric incidence, is given by

$$\Delta z(\alpha)_{\Delta\phi=0} = \Delta y(\alpha)\frac{\sin(\alpha)}{1-\cos^2(\alpha)}. \tag{14}$$

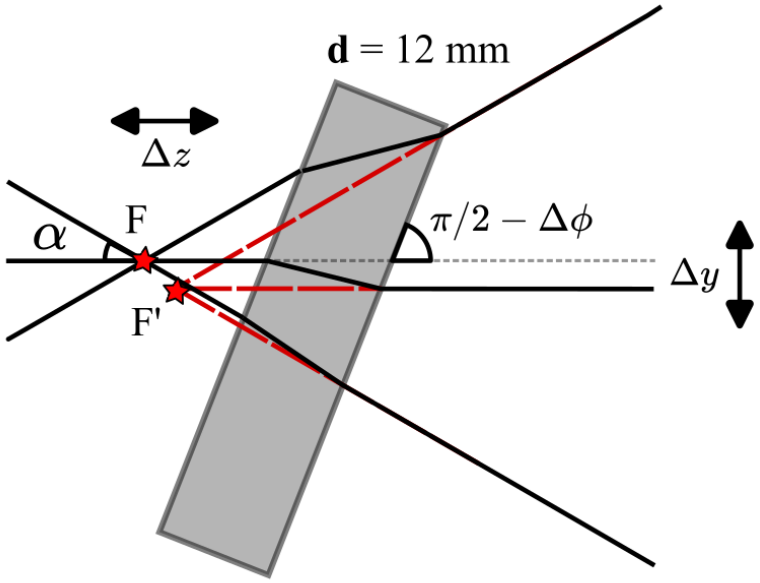

Figure 30: Geometric optic drawing of tilted glass window in the diverging beam path. Due to Snell's law, the change of index of refraction leads to a parallel displacement Δy of the incident beam as described by Equation 13. The focus F now appears to be shifted to F'. Since the amount of parallel displacement is a function of incidence angle α, F' is also moved along Δz, approximated by Equation 14.

This displacement in z needs to be accounted for and causes a readjustment of the z-translation stage's pick-up position. The Equations 13 and 14 are plotted in Figure 31.

To a good approximation, one can assume the lateral displacement to be linear in the limit of small angles giving 64 µm/deg (for a 12 mm window).

The maximal range of lateral displacement can be changed by choosing a thicker window. With a thickness of 12mm and a tilt range of ±40°, the ODT can be displaced by ±3 mm. When considering the width of the ODT to be ~30 µm, that corresponds to a displacement of 200 times its width.

This increase in the range comes at the cost of a deficit in precision. When the angular precision by which the window can be controlled is large, a smaller thickness can help increase the control.

The choice of thickness is also limiting the tilt angle itself. When the optics of finite thickness is tilted, the beam can clip at the edges. When large tilt angles and large thicknesses are required, larger optic diameters of 2 inch and above are needed.

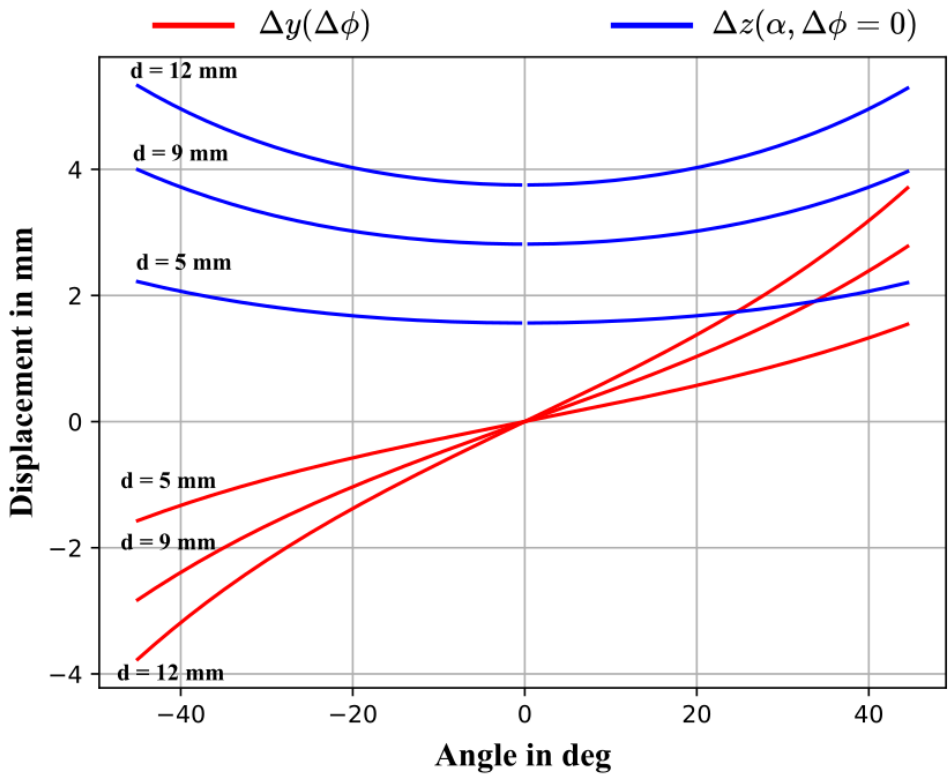

Figure 31: Calculated lateral displacement of the focus as a function of incidence angle on the tilted window. The lateral displacement Δy - in red - and the longitudinal shift Δz - in blue - are plotted as a parameter of window thickness d. Note that the longitudinal shift is a function of beam divergence angle α, assuming $\Delta\phi = 0$.

What is also evident from Figure 31, is that the thicker the window is, the more the focus will be displaced in z. But the aberrations, which can be understood as the curvature of the blue graph, increase with the window thickness.

8.4 DESIGN OF THE ODT DISPLACER

As the geometric optics picture explained above, the ODT position can be controlled by tilting a piece of flat glass at the conjugate plane of the trap. There are many ways a piece of glass can be rotated, but this thesis focuses on two motors, see Table 1.

	ELLIPTEC 18	NEWPORT PR50CC
Bidirectional repeatability	0.05°	0.075°
Max speed	420°/s	20°/s
Accuracy	0.4°	0.05°
Price	270$	2090$
Jerk control	No	Yes

Table 1: Comparison between the Elliptec 18 [83] and PR50cc [84].

When the proof of concept was tested, a window was mounted on the Elliptec rotation stage and put in a replica of the experimental optics setup. A photograph of the partial setup is shown in Figure 32 a). The focus at the image plane was then monitored with a CCD camera sensor.

On board the Elliptec motor, a piezo is driven at around 100 kHz. A periodic expansion of the piezo element brings a little aluminum piece to vibrate in resonance like a tuning fork. This vibrating tuning fork then pushes against a rubber ring and actuates the rotation. The result is a very fast motion of the rotation platform with high repeatability.

The test with the Elliptec motor soon revealed that although the final position of the window could be controlled repeatedly, the dynamics of the motion could not. Neither the velocity nor acceleration could be changed, not to mention programmed. Also, when moving higher loads, the motor would often overshoot the final position and jitter back to the desired angle in a stepwise manner. That is a substantial drawback for the cheap motor. Atoms would be lost during transport since the abrupt motion of the ODT would induce three-body loss and decrease the delivery efficiency.

To explore other options, the waveplate rotator servo-motor from Newport was tested as an alternative. Compared to the Elliptec stage, the Newport option is slower, with similar repeatability and better accuracy. Further, using an SMC100 motion controller, the peak velocity, acceleration, and jerk of the motion between two angles can be adjusted. This big advantage comes with an order-of-magnitude increase in cost.

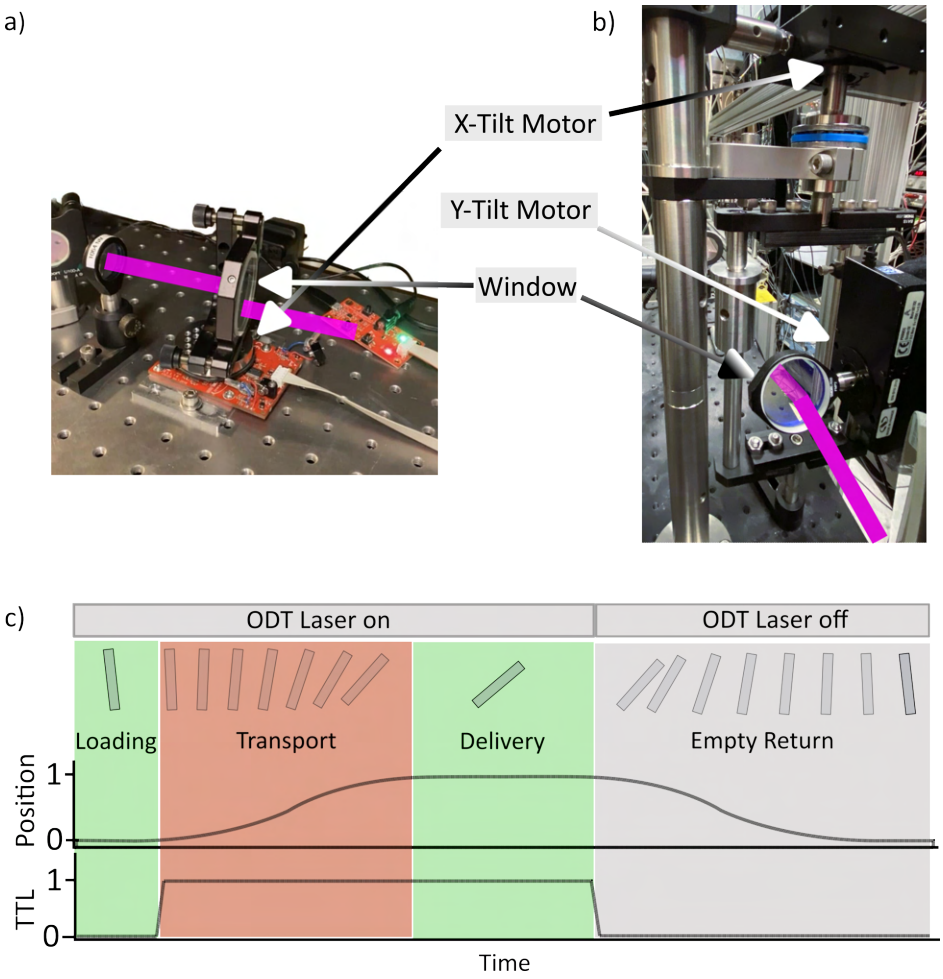

Figure 32: a) First proof of concept design. The 12mm AR coated window is mounted on a single axis, resonant-piezo rotation stage Elliptec 18 [83]. b) Final design of the two-axis gimbal in the experiment. Each x- and y-tilt motor is driven by the PR50CC [84] stepper motor from Newport. The y-tilt motor is mounted in a cage and rotated entirely with the motor by the x-tilt device. The window mounted in the center of each axis of rotation can tilt around two independent axes. c) Schematic representation of the rotation during the experimental sequence. The vertical axis represents the position of the x and y angle of the window. Position 0 is the angle required for the atoms to be loaded at the pick-up position in the main chamber. Position 1 is the angle necessary to drop the atoms off in the science chamber at the right location. During transport, the z-translation stage moves together with the window in a synchronized way. After the atoms are delivered to the science chamber, the ODT light is turned off, and the window and translation stage moves back to the initial position 0 for the next sequence. The TTL graph shows the rise and fall of the required trigger signal to execute this motion. The rising and lowering flank of the TTL stands the motion, respectively.

Since the z-transport of the ODT focus from one chamber to the other takes almost three seconds with the translation stage, the speed of the Newport motor with 20°/s is not creating a bottleneck in the experiment.

Also, if the initial and final positions were known and constant over time, a single axis of rotation along a specific unknown angle would be enough. This isn't easy to do. For two degrees of freedom, two pieces of glass could be rotated by two motors around two orthogonal axes. In our implementation, one piece of glass is rotated along two axes to save space along the beam path, as depicted in Figure 32 b). The gimbal mount houses two PR50cc motors and a single window in the center. The 2d rotation gimbal is homemade and consists of optics posts.

When the x-tilt motor is activated, an axis in a ballbearing shaft rotates a cage housing the y-tilt motor and the window. The y-tilt motor is then only directly connected to the window itself. It is a bit like nesting Matryoshka dolls.

During the sequence, the rotation of both x- and y-tilt motors are timed with the z translation stage as indicated in Figure 32 c). At position 0, the ODT is loaded in the main chamber. When the motion of the translation stage begins, the window starts to rotate to its final position 1. At the arrival, the atoms are caught by other dipole traps, and the transport ODT laser can be turned off. Then the motion is reversed, and the position is returned to its initial start.

The two SMC100 motion controllers from Newport communicate with the motors and can be addressed via RS232. A Rasberry Pi interface was created to sync the movement of the window with the translation stage's TTL trigger. It runs a script in the background to await TTL triggers, execute and send commands to the SMC100 and communicate with the Cicero software via RS232. The details of the control can be found in Appendix B.

8.5 STABILITY OF THE ODT'S POSITION

Many things, such as mechanical vibrations and temperature fluctuations, affect the stability of the experiment. The different materials expand with the change in temperature and cause the optics to misalign. Also, vibrations can introduce noise onto the mirrors, causing the beams to jitter. The difference is that temperature often causes long-term drifts, whereas mechanical instabilities can cause shot-to-shot drifts. To minimize instabilities in the experiments, all components and the environment should enable a repeatable and stable operation.

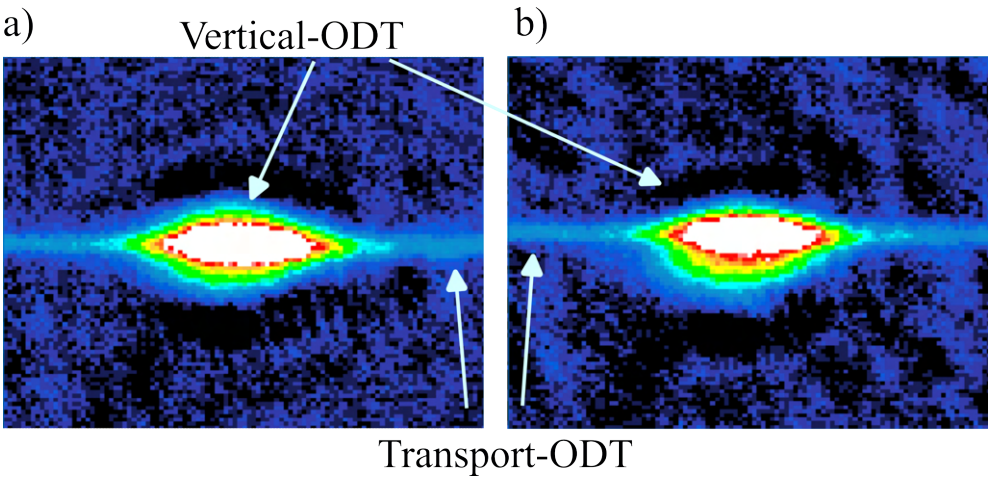

Figure 33: "In-trap" vertical (Top) absorption image of the transport ODT and the vertical-ODT after ramping down the transport ODT power. Pictures a) and b) show the resulting absorption image after running the same sequence. Comparing a) and b) reveals a shot-to-shot drift of the horizontal position of the transport ODT, leading to a shape and loading change into the vertical-ODT.

While optimizing the alignment of the transport ODT to its final position, the vertical-ODT, one could observe some shot-to-shot drift of the transport ODT position, resulting in a change in loading efficiency, depicted in Figure 33. Figure a) shows a centered blob of Rubidium and a residual line from the elongated transport ODT, and Figure b) shows the shifted transport ODT by a few pixels.

The stepper motors have a precision of 20 mdeg, leading to a minimal incremental shift of the Rubidium cloud by 1.29 µm in the x and y directions. Comparing these specs with a piezo-controlled precision mirror, we reach 2.5 µrad precision over a range of 8 mrad, versus ~0.1 µrad over a ~ 30 mrad range [85].

Newport guarantees a bi-directional repeatability of the PR50CC to be ±75 mdeg [84]. Therefore, the propagation of error in the position of the transport ODT for the science chamber would be ±5 µm. The imaging setup in the science chamber has a magnification of ~4.46, and the camera has a pixel size of 13x13 µm, giving us enough resolution to detect this drift.

The Plot in Figure 34 displays some testing data of the transport ODT stability. The Plot 34 a) shows the position of the atoms from shot-to-shot for more than 250 runs of the sequence over several hours.

The first feature of the data in Plot 34 a) is that some peaks/outliers occur randomly. These outliers always shoot up and indicate a cloud displacement in the same direction. They produce a five times larger deviation from the mean than the remaining points. One explanation for this behavior could be a slow RS232 write time, leading to an unfinished movement when the absorption image is taken. Otherwise, mechanical instabilities and hysteresis from the mount can also lead to this behavior. It is unclear why large fluctuations always tend to appear in a biased direction.

The second observation from Figure 34 a) is a linear drift in mean position over time. Again, this can be explained by temperature fluctuations in the lab. The solid red line in the plot indicates the linear mean, which shows a cumulative shift in the position of 2.5 px, which corresponds to 7.2 µm.

Finally, one can look a the histogram in Figure 34 b), displaying the frequency with which a certain displacement would occur around the mean drift. The gaussian curve around the center reveals a standard deviation around the linear drift of σ =1.9 µm. This is in agreement with the expected fluctuations coming from the motors itself [84]. The histogram also again shows the imbalanced distribution of large outliers.

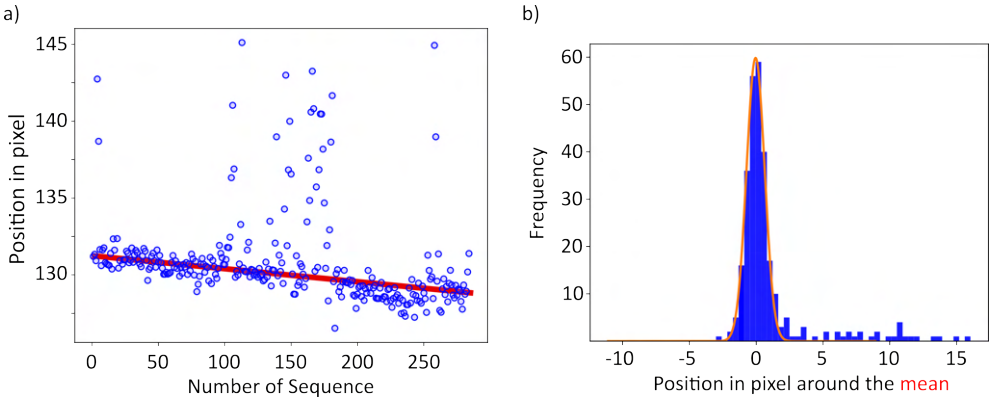

Figure 34: a) Position of the transport ODT waist in pixel after each run N. A linear fit highlights a systematic trend. b) Histogram of transport ODT position data. A Gaussian fit with a standard deviation of σ = 1.9 µm is added.

Since the position error depends on the tilt of the window, we get a different precision at the "pick-up" location in the main chamber compared to the "drop-off" in the science chamber. This is because the main chamber alignment was close to optimal; hence, the window is almost normal to the ODT beam at position 0. The smaller the angle of the window, the better the precision.

The difference in the window angle occurs when the transport ODT is displaced by tilting the window around 10deg, which is the necessary angle for the science chamber position. At zero angle (as is roughly the case for the main chamber), the typical repeatability would result in a displacement of ± 2 μm. Since the magnification for imaging in the main chamber is only ~2, and the imaging pixel size is the same, we could not see any drift from shot to shot.

Is this drift problematic for the repeatability of the experimental sequence? The required precision will depend on the size and shape of the crossed optical dipole trap catching the atoms. If the cross ODT is much larger than the shot-to-shot drift of the transport ODT, then the efficiency is much more forgiving. In Figure 33, the drift happens in the direction where the vertical-ODT is the most confining, and the trap is small. Hence the loading is affected. If we would load the atoms into the horizontal crossed ODT (light sheet), then the horizontal drift would be compensated by the large extent of the axial confinement of the trap. Both vertical- and x-ODT should be ramped up to "catch" the atoms optimally. Also, by introducing a dimple beam, the atom number would equalize more and not suffer as much from drop-off instabilities.

8.6 SEQUENCE OPTIMIZATION

The beam displacer introduces two more degrees of freedom to the experiment, which can be dynamically changed within the sequence. With the translation stage, one can move the atoms on an arbitrarily curved trajectory through the chamber, just like a curved baseball.

After installing the window into the ODT optics, the focus was misaligned from the previous optimum pickup position. That meant the atom number in the ODT after loading was vanishingly small. Aligning the ODT can be very delicate, and signal loss is better avoided.

By scanning the x and y angles of the tiltable window, one could restore the atom number within several minutes. Figure 35 shows the subsequent scan of the x and y tilt of the window in degree and how the atom number in the ODT changes with position. The best angle is found when the atom

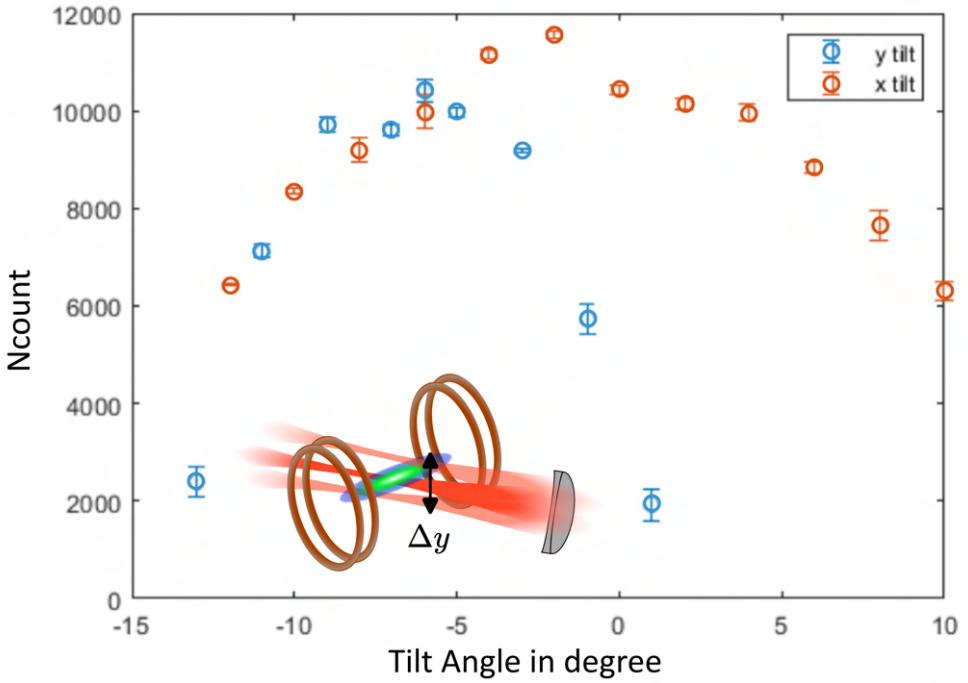

Figure 35: Alignment optimization. Plotted is the number of atoms in the ODT (up to an undetermined multiplicative constant) as a function of the relative tilt angle of the flat window. The tilt is incrementally changed by a few degrees at a time, shifting the focus of the ODT by tens of µm according to Figure 31 and Equation 13. The insert in the Figure displays the cloud in the magnetic trap, while the position of the ODT is scanned for each sequence. The x- and y-tilt is changed independently. The atom number was measured by TOF absorption imaging. Both x and y data show a single maximum at a specific relative angle, indicating optimal loading.

number is the largest. We used this procedure to find the optimum position for the old experimental sequence.

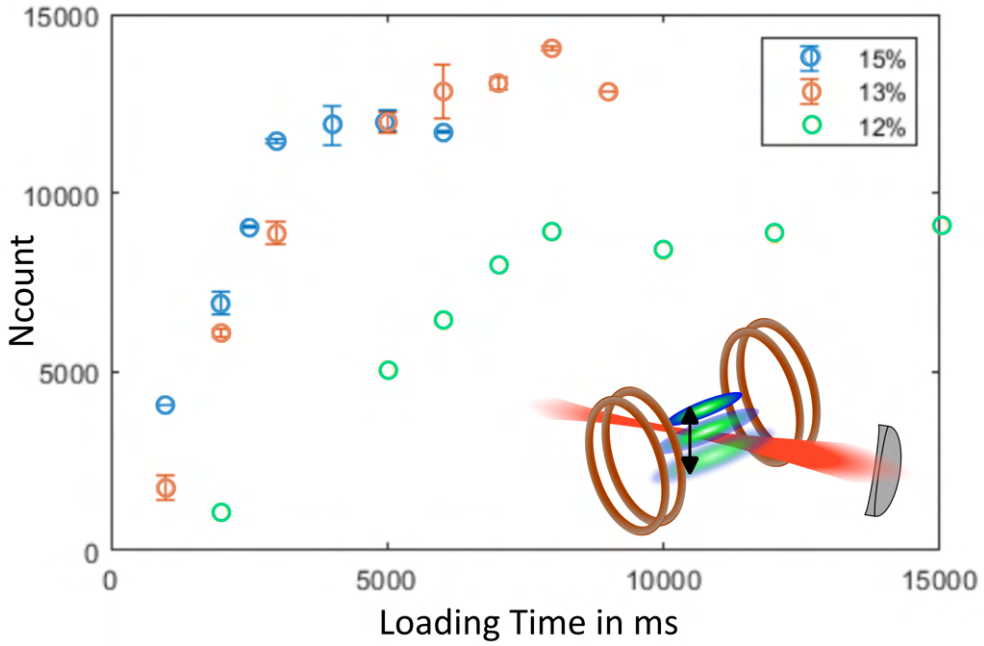

Figure 36: Atom number in the ODT as a function of time displayed for different magnetic trap relaxations. The magnetic trap is relaxed to x% of its original depth, and the position of the ODT is then adjusted to compensate for the lack of gravitational sag. The insert in the Plot shows how the cloud in the magnetic trap is rising and tightening with the increased field, as the ODT tries to load.

A nice thing to be noticed is that the atom number distribution in the ODT is broader for scans in the x- direction and sharper in the y-direction. Since the magnetic trap is cigar-shaped, with its elongated axis orthogonal to the ODT propagation, we see a sharper loading curve by changing the height of the ODT and scanning the radial confinement.

Another feature of the beam displacer is its use as magnification calibration. Knowing the analytic solution for the expected displacement when the window is tilted can calibrate the imaging system's magnification.

After the alignment was restored, the gravitational sag problem could be addressed. Recapitulating, the sequence time and maybe efficiency is suffering because the ODT is loading in a shallow expanded cloud. Before optimizing, a single sequence was 42 seconds long, with a ~ 6 second ODT loading time. The hypothesis was that by not relaxing the trap too much, the trap frequency stays higher, and the atoms "slosh" faster into the ODT, loading more quickly.

That means increasing the trap confinement in the sequence bit by bit and then optimizing the vertical ODT position to compensate for gravitational sag, like in Figure 35. Then we measured a loading curve for several values of magnetic confinement to verify the improvement.

Figure 36 shows the progress of the multi-dimensional optimization. Previously, relaxing the trap to 13% of its original confinement and holding it there for 6.2 seconds was the standard. This loading curve is shown in red. The plot shows that the change in confinement can improve loading by positioning the ODT to a tighter magnetic trap (15%) and worsen it by loosening even more (12%). The quantity important for the assessment is the loading rate (~ slope at the beginning of the curve) and the plateau value after a long time.

Ultimately, all the 6 seconds previously needed to hold the ODT in the relaxed trap and wait by just loading could be reduced. The loading time is now limited by the time the magnetic trap is ramped down within 500 ms[2].

2 This is a significant increase in the quality of a Ph.D. life.

9

MAKING BEC

You miserable piece of rust!
I am man! You are machine!
Do as I command or I will pull your plug!

— Gyro Gearloose

Although making BEC is not a scientific achievement anymore, it is still a challenging and fascinating phenomenon: The transition from a thermal cloud to a coherent macroscopic population of the quantum mechanical ground state.

A high phase space density on the order of unity is required to cross the phase transition to BEC. This is the limit at which the thermal de Broglie wavelength becomes comparable to the interparticle separation in the trap. A sequence of laser and evaporative cooling steps is needed in BEC4 to reach the high phase space density [6].

The motional ground state of the BEC is used to load atoms in the ground state of an optical lattice. This ground state in the optical lattice can be the starting point for quantum simulations in the Bose-Hubbard regime.

The following section will describe the steps and details to reach BEC again in the new science chamber. For this, we did not install the objective yet since it would strongly limit the field of view.

9.1 BEAM LAYOUT

There are several ways in which a cross ODT could be formed. Since we initially planned to use the transport ODT for the evaporation, either an additional vertical ODT or an orthogonal horizontal ODT beam would generate the cross.

Figure 37 shows the layout of the laser beams used in the science chamber. A transport beam brings the atoms to the center of the octagon, which is crossed with a horizontal light sheet. Those two beams are used to make BEC by forced evaporation [23]. Two horizontal and vertical 1064 nm beams generate a lattice. One horizontal axis can also generate a spin-dependent lattice using an 810 nm laser [40]. The molasses beams provide the light to generate the detectable fluorescence while cooling the atoms.

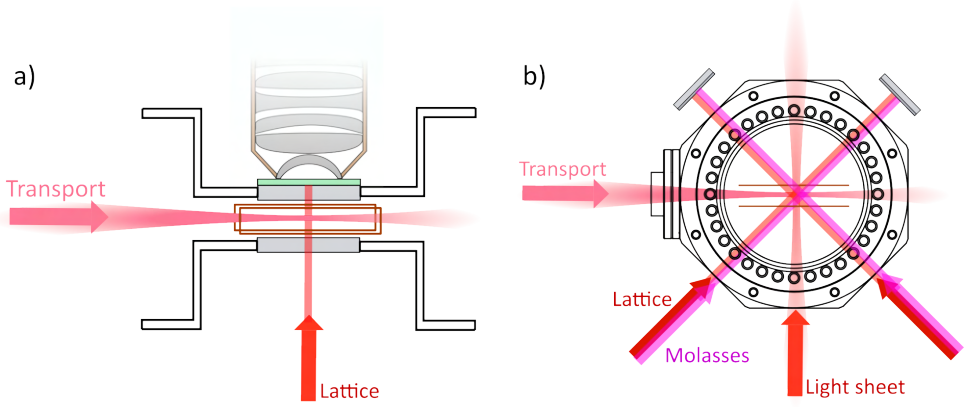

Figure 37: Optics layout for the science chamber. a) Side view: The transport beam (1064 nm) brings the atoms from the main chamber under the objective. Around the atoms in the center of the chamber are RF coils for driving hyperfine transitions. The vertical lattice beam (1064 nm) is sent into the chamber from the bottom viewport and is retro-reflected from the HR coated 1mm correction plate between the objective and viewport. b) Top view: The transport ODT is overlapped with a horizontal light sheet (1064 nm) for evaporation. The two horizontal lattices (1064 nm, 1064 nm+810 nm) are launched and retroreflected through the diagonal side viewports. Also, the molasses beams (780 nm) are sent collinearly with the lattice beams.

Initially, the HR coated 1mm correction plate on the top imaging viewport was not inserted. This prevented the formation of a strong vertical lattice, and the vertical beam is shown in Figure 37 a) was used as a regular dipole trap. A strong optical lattice would reduce the evaporation efficiency and make BEC more tricky.

9.2 ALIGNING THE TRANSPORT-ODT TO A CROSSED ODT

The transport ODT with a waist of ~ 30 μm was first aligned to a horizontal light sheet with $1/e^2$ beam waist 187 μm in the horizontal plane and 17 μm vertically. The general problem is that a single dipole trap has a weak confining axis along its propagation axis. Therefore, another dipole trap can improve the confinement along the loose axis. On the other hand, there is always the need to compensate for gravity, thereby relying on tight vertical confinement with a horizontal beam.

In the end, the atoms should be aligned to the microscope. But due to the small field of view of the objective, it is very inconvenient to align by imaging through it. Therefore two guiding beams are pre-aligned to the center of the science chamber using masks on the viewports. Then the cross dipole beams

(light sheet and vertical ODT) were aligned to those guiding beams, hoping that only fine-tuning is needed when the objective is on.

The next challenge is to bring the atoms to the point in the science chamber where the two foci hopefully meet. We then set up absorption imaging from the top viewport to align the atoms in the transport ODT with the light sheet. We scanned the position of the ODT by utilizing the new beam displacer until we could see a distortion of the ODT trap. Since the transport ODT has three degrees of freedom, which can be scanned, this task was relatively quick (a few minutes). This distortion is shown in Figure 38. The light sheet confines the atoms more to the center, forming an anisotropic cross.

Then, the optimum position is found by maximizing the transfer of atom number from one trap to the other after a particular hold time.

The vertical dipole beam was introduced and similarly aligned to the cross to get tighter confinement in the horizontal plane. We later realized by Kapitza-Dirac analysis [86] that the vertical dipole trap formed a weak lattice with the top imaging viewport. And with the plan of a 1 mm HR plate, forming a deep lattice would be unavoidable and hinder evaporation. Therefore we abandoned the vertical dipole for evaporation.

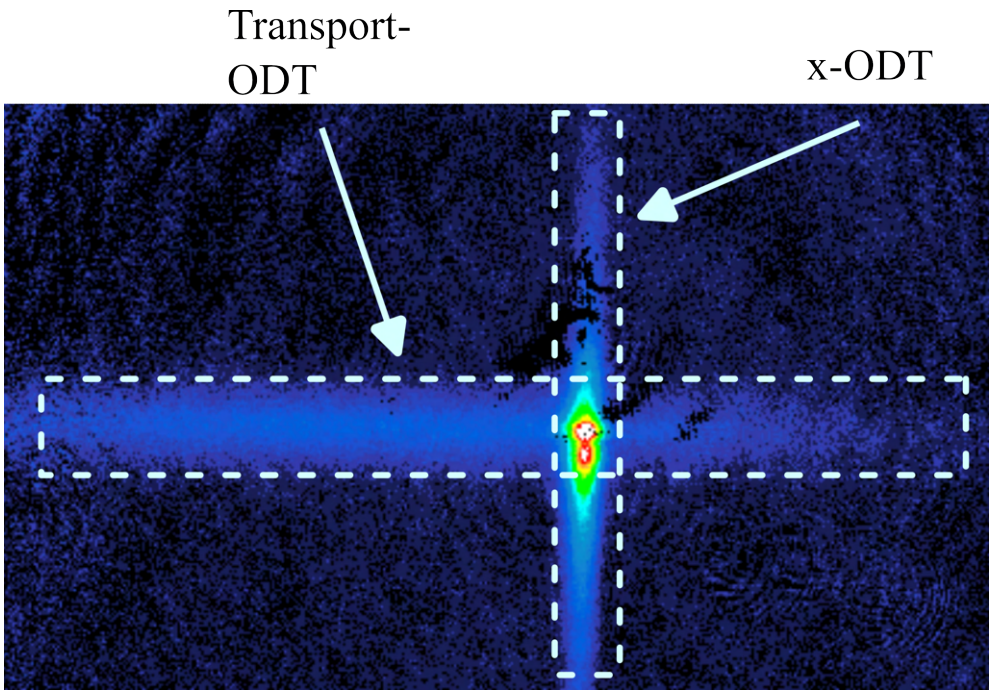

Figure 38: Vertical (Top) absorption imaging of the transport-ODT and the x-ODT after a short time-of-flight (TOF) in the science chamber. The x-ODT power is ramped up after the transport-ODT reaches its final position. After a certain amount of "hold" time for loading, the imaging sequence begins.

We later introduced an additional ODT beam, counter-propagating to the transport ODT (anti-ODT) to get more stable evaporation. The reason is that the transport ODT beam is somewhat limited in its geometry and can't be optimized for optimal trap shape. The transport ODT, therefore, delivered the atoms to three local ODT traps optimized for evaporation.

9.3 EVAPORATIVE COOLING IN CROSS-ODT

Although the atoms were precooled by evaporation in the main chamber magnetic trap, further evaporation is required in the science chamber.

To reach higher phase space density, a non-adiabatic cooling mechanism is needed, where atoms carry away energy by escaping the trap after elastic collisions, leaving behind only the cooler atoms. So to get efficient evaporation, one needs a high atom density to get a high collision rate, and the ratio between inelastic and elastic collisions should be favorable. In addition, evaporation requires a mechanism to selectively remove hot atoms and guarantee re-thermalization of the remaining atoms.

As described in the introduction, a common way to evaporate is by initializing atoms in a low field seeking hyperfine states, and trapping them in a local minimum of a magnetic trap [6]. Then an RF field is applied to the trap, flipping the internal states of the atoms to an anti-trapped state. The resonance condition is a function of their position in the trap, i.e., it depends on the magnetic field. The more energetic atoms can move higher up in the trapping potential; hence, the Zeeman levels are shifted more. If the frequency of the RF field is tuned to that Zeeman splitting, the atoms are in resonance and undergo a spin flip. Carefully sweeping the frequency enables one first to evaporate hot atoms and then remove cooler and cooler atoms.

To evaporate in a cross-dipole trap, the intensity of the light is ramped down, lowering the trap depth. The energetic atoms are released from the trap, while the elastic thermalization keeps the cold atoms. The direct evaporative cooling to BEC in a cross dipole trap was first demonstrated by Adams et al. [87]. In contrast to evaporation in the magnetic trap, the confinement of the trap also changes during evaporation, as can be seen in Equation 11. Because of the reduction of confinement during evaporation, the rate of elastic collisions is reduced [23]. This problem can be addressed using forced evaporation by introducing another highly focussed "dimple" beam that changes the trap shape together with a magnetic gradient [88]. The mechanism of introducing a far narrower trap while relaxing the harmonic confinement of

the former is also described in Reference [89], where a narrow ODT beam is introduced in a large magnetic trap.

Also, in the previous setup, dimple evaporation was implemented because it resulted in a stable and repeatable atom number in the BEC. To make fast progress, the decision was made to generate BEC only in a cross-ODT, without magnetic gradient or dimple.

The optimization of the ramp-down parameters was inspired by the values in the previous experiments. Being rather confident at that point, the only question remaining was finding out when we would cross the BEC transition.

9.4 TEMPERATURE MEASUREMENTS

To determine the temperature change of the gas after evaporation, one can analyze the time of flight (TOF) data from the cloud. The trapping potential is suddenly relaxed, and the cloud expands, as shown in Figure 39 b) and c). Due to expansion, the initial momentum distribution is then mapped onto the density spread of the could. This density is then measured for different delay times between absorption imaging and releasing the atoms from the trap [6].

There are also less destructive ways of determining the temperature of trapped gas in situ. Still, the imaging system's resolution limits this approach, as does a lack of precise knowledge of the actual trapping parameters [23].

For an anisotropic harmonic potential $U(\mathbf{r}) = 1/2\, m(\omega_x^2 x^2 + \omega_y^2 y^2 + \omega_z^2 z^2)$, One can find the density of atoms in the trap in a semi-classical limit being:

$$n(\mathbf{r})_0 = \frac{1}{\lambda_{dB}^3} g_{3/2}\left(e^{(\mu - U(\mathbf{r})/k_B T)}\right). \tag{15}$$

Where $\lambda_{dB} = \left(2\pi\hbar^2/mk_B T\right)^{1/2}$ is the de Broglie wavelength, μ is the chemical potential, which is set by the number of atoms in the trap, and $g_j(z) = \sum_i z^i/i^j$ is the polylogarithm. After free expansion for a time t, the atomic density distribution is given by [6]

$$n(\mathbf{r}, t) = \frac{1}{\lambda_{dB}^3} \prod_{i=1}^{3} \left(\frac{1}{1+\omega_i^2 t^2}\right) g_{3/2}\left(\exp\left[\mu - \frac{m}{2}\sum_{i=1}^{3} x_i^2 \left(\frac{\omega_i^2}{1+\omega_i^2 t^2}\right)\right]\right). \tag{16}$$

Now the spread of the cloud evolves as $\sim e^{-x_i^2/2\sigma(t)^2}$ for times $t \gg 1/\omega_i$. We can find a fit for the curve emerging from plotting standard deviation $\sigma(t)$

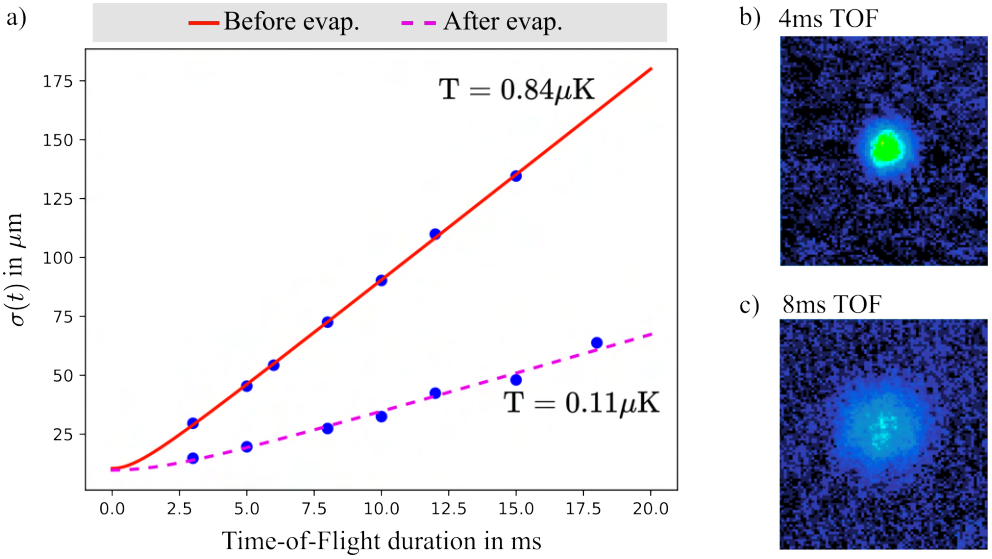

Figure 39: Time-of-flight (TOF) temperature analysis before and after evaporation in an optical cross dipole trap. a) Plotted is the square root of the variance of the atomic density distribution after a certain TOF duration. The solid red line displays the TOF-spread fit of Equation 17 for the cloud before evaporation in the cross ODT. The pink dashed line shows the same function fitted to the data after evaporation in the cross ODT. The temperature for the cloud before (after) evaporation is 0.84 μK (0.11 μK). b) 4 ms TOF absorption image of the cloud after evaporation. c) 8 ms TOF absorption image of the cloud after evaporation.

for multiple TOF parameters, giving the temperature T as a fitting parameter [6, 23, 44]

$$k_B T = \frac{1}{2} m \left(\frac{\omega_i^2}{1 + \omega_i^2 t^2} 2\sigma_{i,th,0}^2 \right). \tag{17}$$

Fitting this equation to the TOF data will also give information about the trapping frequency ω_i. However, since a direct comparison with the trap frequency from Equation 11 is difficult, one should use different techniques to get a more precise result of trapping frequency.

9.5 OPTIMIZING TO BEC

Looking at our TOF data in Figure 39, the phase transition to BEC was not crossed yet. The smoking gun of anisotropic expansion of the cloud in the mean field limit and any form of bi-modal density distribution was not observed yet. Although we did not yet introduce a tightly focussed dimple beam, we hoped to get a "pre-dimple" BEC.

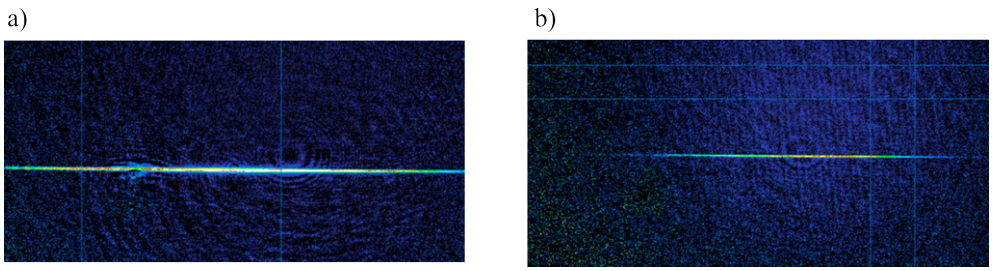

Figure 40: In trap absorption image of transport-ODT a) after, and b) before, optimizing the atom number in the main chamber by a factor of 1.7. The magnification and image frame in both pictures is the same.

Our first hypothesis for not reaching BEC was that the atom number in the trap was too low. This would result in a lower collision rate and slow thermalization during evaporation. So the MOT alignment in the main chamber was optimized and increased the atom number in the magnetic trap after evaporation by a factor of ~ 1.7.

This improvement in atom number is also clearly visible in Figure 40 between two in-trap transport-ODT images before and after optimization.

We also did not apply any form of magnetic field gradient to the atoms during evaporation, as in the previous setup. The gradient would help to blow out atoms from the extended wings of the cross-ODT, thereby suppressing the scattering with the central bulk.

The other concern was that the vertical ODT in the main chamber, forming one of the cross-ODT arms, was not tight enough. So the optics for the launching path of the vertical ODT beam was adapted to get a new beam waist $w_0 \approx 65$ µm instead of the old parameter of ≈ 110 µm.

Also, the parameters of the horizontal x-ODT were changed back and forth between a tighter light sheet and a rounder aspect ratio, hoping it would compensate for gravity more, even after evaporation.

Lastly, we needed to determine if the sequence's ramping parameters were still optimal. Since the aspect ratios and power in the optical traps changed, we had to adapt the trap power's final value, the time for evaporation, and the ramp's curve.

After working on some of our concerns mentioned, we finally got BEC! Figure 41 b) shows the density of the cloud after TOF. Visible is the bimodal shape of the cloud due to the mixture of the trap potential in the Thomas-Fermi approximation and a thermal wing. The fit gives a condensate fraction of 0.32. By evaporating even more, we could get a condensate fraction of 0.7 (not shown in the Figure). Which is the previous "pre-dimple" condensate fraction. This is a recent result, so little testing was done, but many things must be checked before moving on.

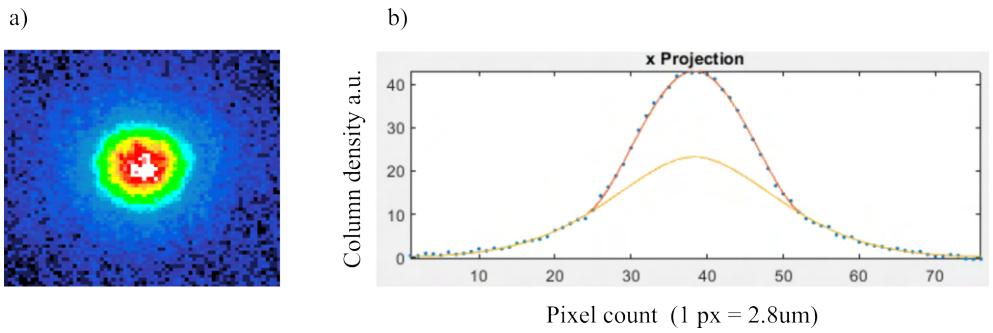

Figure 41: a) 8 ms TOF image after evaporation in cross ODT. b) Column density cross-section of Image a), showing a bimodal density distribution between a thermal Gaussian wing and a Thomas-Fermi inverted potential.

Making BEC is crucial for moving on to the next steps of the experiment. We successfully used the transverse beam displacer to align the atoms to the cross-dipole trap, where further evaporation was performed. Finally, the chapter showed evidence of the formation of BEC by TOF density distribution measurements.

10

SUMMARY AND OUTLOOK

This thesis presented the construction of an ultra-high vacuum system suitable for detecting single site-resolved fluorescence of Rubidium atoms in an optical lattice. The upgrade was done on a two-chamber experiment, with one chamber remaining untouched. The new system features a reentrant viewport capable of housing a high NA (0.8) objective for imaging 780 nm fluorescence. A failure of the imaging viewport's crucial HR coating compelled installing a spare reentrant viewport with a correction plate on top.

The installation of an in-vacuum RF antenna and multiple magnetic fields coils around the chamber was shown. The vertical gradient coils can produce a gradient of ~50 G/cm @ 100 A, and the side coils a bias of ~0.8 G/A.

Furthermore, an extension and improvement to the experimental control interface were made by upgrading and expanding the available analog and digital control channels and their ground loop-breaking devices. A server rack was set up to house three new NI cards with 16 analog and 32 digital channels. An onboard low-pass filter is tailored to suppress frequency components, which possibly cause lattice excitations. The improved stability of analog signals is expected to transfer onto the general stability of the experiment.

A transverse steering mechanism for the transport optical dipole trap was demonstrated. In addition to the existing 360 mm of axial travel between the chambers, it enables a 2D lateral range during transport of up to 6 mm with a minimal incremental motion of 1.3 μm. However, the limiting repeatability of the device, together with thermal and other unknown instabilities, cause the ODT to deviate around the mean drift with a standard deviation of 1.9 μm. Nevertheless, the flexibility of reversible ODT steering has shown to be beneficial for aligning the atoms to the fixed microscope objective. In addition, it improved the loading of the atoms from the main chamber's magnetic trap without limiting the delivery position in the science chamber.

The last part of the thesis presents the progress toward making BEC in the new science chamber. The evaporation was performed in a horizontal crossed dipole trap of 1064 nm laser beams. The forced evaporation was performed by ramp down of intensity. The constraining parameters of the transport ODT motivated the setup of a counter-propagating ODT with a horizontal beam. A Kapitza-Dirac analysis revealed the formation of a weak

vertical lattice from unwanted reflections off AR coatings, preventing the use of vertical dipoles.

In the future, a magnetic gradient during evaporation to introduce a tilt in the potential would expedite the evaporation. We also thought about reinstalling a tightly focused dimple beam at 840 nm wavelength for further evaporation, increasing the condensate fraction, and stabilizing the final atom number. But since this beam would launch through the objective, we were hesitant to mount it at this stage because of its restricting field of view.

The next steps towards seeing single-atom fluorescence in the lattice are to finalize the alignment of the lattice and molasses optics and implement the layer selection. The retro mirror of the molasses will be jittered to prevent interference of the molasses beams and hence uneven illumination of the lattice.

Creating a pinning lattice for the atoms requires a significant amount of power. The light is currently being delivered through regular fibers, which limits the total power. In addition, the fiber amplifiers are degrading in performance. One solution could be to bring the laser closer to the machine table and bypass the use of optical fibers. Another option could be to use photonic crystal fibers to improve power delivery from the laser to the machine table.

As became apparent during the upgrade and with discussions with Peter Schauss from the University of Virginia and the groups at MPQ in Munich, layer selection below the objective is difficult and requires good stability. For example, the magnetic gradient selection planned in BEC_4 requires good magnetic field stability to address only a single layer of atoms in a vertical lattice. In contrast to the Munich experiment, we plan to implement two instead of one gradient coil, creating a larger magnetic gradient at a lower bias, which hopefully makes the stability requirement less stringent. Other methods, such as using a light sheet or accordion lattice, have also been considered but are not the primary option. This is because a light sheet has a strong anisotropy, and the accordion lattice could move independently of the objective plane.

When the fluorescence and lattices are aligned, the performance of the objective will be determined in the setup. The PSF can be analyzed by loading a sparse lattice, revealing possible aberrations. The plan to rest the objective onto the viewport has often caused surprise when presenting to peers. The future will show if the stability and lack of adjustment limit the imaging quality.

Afterward, the experiment will continue to pursue the physics of spin-one quantum magnetism in 1D chains. The ability to individually address

and detect atoms in the lattice will dramatically improve the observation of correlations and the preparation of chains with constant and equal lengths. The cumulative improvements are also expected to help maintain adiabaticity during critical sweeps in the experimental parameters and observe XY-ferromagnetic correlations.

Part IV

APPENDIX

A

PCB DESIGN

A.1 ANALOG GLB CARD

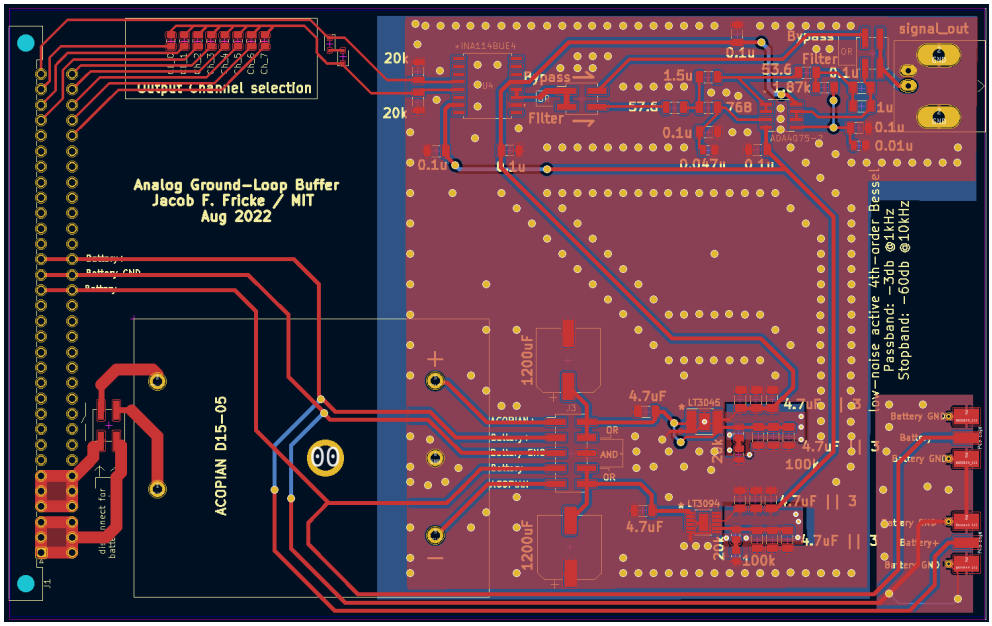

Figure 42: PCB design of the analog GLB card.

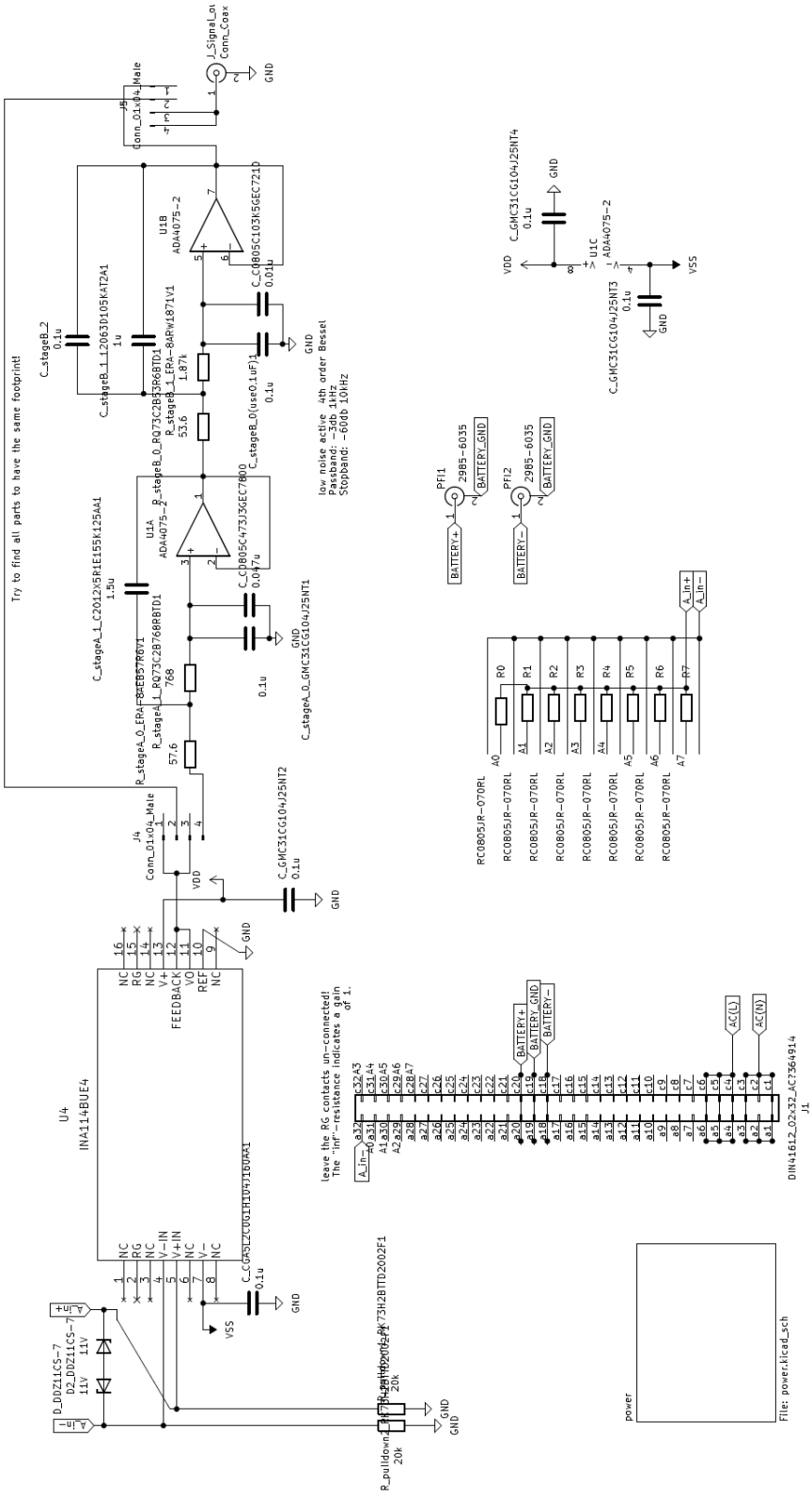

Figure 43: Circuitry schematic of the analog GLB card - Part 1. The schematic shows the backplane connection, and signal routing through the instrumentation amplifier and the active filter stage.

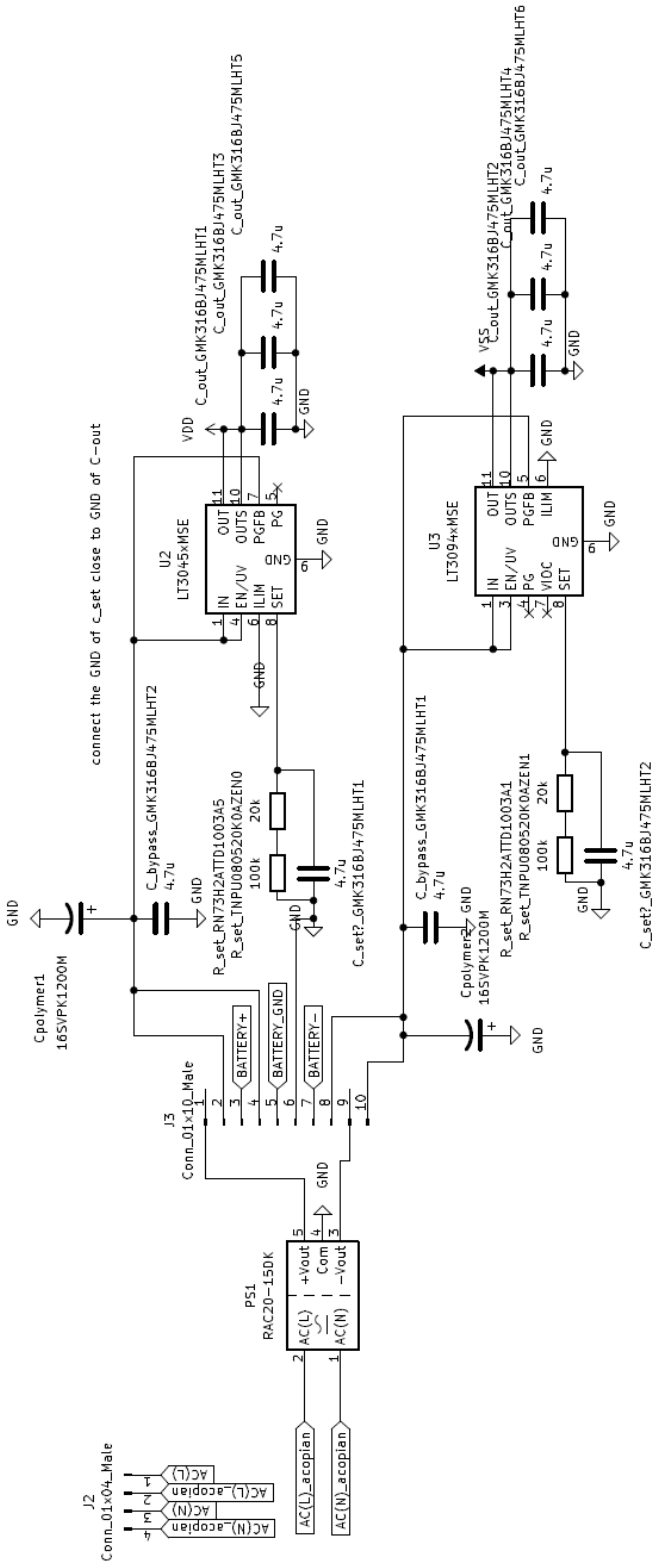

Figure 44: Circuitry schematic of the analog GLB card - Part 2. The schematic displays the details of the power delivery for the analog GLB card.

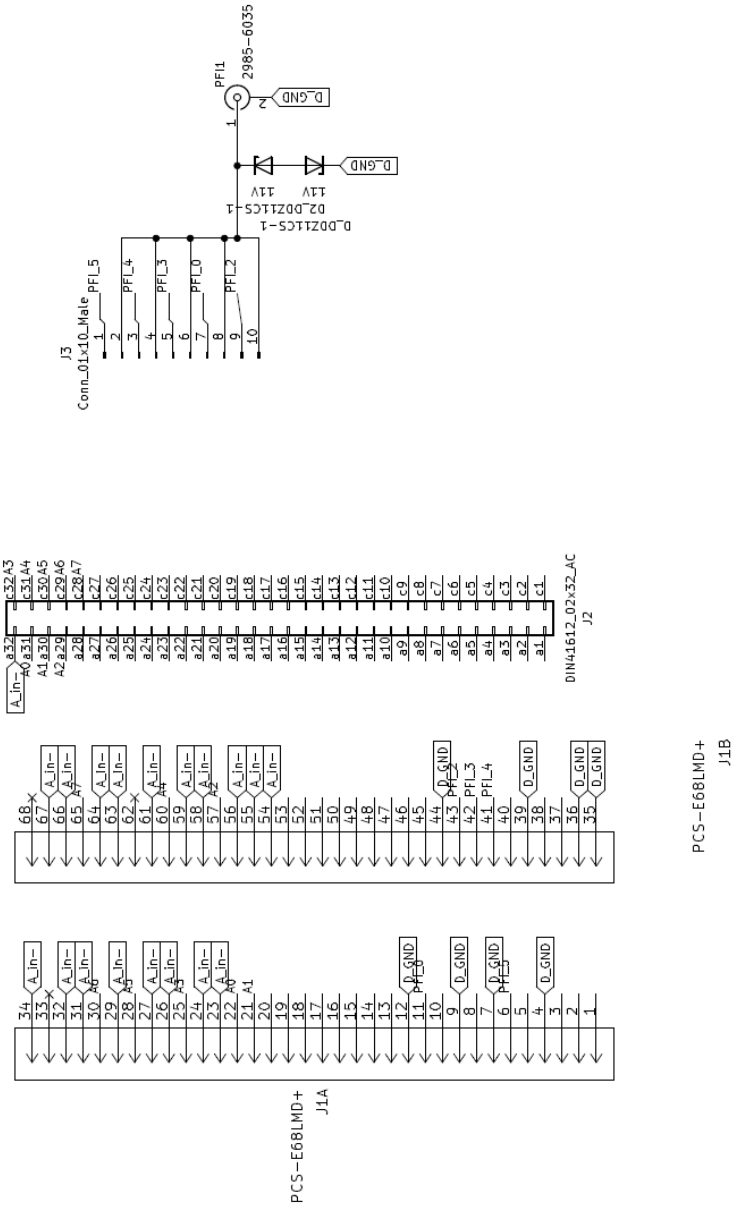

Figure 45: Schematic of the analog breakout card.

A.2 DIGITAL GLB CARD

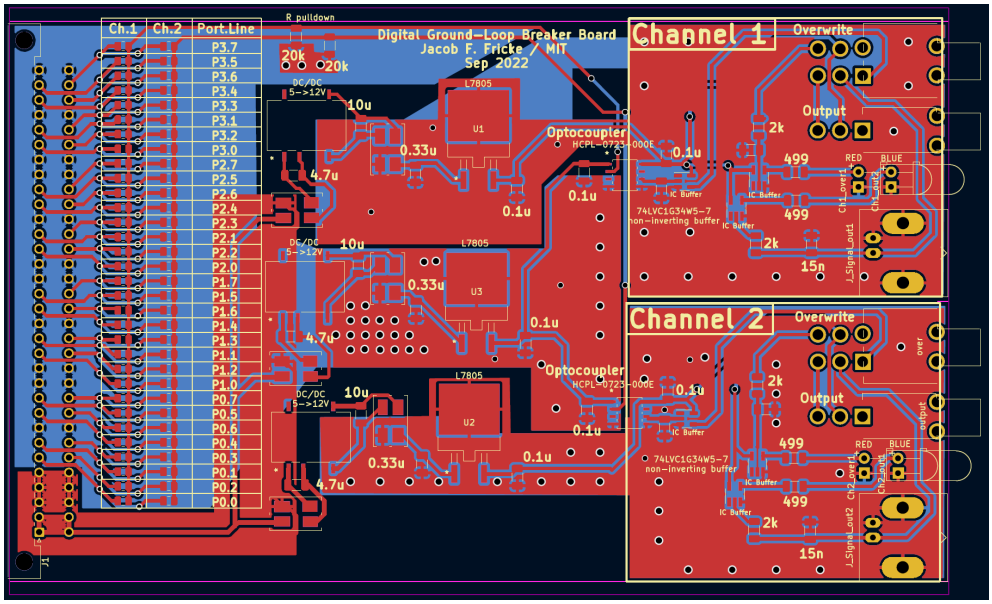

Figure 46: PCB design of the digital GLB card.

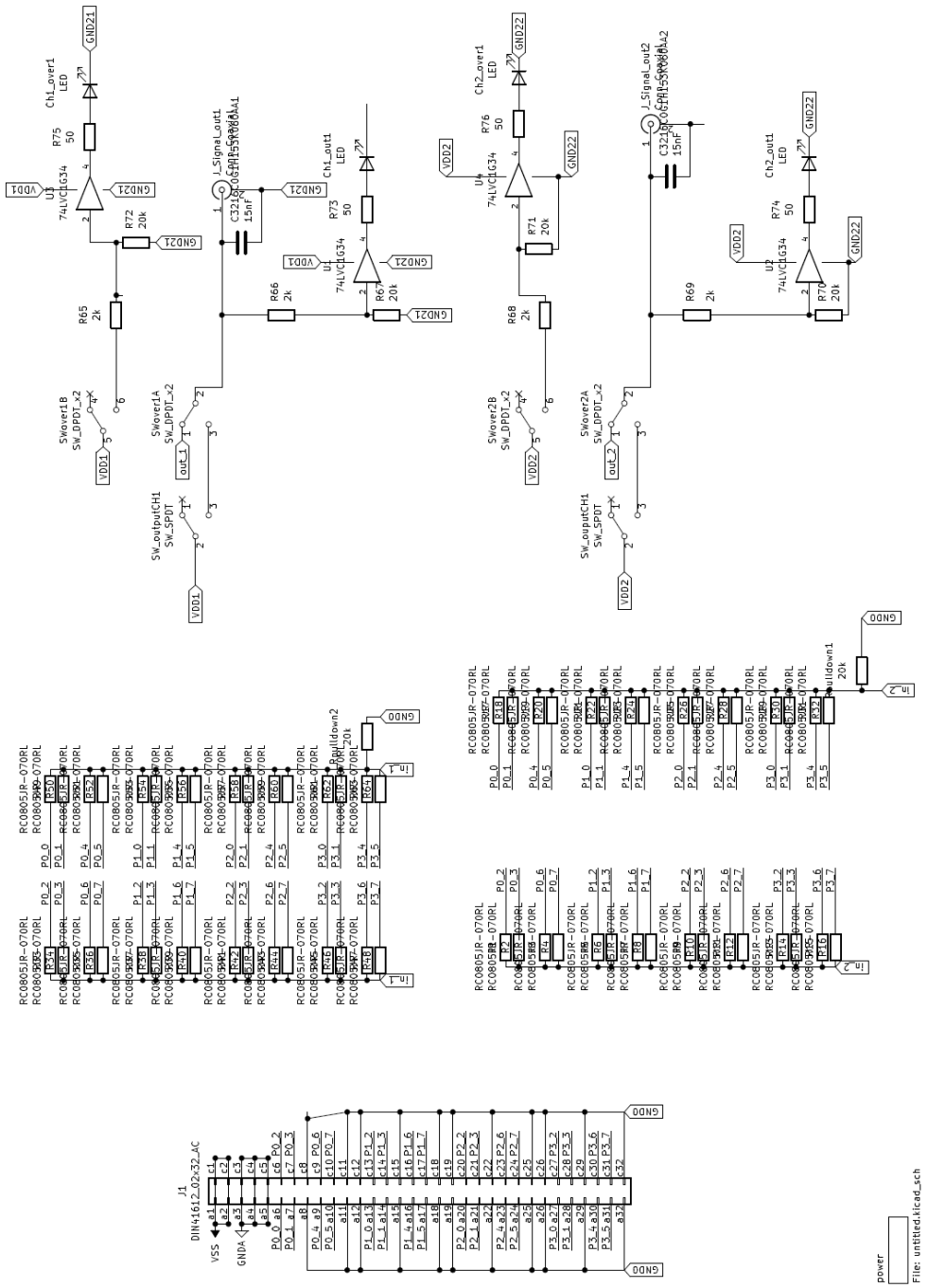

Figure 47: Circuitry schematic of the digital GLB card - Part 1. The schematic shows the backplane connections and the LED and toggle override mechanism.

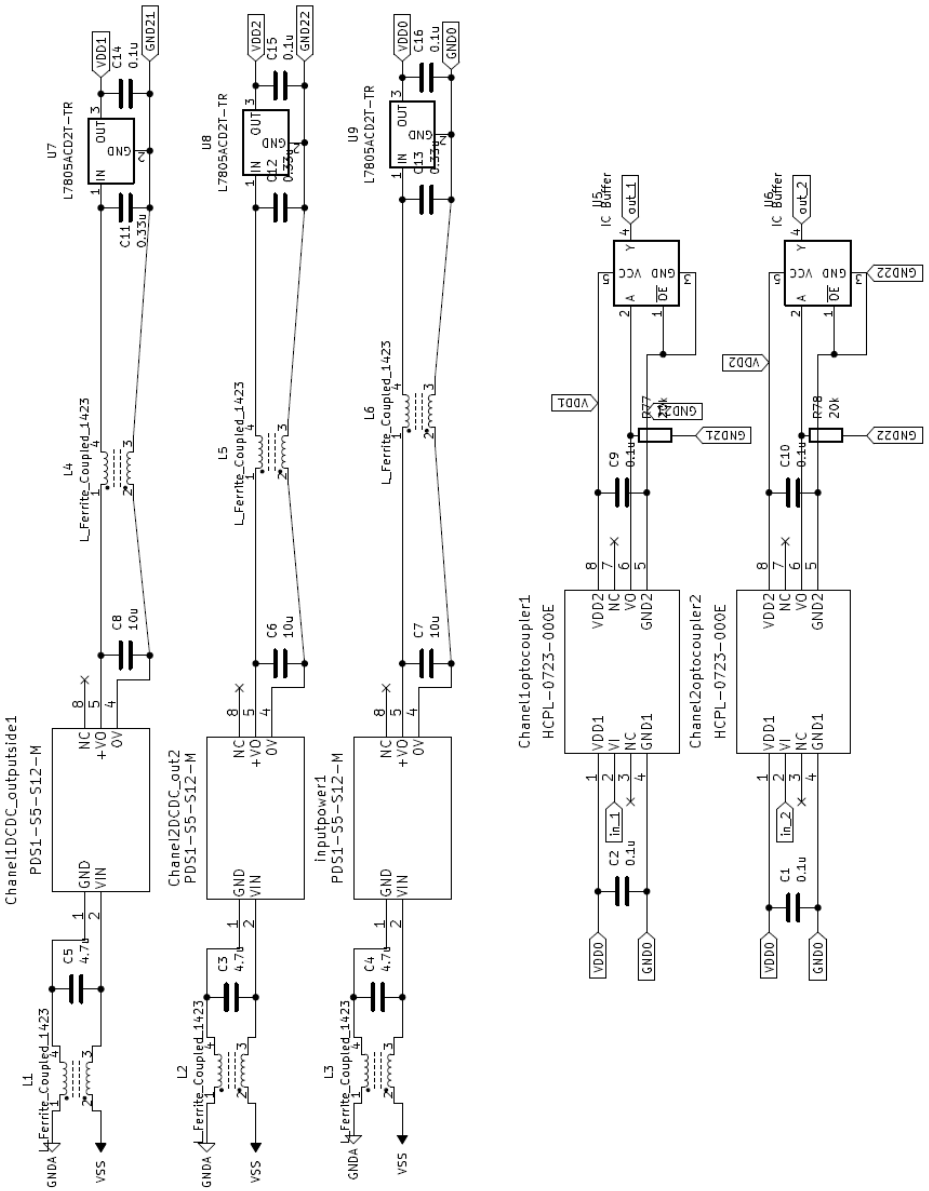

Figure 48: Circuitry schematic of the digital GLB card - Part 2. The schematic shows the details of the isolated power distribution on the left and the optocoupler mechanism on the right.

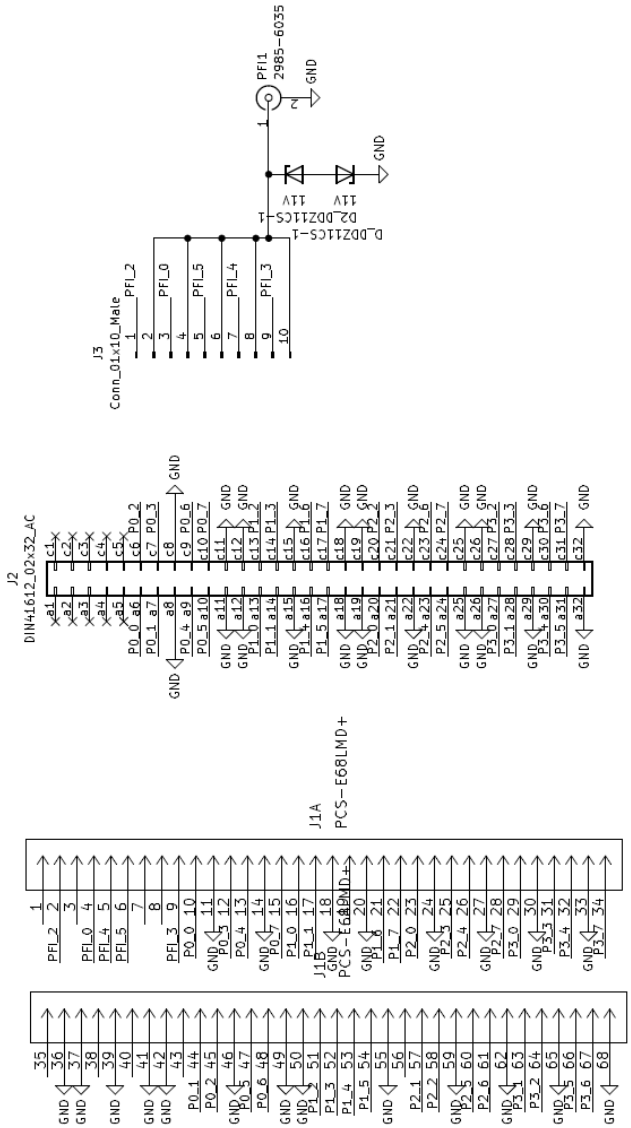

Figure 49: Schematic of the analog breakout card.

A.3 BREAKOUT CARDS

The breakout cards provide the new interface between the NI cable from the NI card[1] to the backplane. Furthermore, they serve as a port for the Programmable Function Interface (PFI) pins, which can be used for the external clock signal. In Figure 50, the basic principle for the breakout cars is presented on the example of the digital PCI-DIO-32HS card. The Breakout for the analog system operates in the same way. The Pinout for the NI card is depicted on the right side of the drawing. The pinout for the digital card can be found in reference [91], and for the two analog cards in references [53] and [54].

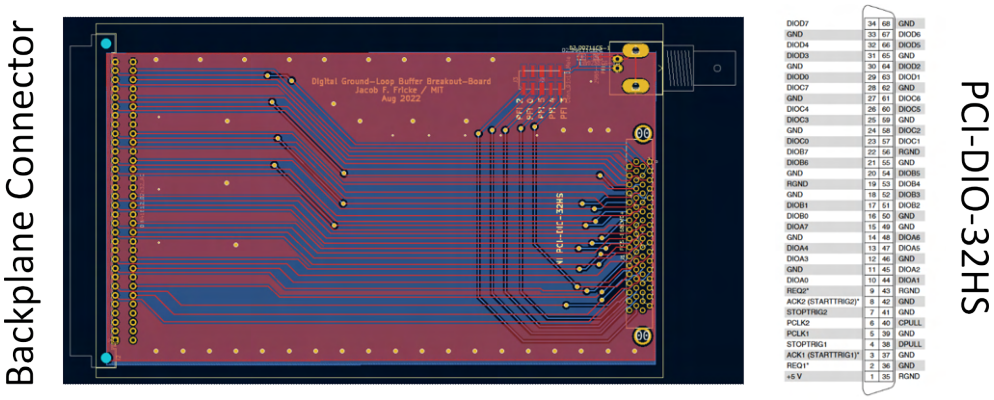

Figure 50: PCB design for the digital GLB breakout card. The NI cable from the PCI-DIO-32HS card, with the corresponding pinout shown on the right, is connectable with the corresponding slot on the card. The BNC interface on the top right of the PCB can be used to address the card's PFI. The main body of the PCB is passive and only reroutes the connections to the backplane via the DIN41612_02x32_AC connection. The schematic for the pinout is adapted from reference [91].

The connections on the breakout PCB are then rerouted and redirected to the backplane connector.

A.4 BACKPLANE

The backplane is a large passive PCB distributing signal and power to and from the NI cards to the GLB devices.

1 The digital NI card Spec sheet [90], and manual [91]. The analog PCI-6713 spec sheet [53], the analog PCI-6733 spec sheet [54] and their combining manual [92].

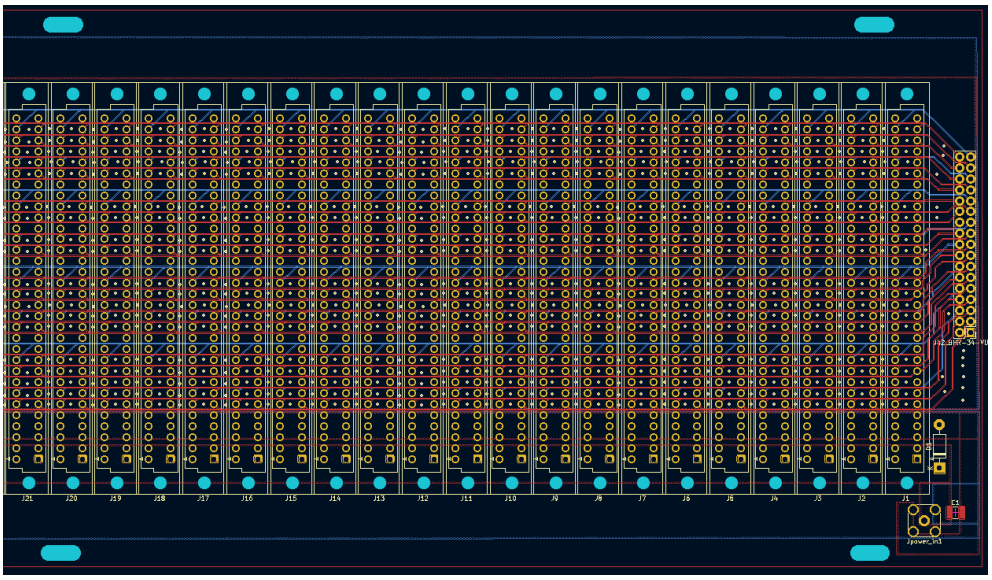

Figure 51: Section of the backplane PCB design for the digital GLB system. The schematic shows an array of DIN41612_02x32_AC connectors. The pins with the same position on the DIN connectors are all interconnected. The horizontal wires connect and distribute the signal between the pins. The smaller rightmost connector is a pin header to attach a ribbon cable to extend the signal from this backplane to another. The bottom row of the DIN connector array is reserved for power distribution. In the case of the digital system, the backplane guides a 5V DC line; for the analog case, it is AC line voltage.

B

PROMETHEUS CONTROL INTERFACE

The system consists of four main components. The gimbal mount with the window, the Newport PR50CC motors diving the X- and Y-axis of the gimbal, the SMC100cc Newport motion controller, a RaspberryPi (Pi), and the Cicero interface. The Pi is the interface between the existing Cicero control system and the Newport motion controller. In this Appendix, the middleman between Cicero and the SMC100 motion controller will be explained.

The SMC100cc can be controlled via Serial commands. The list of available commands can be found in the manual [93].

In the control sequence of the BEC4 lab, Cicero sends digital 5V signals to multiple devices. The motion of the DC motors can't be triggered directly by a single rising voltage signal. Therefore The GPIO pins of a Pi are used to await a trigger signal. A Python script running in the background of the Pi then waits for this signal and sends a Serial command to the SMC100cc Newport motion controller.

The heart of the Pi control is the Python script running in the system's background. The tasks start automatically whenever the Pi is rebooted. The first script is dedicated to listening to a digital 3.3V trigger on one of the Pi's GPIO pins. (The 5V signal from Cicero is converted to a 3.3V signal using a passive voltage divider). Whenever it receives a rising flank, it sends a serial command to the SMC100cc to move the motors to a certain angle position. This is used to synchronize the beam displacer and the z-translation stage.

This angle specification in x and y is called `position_1`. The GPIO pin is constantly on 3.3V as long as the ODT should be on `position_1`. When the Pi's GPIO pin voltage is lowered to 0, the Python script sends another Serial command to the SMC100cc and sets the angles to `position_0` again. (colloquially, one can think of the zeroth position as the pick-up position in the main chamber and the first position as the drop position)

The second Python file is built to wait for serial commands from a tertiary system (in this case, Cicero, but it could be any PC in principle). These serial commands can execute more complex tasks, such as aligning the silica window or changing dynamic motion parameters stored in the SMC100cc.

Both Python scripts have access to a third text file, on which not only the angles for `position_0` and `position_1` are stored but also the dynamical values (velocity, acceleration, and jerk) with which the DC motors are

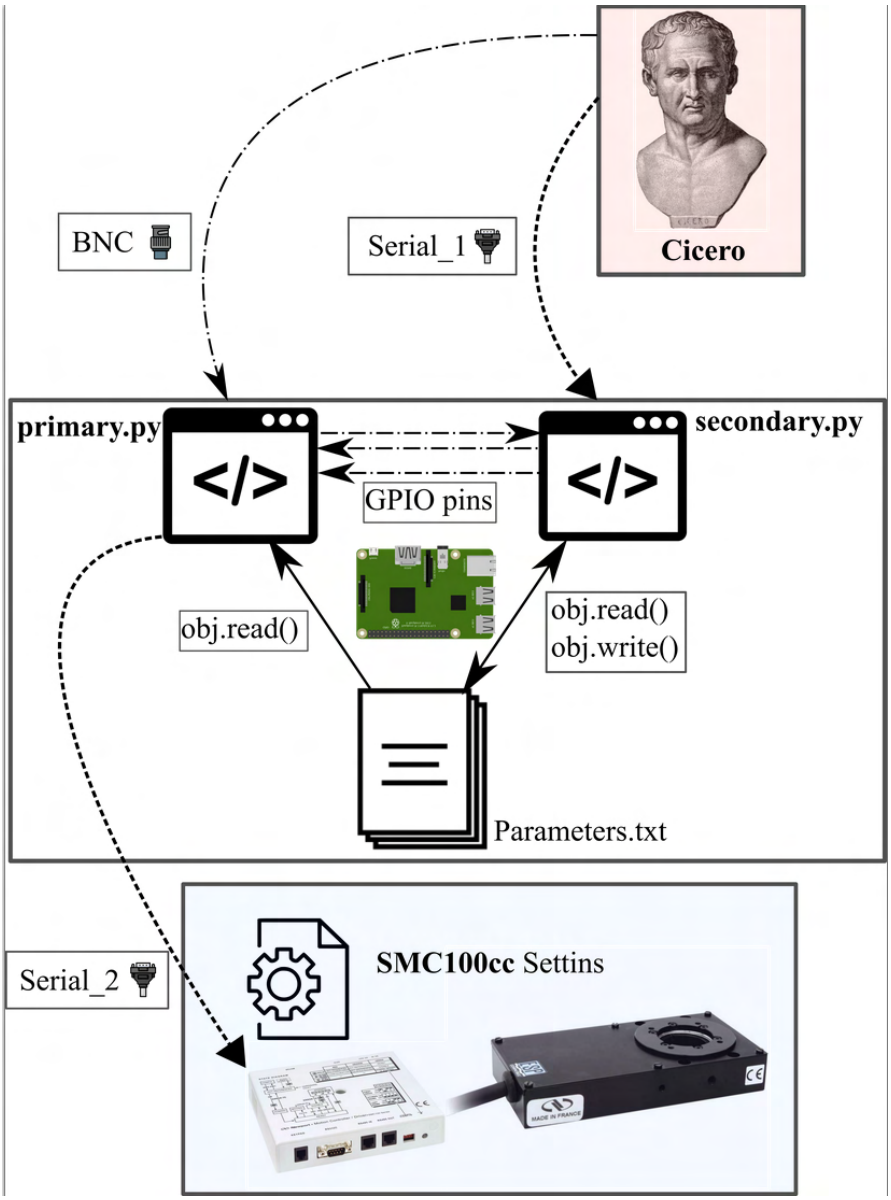

Figure 52: Schematic hierarchies of the beam displacer control.

driven are stored. These values can be transmitted to the SMC100 to change the SMC100cc's internal settings. This settings procedure is time intensive O(30s).

There are also GPIO-to-GPIO hardware connections in the Pi to transmit internal triggers between the two running scripts[1]. These triggers, for example, prevent the user from making remote changes on the SMC100cc settings while the silica window is not in `position_0`. They also deal as artificial trigger values if specific changes have been made to the text file, and a movement should be executed afterward.

1 To every software developer or programming enthusiast reading this... please don't be mad

B.1 LOGIC MAP

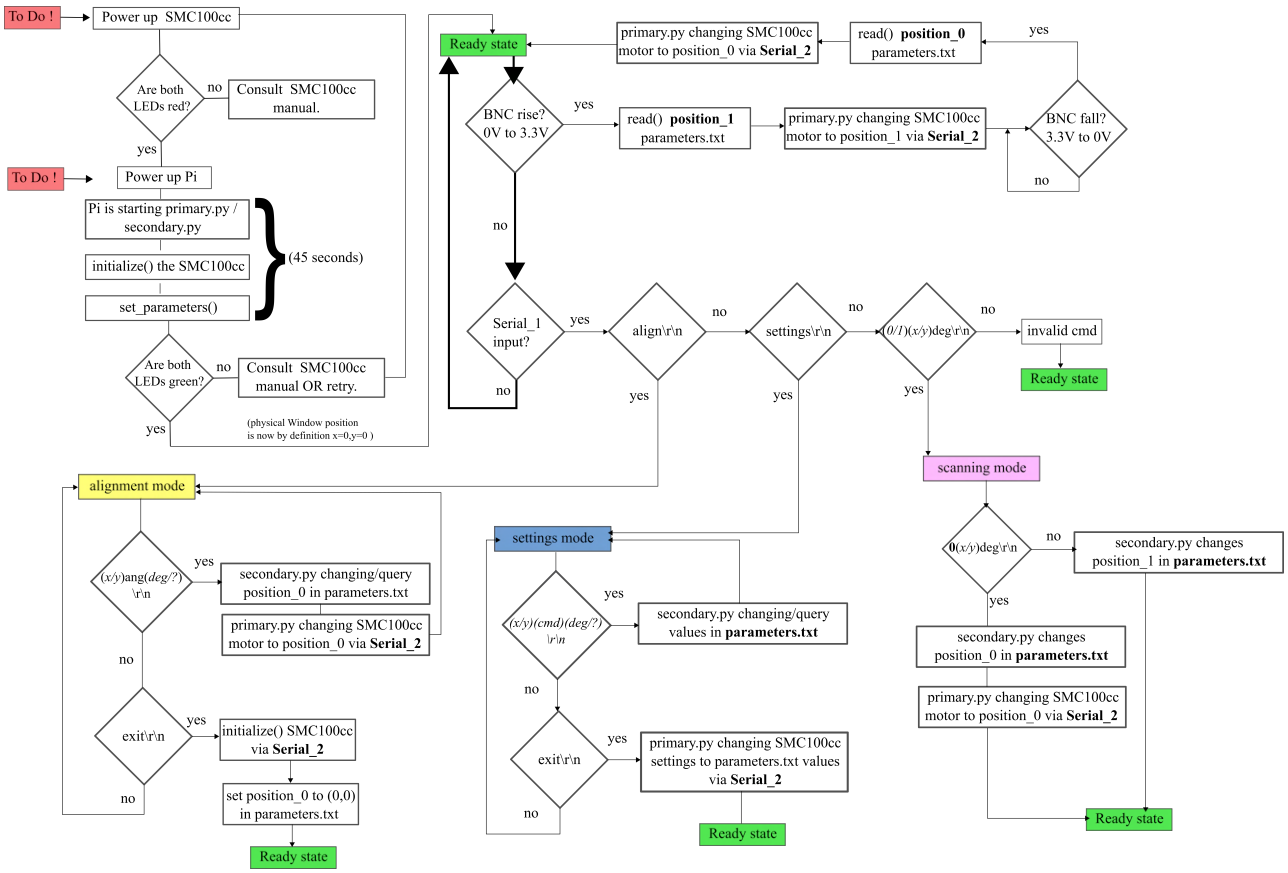

Figure 53: Flowchart of Prometheus' operation. After booting, the system is in the "ready state" and awaits external triggers to execute parameter changes or movements. The two trigger inputs are via a BNC connection and a Serial connection. The BNC connection triggers the main cycle relevant for moving the ODT from the pick-up position to the drop-off position. The serial command can be used to enter the "alignment mode", "settings mode" and "scanning mode".

B.1.1 *Ready State*

This is the default operation state of the system. After booting, the two LEDs on the SMC100cc should light up green. In this stage, the secondary and the primary Python script await input signals from a rising voltage flank through the BNC cable or a serial command via the Serial_1 port.

B.1.1.1 *BNC Trigger*

The rising voltage flank triggers the start of the "standard" operation cycle. First, the primary.py file receives the trigger to look up the x- and y- angles for position_1 (aka the drop-off in the science chamber). Then via the serial_2 connection, a serial command is sent to the SMC100cc, changing the absolute angle position of the x and y motors following the parameters listed in parameters.txt. This step takes 1-2 seconds. The exact time depends on the dynamic variables (velocity, acceleration, jerk of rotation). During the motion, the green LEDs blink, which is also an indicator of the successful transmission of the command.

Then when the voltage is lowered again, the procedure repeats. First, the absolute angles for position_0 are read from the file parameters.txt. Then the movement is executed by sending the serial commands to the SCM100cc. The LEDs blink. The motion is executed.

One important caveat is that while the motors are in motion, the SMC100cc is "blind" for inputs. When the voltage signal is lowered again fast, and the motion is unfinished, the window's position will be stuck in the drop-off (position 1). Another artificial rising and lowering voltage flank will restore the position to pick-up[2]. Therefore, the voltage plateau should be high (5V out in Cicero) long enough for the movement to finish. It needs to "see" the voltage flank fall.

B.1.1.2 *Serial_1 Trigger*

This serial input adds a lot of convenience and flexibility to the system. In principle, the binary on/off BNC input is sufficient to pick up the atoms at the magnetic trap and deliver them at the cross dipole trap. But this channel becomes important, especially when the pick-up or drop-off positions need to be optimized or the absolute home position should be changed. Also, when the dynamic settings must maybe be altered. All modes, EXCEPT the scanning mode, can be addressed ONLY in position_0, aka when there is NO voltage input on the BNC. This ensures that the cycle operation is more robust once started.

2 This can be done with the manual override toggles.

B.1.2 *Alignment Mode*

The alignment mode is created to change the pick-up position by changing the absolute home position. **The global zero will be reset after exiting this mode!**

Enter alignment mode:

```
align\r\n
```

Change absolute x angle relative to global zero to +20 deg:

```
xang20\r\n
```

Change absolute y angle relative to global zero to -2.5 deg:

```
yang-2.5\r\n
```

Query the current y angle of the window relative o global zero:

```
yang?\r\n
```

Change the x angle relative to global zero by 0.5 deg at a time:

```
xang-0.5\r\n
xang0.5\r\n
xang1\r\n
xang1.5\r\n
xang2\r\n
xang2.5\r\n
```

...

Exit the alignment mode and **set the current physical angle to new global zero**:

```
exit\r\n
```

B.1.3 *Settings Mode*

After exiting, the settings mode also changes the global zero to the current physical position. Enter settings mode:

```
settings\r\n
```

Query the status of all set values in parameters.txt:

```
dall\r\n
```

returns:

[position_0] ang_x = 0 ang_y = 0

[position_1] ang_x = 1.1 ang_y = 17.1

[velocity] vel_x = 40 vel_y = 40

[acceleration] acc_x = 40 acc_y = 40

[jerk] jrk_x = 0.5 jrk_y = 0.5

If only a single value is of interest:

Query the status of the velocity for the x motor in parameters.txt:

```
xvel?\r\n
```

Query the status of the acceleration for the y motor in parameters.txt:

```
yacc?\r\n
```

Query the status of the jerk for the x motor in parameters.txt:

```
xjrk?\r\n
```

change the value of the acceleration for y motor in parameters.txt to 40:

```
yacc40\r\n
```

change the value of the position_1 for the x motor in parameters.txt to -3.5 deg:

```
xang-3.5\r\n
```

Exit the settings mode and overwrite the SMC100cc dynamic parameters and change global zero:

```
exit\r\n
```

B.1.4 *Scanning Mode*

The scanning mode is more like a pseudo mode. Unlike alignment and settings, it does not need to be entered or exited. **Also, only changes to the position in the parameter.txt file are made, and the global zero is always conserved.**

What can be changed are the x and y angles for pick up and drop off. In the special case of changing the pick-up position, also a movement is executed since it assumes the changes have been made while being in position 0. Since we are in the ready state, we should always be able to start the motion sequence form here. When the trigger is provided, then the new position 1 will be used.

Set the position_0 x angle to 14deg in parameters.txt relative to global zero and move:

```
0x14\r\n
```

Set the position_0 y angle to 1deg in parameters.txt relative to global zero and move:

```
0y1\r\n
```

Set the position_1 y angle to -2.9deg in parameters.txt relative to global zero and DONT move:

```
1y-2.9\r\n
```

No exit command is necessary! After finishing the scan of position 0, it is recommended to restore the value in the txt file of position 0 back to zero. The value for position 1 should be changed such that the angle interval is

still the same as before. This can be done by entering the settings mode and changing the parameters of positions 0 and 1. (If only Position 1 - in the science chamber - was changed, then the value does not need to be changed.) This helps to protect the alignment from a sudden power outage or malfunction

Example: Position 1 AND position 0 were scanned, and their optimal values were found to be:

[position_0] ang_x = 2 ang_y = -1.2

[position_1] ang_x = 13 ang_y = 6

The Settings mode should now be entered and the values should be adjusted to be

NEW [position_0] ang_x = 0 ang_y = 0

NEW [position_1] ang_x = 11 ang_y = 7.2

now the exit command can be executed. DONE.

C

MAKING COILS

a) b)

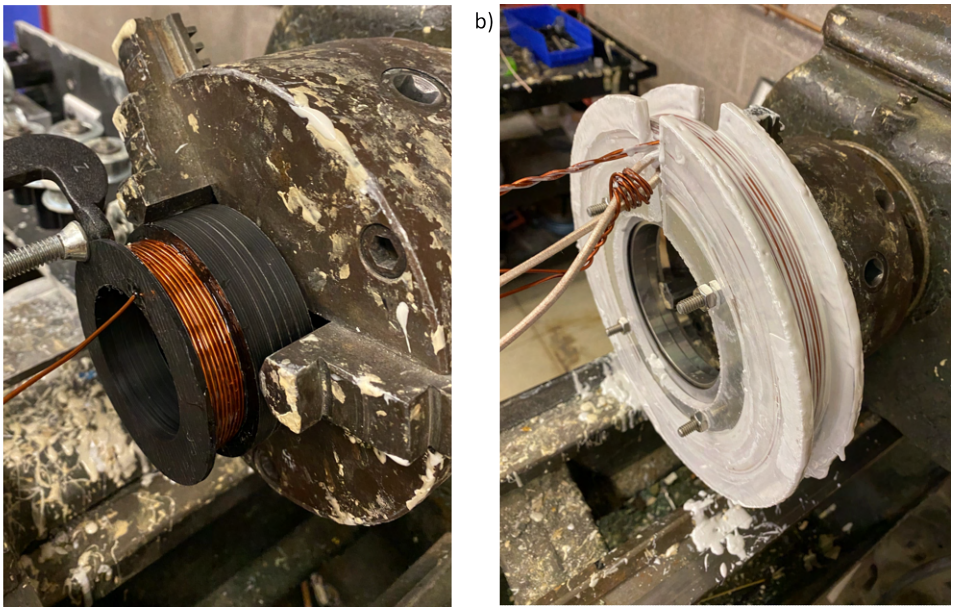

Figure 54: The Photograph a) shows the fabrication of the side coils, and Photograph b) depicts the main gradient coil. The main gradient coil would be square hollow core copper wire insulated by fiberglass. The lathe holds the mold and rotates while the hollow core wire is fed. The coil is fixated using non-magnetic high-temperature two-component epoxy (in white). The side coils a) are wound on a plastic mold with standard magnet wire and glued together with standard high-temperature epoxy.

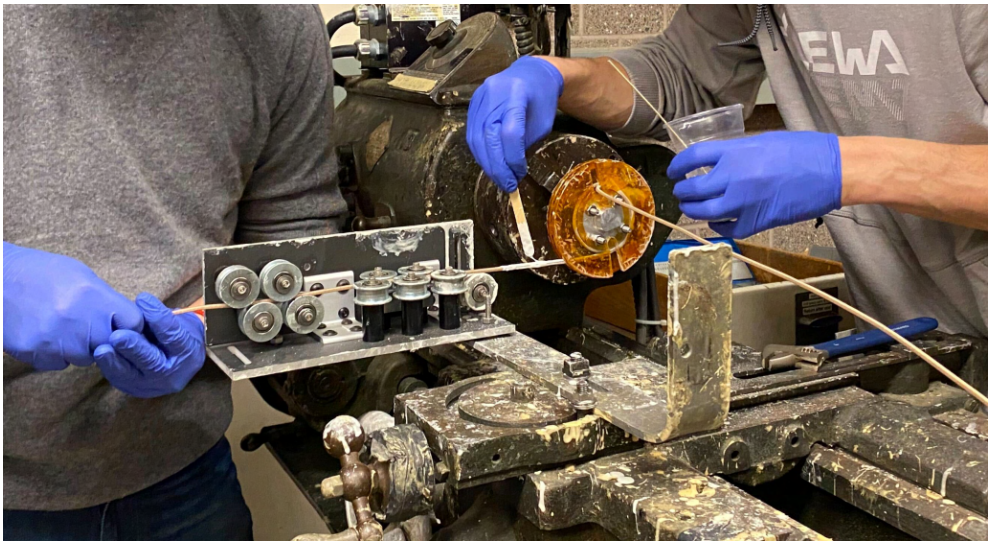

Figure 55: Winding process of the magnetic field coil. The square hollow-core wire is fed into the mold under constant tension to ensure tight winding. In parallel, the epoxy is applied in between the layers.

a) b)

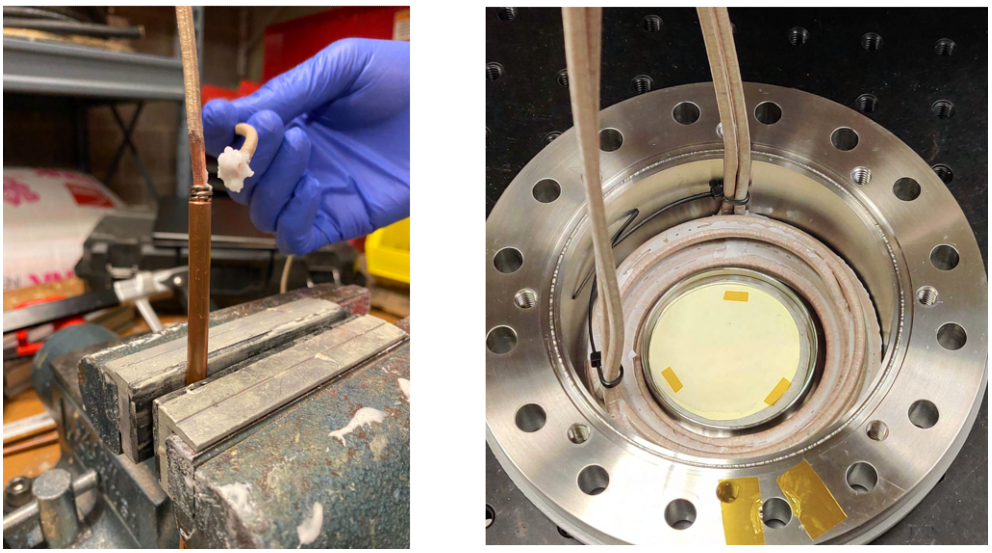

Figure 56: Picture a) depicts the preparation for brazing the end of the square wire to a swage-lock-able copper tube. The fiberglass insulation is stripped, and the copper is fitted to the tube. Then flux and solder are applied to the joint before heating it with a propane torch. Image b) depicts the initial plan of mounting water-cooled coils inside the reentrant viewport, close to the atoms. It was abandoned due to the lack of access to the objective and inhomogeneity concerns.

BIBLIOGRAPHY

[1] Christopher J Foot. *Atomic physics*. Vol. 7. OUP Oxford, 2004.

[2] Gerald Gabrielse, Hans Dehmelt, and William Kells. "Observation of a relativistic, bistable hysteresis in the cyclotron motion of a single electron." In: *Physical review letters* 54.6 (1985), p. 537.

[3] Hans Dehmelt. "A single atomic particle forever floating at rest in free space: New value for electron radius." In: *Physica Scripta* 1988.T22 (1988), p. 102.

[4] Mike H Anderson, Jason R Ensher, Michael R Matthews, Carl E Wieman, and Eric A Cornell. "Observation of Bose-Einstein condensation in a dilute atomic vapor." In: *science* 269.5221 (1995), pp. 198–201.

[5] Kendall B Davis, M-O Mewes, Michael R Andrews, Nicolaas J van Druten, Dallin S Durfee, DM Kurn, and Wolfgang Ketterle. "Bose-Einstein condensation in a gas of sodium atoms." In: *Physical review letters* 75.22 (1995), p. 3969.

[6] Wolfgang Ketterle, Dallin S Durfee, and DM Stamper-Kurn. "Making, probing and understanding Bose-Einstein condensates." In: *arXiv preprint cond-mat/9904034* (1999).

[7] Brian DeMarco and Deborah S Jin. "Onset of Fermi degeneracy in a trapped atomic gas." In: *science* 285.5434 (1999), pp. 1703–1706.

[8] CA Regal, Markus Greiner, and Deborah S Jin. "Observation of resonance condensation of fermionic atom pairs." In: *Physical review letters* 92.4 (2004), p. 040403.

[9] Julian Léonard, Sooshin Kim, Joyce Kwan, Perrin Segura, Fabian Grusdt, Cécile Repellin, Nathan Goldman, and Markus Greiner. "Realization of a fractional quantum Hall state with ultracold atoms." In: *arXiv preprint arXiv:2210.10919* (2022).

[10] Markus Greiner, Olaf Mandel, Tilman Esslinger, Theodor W Hänsch, and Immanuel Bloch. "Quantum phase transition from a superfluid to a Mott insulator in a gas of ultracold atoms." In: *nature* 415.6867 (2002), pp. 39–44.

[11] Immanuel Bloch, Jean Dalibard, and Sylvain Nascimbene. "Quantum simulations with ultracold quantum gases." In: *Nature Physics* 8.4 (2012), pp. 267–276.

[12] Dieter Jaksch, Juan Ignacio Cirac, Peter Zoller, Steve L Rolston, Robin Côté, and Mikhail D Lukin. "Fast quantum gates for neutral atoms." In: *Physical Review Letters* 85.10 (2000), p. 2208.

[13] Mark Saffman, Thad G Walker, and Klaus Mølmer. "Quantum information with Rydberg atoms." In: *Reviews of modern physics* 82.3 (2010), p. 2313.

[14] Iris Cong, Harry Levine, Alexander Keesling, Dolev Bluvstein, Sheng-Tao Wang, and Mikhail D Lukin. "Hardware-efficient, fault-tolerant quantum computation with Rydberg atoms." In: *Physical Review X* 12.2 (2022), p. 021049.

[15] Gregory Bentsen, Tomohiro Hashizume, Anton S Buyskikh, Emily J Davis, Andrew J Daley, Steven S Gubser, and Monika Schleier-Smith. "Treelike interactions and fast scrambling with cold atoms." In: *Physical review letters* 123.13 (2019), p. 130601.

[16] Sepehr Ebadi, Alexander Keesling, Madelyn Cain, Tout T Wang, Harry Levine, Dolev Bluvstein, Giulia Semeghini, Ahmed Omran, J-G Liu, Rhine Samajdar, et al. "Quantum optimization of maximum independent set using Rydberg atom arrays." In: *Science* (2022), eabo6587.

[17] Gretchen K Campbell, Andrew D Ludlow, Sebastian Blatt, Jan W Thomsen, Michael J Martin, Marcio HG De Miranda, Tanya Zelevinsky, Martin M Boyd, Jun Ye, Scott A Diddams, et al. "The absolute frequency of the 87Sr optical clock transition." In: *Metrologia* 45.5 (2008), p. 539.

[18] Lauriane Chomaz, Igor Ferrier-Barbut, Francesca Ferlaino, Bruno Laburthe-Tolra, Benjamin L Lev, and Tilman Pfau. "Dipolar physics: A review of experiments with magnetic quantum gases." In: *arXiv preprint arXiv:2201.02672* (2022).

[19] Thorsten Köhler, Krzysztof Góral, and Paul S Julienne. "Production of cold molecules via magnetically tunable Feshbach resonances." In: *Reviews of modern physics* 78.4 (2006), p. 1311.

[20] Roman Krems, Bretislav Friedrich, and William C Stwalley. *Cold molecules: theory, experiment, applications*. CRC press, 2009.

[21] Richard P Feynman. "Simulating physics with computers." In: *Feynman and computation*. CRC Press, 2018, pp. 133–153.

[22] Jonathan Simon, Waseem S Bakr, Ruichao Ma, M Eric Tai, Philipp M Preiss, and Markus Greiner. "Quantum simulation of antiferromagnetic spin chains in an optical lattice." In: *Nature* 472.7343 (2011), pp. 307–312.

[23] Rudolf Grimm, Matthias Weidemüller, and Yurii B Ovchinnikov. "Optical dipole traps for neutral atoms." In: *Advances in atomic, molecular, and optical physics*. Vol. 42. Elsevier, 2000, pp. 95–170.

[24] Sarthak Subhankar, Yang Wang, Tsz-Chun Tsui, SL Rolston, and James V Porto. "Nanoscale atomic density microscopy." In: *Physical Review X* 9.2 (2019), p. 021002.

[25] Mickey McDonald, Jonathan Trisnadi, Kai-Xuan Yao, and Cheng Chin. "Superresolution microscopy of cold atoms in an optical lattice." In: *Physical Review X* 9.2 (2019), p. 021001.

[26] Jacob F Sherson, Christof Weitenberg, Manuel Endres, Marc Cheneau, Immanuel Bloch, and Stefan Kuhr. "Single-atom-resolved fluorescence imaging of an atomic Mott insulator." In: *Nature* 467.7311 (2010), pp. 68–72.

[27] Lord Rayleigh. "XXXI. Investigations in optics, with special reference to the spectroscope." In: *The London, Edinburgh, and Dublin Philosophical Magazine and Journal of Science* 8.49 (1879), pp. 261–274.

[28] Martin Miranda, Ryotaro Inoue, Naoki Tambo, and Mikio Kozuma. "Site-resolved imaging of a bosonic Mott insulator using ytterbium atoms." In: *Physical Review A* 96.4 (2017), p. 043626.

[29] Aaron J. Krahn. *Erbium quantum gas microscope. Doctoral dissertation, Harvard University Graduate School of Arts and Sciences.* https://nrs.harvard.edu/URN-3:HUL.INSTREPOS:37369476. [Online; accessed 22-Jan-2023]. 2021.

[30] Waseem S Bakr, Jonathon I Gillen, Amy Peng, Simon Fölling, and Markus Greiner. "A quantum gas microscope for detecting single atoms in a Hubbard-regime optical lattice." In: *Nature* 462.7269 (2009), pp. 74–77.

[31] Jin Yang, Liyu Liu, Jirayu Mongkolkiattichai, and Peter Schauss. "Site-resolved imaging of ultracold fermions in a triangular-lattice quantum gas microscope." In: *PRX Quantum* 2.2 (2021), p. 020344.

[32] Jason S Rosenberg, Lysander Christakis, Elmer Guardado-Sanchez, Zoe Z Yan, and Waseem S Bakr. "Observation of the Hanbury Brown–Twiss effect with ultracold molecules." In: *Nature Physics* 18.9 (2022), pp. 1062–1066.

[33] Lawrence W Cheuk, Matthew A Nichols, Melih Okan, Thomas Gersdorf, Vinay V Ramasesh, Waseem S Bakr, Thomas Lompe, and Martin W Zwierlein. "Quantum-gas microscope for fermionic atoms." In: *Physical review letters* 114.19 (2015), p. 193001.

[34] Philip Zupancic, Philipp M Preiss, Ruichao Ma, Alexander Lukin, M Eric Tai, Matthew Rispoli, Rajibul Islam, and Markus Greiner. "Ultra-precise holographic beam shaping for microscopic quantum control." In: *Optics express* 24.13 (2016), pp. 13881–13893.

[35] Christian Gross and Waseem S Bakr. "Quantum gas microscopy for single atom and spin detection." In: *Nature Physics* 17.12 (2021), pp. 1316–1323.

[36] Johannes Schachenmayer, David M Weld, Hirokazu Miyake, Georgios A Siviloglou, Wolfgang Ketterle, and Andrew J Daley. "Adiabatic cooling of bosons in lattices to magnetically ordered quantum states." In: *Physical Review A* 92.4 (2015), p. 041602.

[37] Paul Niklas Jepsen. *Spin dynamics in a tunable Heisenberg model realized with ultracold atoms*. https://www.rle.mit.edu/cua_pub/ketterle_group/Theses/jepsen_thesis.pdf. [Online; accessed 24-Jan-2023]. February 2022.

[38] Woo Chang Chung. *Quantum Simulation of Spin-1 Physics with Bosons in Optical Lattice*. https://www.rle.mit.edu/cua_pub/ketterle_group/Theses/Chung_%20Woo%20Chang_THESIS.pdf. [Online; accessed 24-Jan-2023]. June 2021.

[39] Ehud Altman, Walter Hofstetter, Eugene Demler, and Mikhail D Lukin. "Phase diagram of two-component bosons on an optical lattice." In: *New Journal of Physics* 5.1 (2003), p. 113.

[40] Julius de Hond, Jinggang Xiang, Woo Chang Chung, Enid Cruz-Colón, Wenlan Chen, William Cody Burton, Colin J Kennedy, Wolfgang Ketterle, et al. "Preparation of the spin-Mott state: a spinful Mott insulator of repulsively bound pairs." In: *Physical Review Letters* 128.9 (2022), p. 093401.

[41] Matthias Vojta. "Quantum phase transitions." In: *Reports on Progress in Physics* 66.12 (2003), p. 2069.

[42] Daniel A Steck. "Rubidium 87 D line data." In: (2001).

[43] Daniel A Steck. "Quantum and atom optics." In: (2007).

[44] Erik W Streed, Ananth P Chikkatur, Todd L Gustavson, Micah Boyd, Yoshio Torii, Dominik Schneble, Gretchen K Campbell, David E Pritchard, and Wolfgang Ketterle. "Large atom number Bose-Einstein condensate machines." In: *Review of Scientific Instruments* 77.2 (2006), p. 023106.

[45] Wolfgang Ketterle, Kendall B Davis, Michael A Joffe, Alex Martin, and David E Pritchard. "High densities of cold atoms in a dark spontaneous-force optical trap." In: *Physical review letters* 70.15 (1993), p. 2253.

[46] Jean Dalibard and Claude Cohen-Tannoudji. "Laser cooling below the Doppler limit by polarization gradients: simple theoretical models." In: *JOSA B* 6.11 (1989), pp. 2023–2045.

[47] Yue-Sum Chin, Matthias Steiner, and Christian Kurtsiefer. "Polarization gradient cooling of single atoms in optical dipole traps." In: *Physical Review A* 96.3 (2017), p. 033406.

[48] John David Jackson. *Classical electrodynamics*. 1999.

[49] Wolfgang Petrich, Michael H Anderson, Jason R Ensher, and Eric A Cornell. "Stable, tightly confining magnetic trap for evaporative cooling of neutral atoms." In: *Physical Review Letters* 74.17 (1995), p. 3352.

[50] Fam Le Kien, Philipp Schneeweiss, and Arno Rauschenbeutel. "Dynamical polarizability of atoms in arbitrary light fields: general theory and application to cesium." In: *The European Physical Journal D* 67.5 (2013), pp. 1–16.

[51] Bill Whitlock. "Understanding, Finding, and Eliminating Ground Loops." In: *Handout for Courses A14T and B50T, CEDIA* (2003), p. 108.

[52] Aviv Keshet and Wolfgang Ketterle. "A distributed, graphical user interface based, computer control system for atomic physics experiments." In: *Review of Scientific Instruments* 84.1 (2013), p. 015105.

[53] National Instruments. *PCI-6713-Specs*. https://www.ni.com/docs/en-US/bundle/ni-6711-6713-specs/resource/371011c.pdf. [Online; accessed 01-Jan-2023]. 2005.

[54] National Instruments. *PCI-6733-Specs*. https://www.ni.com/docs/en-US/bundle/ni-6731-6733-specs/resource/371232b.pdf. [Online; accessed 01-Jan-2023]. 2005.

[55] BROADCOM. *HCPL-0723 Datasheet: 50-MBd 2-ns PWD High-Speed CMOS Optocoupler*. https://docs.broadcom.com/doc/AV02-0643EN. [Online; accessed 10-Jan-2023]. September 26, 2017.

[56] CUI. *DC-DC CONVERTER Datasheet: PDS1-S5-S12-M*. https://www.cui.com/product/resource/pds1-m.pdf. [Online; accessed 10-Jan-2023]. October 27, 2022.

[57] Jack G Ganssle. "A guide to debouncing." In: *Guide to Debouncing, Ganssle Group, Baltimore, MD, US* (2004), pp. 1–22.

[58] Acopian. *Mini Encapsulated, LINEAR REGULATED, AC-DC dual output PC board mounting Datasheet*. https://www.acopian.com/inc/streamFile.asp?loc=info&id=AcopianCatMiniPCBDual.pdf. [Online; accessed 10-Jan-2023]. 2022.

[59] Texas Instruments. *INA114 Precision Instrumentation Amplifier*. https://www.ti.com/lit/ds/symlink/ina114.pdf. [Online; accessed 05-Sep-2022]. March 1998.

[60] Paul Horowitz, Winfield Hill, and Ian Robinson. *The art of electronics*. Vol. 2. Cambridge university press Cambridge, 1989.

[61] Analog Devices. *Analog Filter Wizard*. https://tools.analog.com/en/filterwizard/. [Online; accessed 22-Jan-2023]. 2023.

[62] Analog Devices. *ADA4075-2 Ultralow Noise Amplifier at Lower Power*. https://www.analog.com/media/en/technical-documentation/data-sheets/ADA4075-2.pdf. [Online; accessed 05-Sep-2022]. 2013.

[63] Recom. *RAC10-15DK/277 Datasheet*. https://recom-power.com/pdf/Powerline_AC-DC/RAC10-K_277.pdf. [Online; accessed 01-Jan-2023]. August 2020.

[64] Pico Technology. *PicoScope 5000 Series, High Speed and High Resolution*. https://www.picotech.com/download/datasheets/MM040.en-8.pdf. [Online; accessed 22-Jan-2023]. 2023.

[65] Analog Devices. *LT3045; 20V, 500mA, Ultralow Noise, Ultrahigh PSRR Linear Regulator*. https://www.analog.com/media/en/technical-documentation/data-sheets/lt3045.pdf. [Online; accessed 05-Sep-2022]. March 2021.

[66] Analog Devices. *LT3094; -20V, 500mA, Ultralow Noise, Ultrahigh PSRR Linear Regulator*. https://www.analog.com/media/en/technical-documentation/data-sheets/LT3094.pdf. [Online; accessed 05-Sep-2022]. Jan 2020.

[67] John H Moore, Christopher C Davis, Michael A Coplan, and Sandra C Greer. *Building scientific apparatus*. Cambridge University Press, 2009.

[68] Plymouth Grating. *Optical thin-film dielectric coatings*. https://www.plymouthgrating.com/about-pgl/pgls-technology/thin-film-coating/. [Online; accessed 22-Jan-2023]. 2022.

[69] Debayan Mitra. *Exploring attractively interacting fermions in 2D using a Quantum Gas Microscope*. https://physics.princeton.edu//archives/theses/lib/upload/DM_thesis_electronic_version.pdf. [Online; accessed 05-Sep-2022]. Nov 2018.

[70] M. R. Andrews, C. G. Townsend, H.-J. Miesner, D. S. Durfee, D. M. Kurn, and W. Ketterle. "Observation of Interference Between Two Bose Condensates." In: *Science* 275.5300 (1997), pp. 637–641. DOI: 10.1126/science.275.5300.637. eprint: https://www.science.org/doi/pdf/10.1126/science.275.5300.637. URL: https://www.science.org/doi/abs/10.1126/science.275.5300.637.

[71] A Röhrl, M Naraschewski, A Schenzle, and H Wallis. "Transition from phase locking to the interference of independent Bose condensates: Theory versus experiment." In: *Physical review letters* 78.22 (1997), p. 4143.

[72] Max Born and Emil Wolf. *Principles of optics: electromagnetic theory of propagation, interference and diffraction of light*. Elsevier, 2013.

[73] Joseph W Goodman and P Sutton. "Introduction to Fourier optics." In: *Quantum and Semiclassical Optics-Journal of the European Optical Society Part B* 8.5 (1996), p. 1095.

[74] TC Li, H Kelkar, D Medellin, and MG Raizen. "Real-time control of the periodicity of a standing wave: an optical accordion." In: *Optics express* 16.8 (2008), pp. 5465–5470.

[75] Karl D Nelson, Xiao Li, and David S Weiss. "Imaging single atoms in a three-dimensional array." In: *Nature Physics* 3.8 (2007), pp. 556–560.

[76] Simon Wili, Tilman Esslinger, and Konrad Viebahn. "An accordion superlattice for controlling atom separation in optical potentials." In: *arXiv preprint arXiv:2301.04144* (2023).

[77] Michael J Rust, Mark Bates, and Xiaowei Zhuang. "Sub-diffraction-limit imaging by stochastic optical reconstruction microscopy (STORM)." In: *Nature methods* 3.10 (2006), pp. 793–796.

[78] Julian Léonard, Moonjoo Lee, Andrea Morales, Thomas M Karg, Tilman Esslinger, and Tobias Donner. "Optical transport and manipulation of an ultracold atomic cloud using focus-tunable lenses." In: *New Journal of Physics* 16.9 (2014), p. 093028.

[79] Manuel Endres. *Probing correlated quantum many-body systems at the single-particle level*. Springer Science & Business, 2014.

[80] Markus Greiner, Immanuel Bloch, Theodor W Hänsch, and Tilman Esslinger. "Magnetic transport of trapped cold atoms over a large distance." In: *Physical Review A* 63.3 (2001), p. 031401.

[81] TL Gustavson, AP Chikkatur, AE Leanhardt, A Görlitz, Subhadeep Gupta, DE Pritchard, and Wolfgang Ketterle. "Transport of Bose-Einstein condensates with optical tweezers." In: *Physical Review Letters* 88.2 (2001), p. 020401.

[82] Jongchul Mun. *Bose-Einstein Condensates in Optical Lattices: The Superfluid to Mott Insulator Phase Transition*. https://www.rle.mit.edu/cua_pub/ketterle_group/Theses/Mun%20Jongchul%20Thesis.pdf. [Online; accessed 05-Sep-2022]. May 2008.

[83] Thorlabs. *ELL18 - Rotation Stage*. https://www.thorlabs.com/drawings/56aabbcf0e824bc0-2BCCABA4-CBC1-C629-668BA36003AC972A/ELL18-Manual.pdf. [Online; accessed 03-Oct-2022]. June 2022.

[84] Newport. *PR50 High Speed Compact Rotation Stages*. https://www.newport.com/mam/celum/celum_assets/resources/PR50_Data_Sheet.pdf?2. [Online; accessed 05-Sep-2022]. July 2022.

[85] Thorlabs. *PGM1SE - Piezoelectric Gimbal Mount with Strain Gauge Feedback*. https://www.thorlabs.com/drawings/ae9ba9e0c51f2e09-3B676BC5-CC91-430A-B813DC4D6C9A74EB/PGM1SE-KinesisManual.pdf. [Online; accessed 03-Oct-2022]. March 2022.

[86] Bryce Gadway, Daniel Pertot, René Reimann, Martin G Cohen, and Dominik Schneble. "Analysis of Kapitza-Dirac diffraction patterns beyond the Raman-Nath regime." In: *Optics express* 17.21 (2009), pp. 19173–19180.

[87] Charles S Adams, Heun Jin Lee, Nir Davidson, Mark Kasevich, and Steven Chu. "Evaporative cooling in a crossed dipole trap." In: *Physical review letters* 74.18 (1995), p. 3577.

[88] David Jacob, Emmanuel Mimoun, Luigi De Sarlo, Martin Weitz, Jean Dalibard, and Fabrice Gerbier. "Production of sodium Bose–Einstein condensates in an optical dimple trap." In: *New Journal of Physics* 13.6 (2011), p. 065022.

[89] DM Stamper-Kurn, H-J Miesner, AP Chikkatur, S Inouye, J Stenger, and W Ketterle. "Reversible formation of a Bose-Einstein condensate." In: *Physical review letters* 81.11 (1998), p. 2194.

[90] National Instruments. *PCI-DIO-32HS Specifications*. https://www.ni.com/docs/en-US/bundle/374163a/page/download.html. [Online; accessed 01-Jan-2023]. 2005.

[91] National Instruments. *PCI-DIO-32HS Manual*. https://www.ni.com/docs/en-US/bundle/371464d/page/download.html. [Online; accessed 01-Jan-2023]. 2005.

[92] National Instruments. *PCI-6713/6733-Manual*. https://www.ni.com/docs/en-US/bundle/ni-6711-6713-6722-6723-6731-6733-features/resource/370735f.pdf. [Online; accessed 01-Jan-2023]. 2005.

[93] Newport. *SMC100CC Single-Axis Motion Controller/Driver for DC or Stepper Motor*. https://www.newport.com/medias/sys_master/images/images/h8d/h3a/8797263101982/SMC100CC-SMC100PP-User-Manual.pdf. [Online; accessed 05-Jan-2023]. Aug 2015.

DECLARATION

Eidgenössische Technische Hochschule Zürich
Swiss Federal Institute of Technology Zurich

Declaration of originality

The signed declaration of originality is a component of every semester paper, Bachelor's thesis, Master's thesis and any other degree paper undertaken during the course of studies, including the respective electronic versions.

Lecturers may also require a declaration of originality for other written papers compiled for their courses.

I hereby confirm that I am the sole author of the written work here enclosed and that I have compiled it in my own words. Parts excepted are corrections of form and content by the supervisor.

Title of work (in block letters):

TOWARDS A RUBIDIUM QUANTUM GAS MICROSCOPE

Authored by (in block letters):
For papers written by groups the names of all authors are required.

Name(s):	**First name(s):**
FRICKE	JACOB FERDINAND

With my signature I confirm that

- I have committed none of the forms of plagiarism described in the 'Citation etiquette' information sheet.
- I have documented all methods, data and processes truthfully.
- I have not manipulated any data.
- I have mentioned all persons who were significant facilitators of the work.

I am aware that the work may be screened electronically for plagiarism.

Place, date	**Signature(s)**
Cambridge MA, 31.01.23	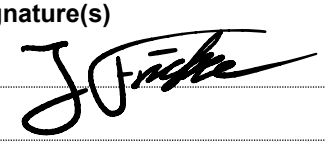

For papers written by groups the names of all authors are required. Their signatures collectively guarantee the entire content of the written paper.